



## Thèse de Doctorat

Présentée Par:

**Danielle EL HAJJ**

pour l'obtention du grade de Docteur de l'Université de Lille

05/03/2019

Spécialité:

Optique, Lasers, Physico-Chimie, Atmosphère

---

# Aerosol hygroscopic properties: a laboratory approach for single and multi-component inorganic particles of atmospheric relevance

---

Alfons Schwarzenboeck	Professeur	LaMP, Clermont-Ferrand	Rapporteur
Jean Sciare	Professeur	The Cyprus Institute, Nicosie	Rapporteur
Stéphane Alfaro	Professeur	LISA, Paris	Examineur
Cyrielle Denjean	Chargée de Recherche	CNRM, Toulouse	Examinatrice
Denis Petitprez	Professeur	PC2A, Lille	Examineur
Marie Choël	Maître de conférences	LASIR, Lille	Encadrante
Suzanne Crumeyrolle	Maître de conférences	LOA, Lille	Encadrante
Isabelle Chiapello	Chargé de Recherche, CNRS	LOA, Lille	Directrice de thèse

Laboratoire d'Optique Atmosphérique (Département de Physique)

et

Laboratoire de Spectrochimie Infrarouge et Raman (Département de Chimie)

59655 Villeneuve d'Ascq, France





## Thèse de Doctorat

Présentée Par:

**Danielle EL HAJJ**

pour l'obtention du grade de Docteur de l'Université de Lille

Spécialité:

Optique, Lasers, Physico-Chimie, Atmosphère

---

# Propriétés hygroscopiques des aérosols: études en laboratoire de particules inorganiques pures et mélangées d'intérêt atmosphérique

---

Alfons Schwarzenboeck	Professeur	LaMP, Clermont-Ferrand	Rapporteur
Jean Sciare	Professeur	The Cyprus Institute, Nicosie	Rapporteur
Stéphane Alfaro	Professeur	LISA, Paris	Examineur
Cyrielle Denjean	Chargée de Recherche	CNRM, Toulouse	Examinatrice
Denis Petitprez	Professeur	PC2A, Lille	Examineur
Marie Choël	Maître de conférences	LASIR, Lille	Encadrante
Suzanne Crumeyrolle	Maître de conférences	LOA, Lille	Encadrante
Isabelle Chiapello	Chargé de Recherche, CNRS	LOA, Lille	Directrice de thèse

Laboratoire d'Optique Atmosphérique (Département de Physique)

et

Laboratoire de Spectrochimie Infrarouge et Raman (Département de Chimie)

59655 Villeneuve d'Ascq, France



---

# Acknowledgement

---

I want to express my respect and appreciation to my director and my two supervisors, Isabelle Chiapello, Marie Choël and Suzanne Crumeyrolle for their advices and ideas to overcome obstacles.

I would also like to thank my committee members Alfons Schwarzenboeck, Jean Sciare, Stéphane Alfaro, Cyrielle Denjean and Denis Petitprez for their continued support and encouragement and their well focused questions.

A big thank you goes out to the directors of the two laboratories LOA and LASIR, Frédéric Parol and Hervé Vezin, for hosting me.

I would also like to acknowledge my co-funders: the LABEX Cappa and the Region Haut de France.

I wish to acknowledge and thank my friends for their love and support.

Finally, I must express my very profound gratitude to my family for providing me continuous encouragement throughout my years of study.

---

# Résumé

---

Les aérosols atmosphériques jouent un rôle essentiel sur l'équilibre énergétique de la planète et ont également un impact important sur la santé humaine. Le dernier rapport d'évaluation du Groupe d'Experts Intergouvernemental sur l'Evolution du Climat (GIEC) souligne que le niveau d'incertitude associé aux estimations du forçage radiatif des aérosols, par effet direct et indirects, reste particulièrement élevé. En effet, les impacts des aérosols sont directement liés à leurs propriétés physico-chimiques et optiques, qui évoluent constamment dans l'atmosphère. En particulier, une humidité relative (RH) élevée augmente la quantité de vapeur d'eau captée par les particules d'aérosol atmosphériques, ce qui modifie leurs tailles, leurs morphologies et leurs composition chimiques et donc leurs propriétés optiques.

Le but de cette thèse est (1) d'étudier l'évolution des propriétés optiques (diffusion), chimiques et physiques (taille) des aérosols à différentes humidités, en s'appuyant sur des mesures de laboratoire à humidité contrôlée et (2) de comparer ces données expérimentales avec les résultats de modèles thermodynamiques et de paramétrisations (Zdanovskii-Stokes-Robinson, ZSR), couramment utilisés, permettant d'estimer la quantité de vapeur d'eau condensée sur les aérosols. Pour atteindre ces objectifs, des aérosols inorganiques purs et mélangés, représentatifs des particules les plus abondantes dans l'atmosphère, ont été générés en laboratoire, tels que des particules de chlorure de sodium ( $NaCl$ ), de sulfate d'ammonium ( $(NH_4)_2SO_4$ ), de nitrate de sodium ( $NaNO_3$ ) et le chlorure de potassium ( $KCl$ ). Deux dispositifs instrumentaux permettant une caractérisation des propriétés de ces aérosols en fonction de l'humidité ont été utilisés : le premier basé sur des mesures in-situ (néphélomètre et compteur optique de particules) d'une population d'aérosols, le second s'appuyant sur des mesures de microscopie optique et spectrométrie Raman) à l'échelle de la particule.

La relation ZSR, qui permet de prédire la croissance hygroscopique de l'aérosol a été appliquée aux résultats des mélanges d'aérosols et comparée aux mesures expérimentales. Les écarts constatés entre ZSR et observations sont relativement importants quelle que soit la gamme d'humidité relative, avec une sous-estimation avant le  $DRH_{mélange}$  et une sur-estimation après le  $DRH_{mélange}$ . De plus, le point de déliquescence d'un mélange d'aérosols ( $DRH_{mélange}$ ) est toujours plus bas que les DRH des composés purs. Une relation linéaire

telle que la ZSR est donc incapable de reproduire ce comportement. C'est pourquoi une meilleure caractérisation du  $\text{DRH}_{\text{mélange}}$  est nécessaire. Cependant, la comparaison des résultats de modèles thermodynamiques (E-AIM) avec nos observations met en évidence que la formation de nouvelles espèces ainsi que la modification de leurs phases vont modifier ce  $\text{DRH}_{\text{mélange}}$ . Dès lors, nos résultats montrent la complexité de représenter, de manière robuste, l'évolution d'un mélange binaire d'aérosol en fonction de l'humidité relative. Cette thèse s'étant exclusivement basée sur les paramètres hygroscopiques d'aérosols générés et mesurés en laboratoire, la prise de compte des modifications affectant les aérosols présents en atmosphère réelle, encore plus complexe apparaît donc difficile.

---

# Abstract

---

Atmospheric aerosols play a crucial role in the global energy balance and also have a significant impact on human health. The latest assessment report of the Intergovernmental Panel on Climate Change (IPCC) emphasizes that the level of uncertainty associated to estimates of aerosols radiative forcing, due to direct and indirect effects, is particularly high. Indeed, aerosols impacts are directly related to their physico-chemical and optical properties, that constantly evolve in the atmosphere. In particular, high relative humidity (RH) increases the amount of water vapor adsorbed by atmospheric aerosol particles, which modifies their sizes, their morphologies and their chemical compositions and thus their optical properties.

The aim of this thesis is (1) to study the evolution of the optical (scattering), chemical and physical properties of aerosols at different humidities, based on humidity-controlled laboratory measurements and (2) to compare these experimental data set with the results of commonly used thermodynamic models and parametrizations (E-AIM, Zdanovskii-Stokes-Robinson, ZSR herein) to estimate the amount of water vapor condensed on aerosols. To achieve these objectives, pure aerosols and mixed inorganic aerosols have been generated in laboratory, such as particles of sodium chloride ( $NaCl$ ), ammonium sulphate ( $(NH_4)_2SO_4$ ), sodium nitrate ( $NaNO_3$ ) and potassium chloride ( $KCl$ ). Two instrumental systems allowing a characterization of aerosol properties as a function of humidity have been used: the first one based on in-situ measurements (nephelometer and Optical Particle Counter) of an aerosol population and the second one based on optical microscopy and Raman microspectrometry of a single particle.

The ZSR relationship, which allows to predict the aerosol hygroscopic growth, has been applied to binary aerosol mixtures and compared to results of experimental measurements. The differences in hygroscopic growth observed between ZSR and observations are relatively important whatever the RH range, with underestimation before the  $DRH_{mixture}$  and an overestimation after the  $DRH_{mixture}$ . Moreover, the point of deliquescence of a mixture ( $DRH_{mixture}$ ) is always lower than the DRH of pure compounds. A linear relation such as the ZSR is thus incapable of reproducing this behavior. This is why a better characterization of the  $DRH_{mixture}$  is necessary. However, comparing the results of thermodynamic

models (E-AIM) with our observations shows that the formation of new species and modification of their phases will modify this  $DRH_{mixture}$ . Thus, our results show the complexity of representing, in a robust way, the evolution of a binary aerosol mixture as a function of relative humidity. This thesis being entirely based on hygroscopic parameters of aerosols generated and measured in laboratory, an accurate representation of modifications affecting aerosols present in real atmosphere, with a higher level of complexity appears to be highly challenging.



---

# Contents

---

<b>Introduction</b>	<b>14</b>
<b>Chapter 1 Aerosols characteristics and hygroscopic properties</b>	<b>28</b>
1.1 Physical properties . . . . .	30
1.2 Chemical properties and aging . . . . .	33
1.3 Optical properties . . . . .	36
1.3.1 Extinction, scattering and absorption coefficients . . . . .	36
1.3.2 Refractive index . . . . .	39
1.4 Hygroscopic properties . . . . .	39
1.4.1 Hygroscopic conditions and phase transitions . . . . .	40
1.4.1.1 Köhler's theory . . . . .	41
1.4.1.2 Sub-saturation (RH<100%) . . . . .	42
1.4.2 Hygroscopic factors . . . . .	47
1.4.2.1 Growth Factor $g(\text{RH})$ . . . . .	47
1.4.2.2 Scattering enhancement factor $f(\text{RH})$ . . . . .	48
1.4.2.3 Link between Hygroscopic factors . . . . .	49
1.4.3 Aerosols thermodynamic models . . . . .	51
1.4.4 Application of ZSR relation (Zdanovskii-Stokes-Robinson) to multi- component aerosols . . . . .	53
1.5 Conclusion . . . . .	55
<b>Chapter 2 Methodology and instrumentation</b>	<b>58</b>
2.1 Experiment 1: Size and optical properties of aerosol population . . . . .	60
2.1.1 Aerosol size distribution measured by Optical Particle Counters (OPC)	63

2.1.2	Aerosol scattering coefficient measured by Nephelometer . . . . .	65
2.2	Experiment 2: Physico-chemical properties of a single particle . . . . .	68
2.2.1	Levitation system: Acoustic levitation . . . . .	69
2.2.2	Aerosol chemical composition and physical properties . . . . .	71
2.3	Conclusion . . . . .	75
<b>Chapter 3</b>	<b>Hygroscopic growth properties of pure aerosols</b>	<b>76</b>
3.1	Determination of the DRH . . . . .	78
3.1.1	Aerosol population . . . . .	79
3.1.2	Single particle . . . . .	81
3.2	Effect of RH on aerosol population diameter . . . . .	84
3.3	Hygroscopic growth factor measurements . . . . .	87
3.4	Conclusion . . . . .	89
<b>Chapter 4</b>	<b>Hygroscopic behavior of mixed aerosol population</b>	<b>92</b>
4.1	Mixing of 3 ions . . . . .	93
4.1.1	NaCl/KCl mixing . . . . .	94
4.1.1.1	Experimental results . . . . .	94
4.1.1.2	Comparison to the ZSR . . . . .	96
4.1.2	NaCl/NaNO <sub>3</sub> mixing . . . . .	98
4.1.2.1	Experimental results . . . . .	98
4.1.2.2	Comparison to the ZSR . . . . .	100
4.2	Mixing of more than 3 ions . . . . .	102
4.2.1	Experimental results . . . . .	103
4.2.2	Comparison to the ZSR . . . . .	105
4.3	Conclusion . . . . .	108
<b>Chapter 5</b>	<b>Hygroscopic behavior of internally mixed single particles of NaCl/(NH<sub>4</sub>)<sub>2</sub>SO<sub>4</sub></b>	<b>110</b>
5.1	Phase transitions and growth factors analysis . . . . .	112
5.2	Comparison of experimental results with E-AIM model . . . . .	116

5.3	Aerosol composition modifications . . . . .	120
5.3.1	Analysis with Raman microspectrometry . . . . .	120
5.3.2	E-AIM calculation of MDRH and DRH . . . . .	123
5.4	Discussion . . . . .	126
	<b>Conclusion and perspectives</b>	<b>130</b>
	<b>Annex</b>	<b>138</b>
	<b>Bibliography</b>	<b>184</b>



---

# Introduction

---

### **Scientific context and current uncertainties related to aerosols**

One of the most important environmental issues facing our societies is the understanding of climate and weather systems and their current and future changes (IPCC, 2018). The first collective awareness of the effect of human activities on the atmospheric composition became apparent with the discovery of identifiable events such as acid rain, the hole in the ozone layer or the transport of radioactive particles. As a large part of humanity is potentially exposed to the harmful effects of the forthcoming climatic changes, a better understanding of the environmental problems we have to face is needed. Due to these complex modifications of our ambient environment in the last decades, the scientific community has made a lot of effort to refine its knowledge on the physico-chemical mechanisms that take place in the atmosphere.

The scientific consensus advocating the impact of humans on the atmosphere was made public in the first reports of the “Groupe d’Experts Intergouvernemental sur l’Evolution du Climat” (GIEC or IPCC) in 1990 and 1995. These reports make the connection between the rise of the sea level and the global ice melt, the rise in temperatures ( $+0.74^{\circ}\text{C}$  between 1906 and 2005, IPCC, 2007) and the increase in anthropogenic greenhouse gases. The overall impact of present-day atmospheric aerosols is estimated to be cooling, globally counterbalancing a significant fraction of the warming associated with greenhouse gases (IPCC, 2013). Thus, aerosols particles, both natural and anthropogenic, have been deeply investigated in the last decades, both because of their environmental health impacts on population and because they are radiatively active components of the Earth’s atmosphere. They exert a direct radiative effect by scattering and absorbing solar and infrared radiation. This phenomenon leads to a cooling or a warming effect of the atmospheric layers. This is known as the aerosol direct radiative effect. The local warming effect due to absorbing particles also induces changes in the vertical temperature profiles, relative humidity, and stability of the atmospheric column, that modifies the cloud formation conditions (Ramanathan et al., 2001; Boucher et al., 2013). This effect is known as the semi-direct effect. Robust estimation of the direct radiative forcing requires an accurate knowledge of the aerosol properties, as well as their variabilities in space and time (Solomon et al., 2007). The global annual aerosol

radiative forcing due to direct radiative effect has been estimated to  $-0.35 \text{ W.m}^{-2}$  with an uncertainty range of  $-0.85$  to  $+0.15 \text{ W.m}^{-2}$  (Figure 1, Myhre et al. (2013b)).

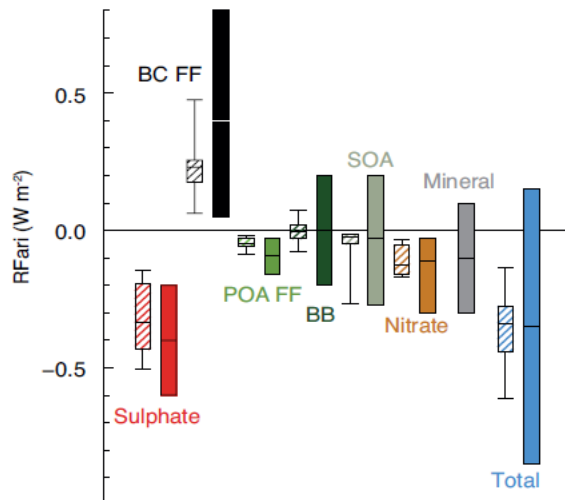


**Figure 1:** Annual mean top of the atmospheric radiative forcing of aerosol-radiation interactions due to different anthropogenic aerosol types, for the 1750-2010 period. Hatched whisker boxes show median (line), 5th to 95th percentiles (box) and min/max values (whiskers) from AeroCom II models Myhre et al. (2013a). Solid colour boxes show the AR5 (Fifth Assessment Report) best estimates and 90% uncertainty ranges. BC FF represents black carbon from fossil fuel and biofuel; POA FF, primary organic aerosol from fossil fuel and biofuel; BB, aerosols from biomass burning; SOA, secondary organic aerosols from Boucher et al. (2013).

Moreover, due to their ability to act as cloud condensation nuclei (CCN) and ice nuclei (IN) aerosols interact with clouds, and influence their radiative properties through different processes known as indirect radiative effects. A CCN increase from anthropogenic aerosols leads to a larger number of cloud droplets and, assuming constant liquid water content, smaller cloud droplet sizes (Boucher, 2015). The increasing number of droplets in turn increases the cloud albedo called the first aerosol indirect effect (Twomey, 1977). Moreover, the smaller cloud droplet sizes lead to a delay precipitation, which may further alter cloud properties

such as its lifetime. This is known as the second indirect effect described by [Albrecht \(1989\)](#). Importantly, aerosol-cloud interactions continue to constitute a major source of uncertainty for the estimate of climate radiative forcing ([Myhre et al., 2013b](#)).

The large uncertainties associated to current estimates of atmospheric aerosol direct, semi-direct and indirect radiative effects are largely due to a partial knowledge of aerosol properties, which are intrinsically highly variable. Indeed, atmospheric aerosols encompass a large variety of aerosol types, considering their origin (natural, anthropogenic), chemical composition and size ranges. Moreover, these particles, during their transport in the atmosphere, are subject to aging processes upon interactions between particles and gases, making their physical, chemical, optical and hygroscopic properties constantly evolving ([Zhang et al., 2000a](#)). Especially, atmospheric particles are sites of (i) condensation of non-volatile or semi-volatile gaseous compounds formed by photochemical reaction ([Hodzic et al., 2010](#)), (ii) heterogeneous chemical reactions on their surface ([Wang et al., 2010](#)), and (iii) cloud cycles leading to significant changes in their size and composition ([Adler et al., 2013](#)). It is therefore important to understand the life cycle of atmospheric aerosols and to be able to quantify their sources, sinks and transformations during transport in the atmosphere. This is a complex task as most aerosols present in the atmosphere are a heterogeneous mixture of particles of various origin, size, and chemical composition, characterized by a high spatial and temporal variability, due to their relatively short lifetimes in the troposphere (from days to weeks ([Ramanathan et al., 2001](#))). Robust and coordinated measurements of aerosol particle optical properties (i.e. scattering and absorption) together with measurements of their physical and chemical properties are fundamental for improving our knowledge of their life cycle, environmental health and climate impacts. Such a strategy is currently being developed, as for example in the context of ACTRIS observatories in Europe ([Pandolfi et al., 2018](#)). It is important to note that at the majority of ACTRIS observatories, the aerosol particle light-scattering measurements are taken at a low relative humidity (RH <40%), to ensure that the data are comparable across the network.

Due to the variability of ambient relative humidity (RH), aerosols may take up water, thus changing their size ([Winkler, 1973](#)), mass ([Pilinis et al., 1989](#)), chemical composition ([Covert](#)

et al., 1972), and associated light scattering coefficient (Schuster et al., 2009; Zieger et al., 2013; Titos et al., 2016). Importantly, depending on their initial size distribution and chemical composition, the water uptake by aerosol particles will increase their size relative to their dry equivalents, leading them to scatter more light (Titos et al., 2016). Lifetime and their activity as CCN are also modified, with subsequent impacts on the aerosol indirect radiative forcing (Ziemba et al., 2013). Aerosol hygroscopicity is also an important parameter to take into account, for assessing surface air quality (particulate matter concentration) from satellite remote sensing observations, which are made at ambient RH (Crumeyrole et al., 2014), as attempted by several studies (Kacenenbogen et al., 2006; Hoff and Christopher, 2009). Indeed, typical in-situ microphysical and optical measurements are made at relatively low relative humidity (RH <40%, (Collaud Coen et al., 2013)) meaning that they are not representative of ambient conditions (Titos et al., 2014, 2016). Currently, aerosol liquid water content (ALWC) is not systematically measured at the ground sites of the global atmosphere watch (GAW) network nor on a global scale, so many studies either neglect or estimate the humidity effect when parameterizing the relationship between satellite derived AOD and PM<sub>2.5</sub> (Schaap et al., 2009). Given the potential of utilizing satellite-based observations to monitor particulate air-quality regionally and throughout the world, several studies have investigated how humidity impacts these approaches, notably during field-campaigns (Ziemba et al., 2013; Crumeyrole et al., 2014).

As an example, Figure 2 shows the diurnal variation of the relative humidity measured in the ambient air (in Lille) and in the nephelometer (part of the atmospheric platform of measurements located in the roof of LOA laboratory, University of Lille) for the years 2015-2016. These data illustrate that the relative humidity in the ambient air reaches values up to 90% (red curve), while it varies between 28 and 40% in the nephelometer (black curve). Therefore, the use of in-situ techniques with variable relative humidity measurements ability is highly needed in order to be representative of the real atmospheric conditions and study the relative humidity effects on atmospheric aerosol properties.

In a general point of view, many studies have highlighted that the role of RH on aerosol

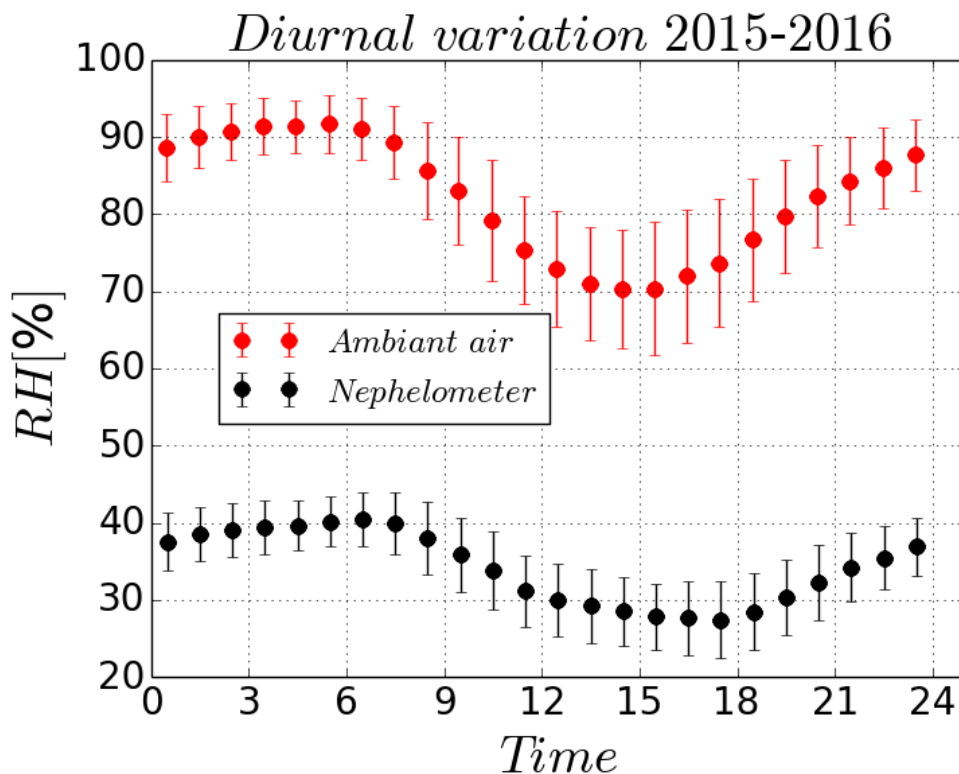


**Figure 2:** *Diurnal variation of the relative humidity measured by the DAVIS meteo station and inside the nephelometer at the roof top of LOA for 2015-2016.*

optical properties, as well as applications to the direct and indirect effects of aerosols on the Earth’s radiative balance is fundamental (Tang and Munkelwitz, 1994b; Tang, 1996a; Kotchenruther et al., 1999; Yoon and Kim, 2006; Cheng et al., 2008; Massoli et al., 2009; Liu et al., 2009, 2010). Additionally, horizontal visibility will be worsened when RH is higher with the same level of aerosol mass concentration (Malm and Day, 2001).

### **Aerosol hygroscopicity: from field measurements to parameterizations**

Due to the importance of humidification process, a number of studies have investigated the change in size of aerosol particles due to water uptake, in particular by using the common Humidified Tandem Differential Mobility Analysers (HTDMA) technique, as for example Massling et al. (2007) during the ACE-Asia (Aerosol Characterization Experiment - Asia)

field campaign in 2001, or [Meier et al. \(2009\)](#) and [Wu et al. \(2013\)](#) in other environments. HTDMAs were firstly introduced by [Liu et al. \(1978\)](#) and have been used worldwide not only during field campaigns but also in laboratory experiments ([Prenni et al., 2003](#); [Meyer et al., 2009](#); [Denjean et al., 2014](#)). The parameter determined is the particle growth factor (named GF or  $g(\text{RH})$  depending on studies), i.e. the ratio of the particle diameter at a given RH to the particle diameter under low RH condition. As a limitation of HTDMA, measurements of  $g(\text{RH})$  are usually performed for a single size class.

It is also possible to measure directly the enhancement of the scattering coefficient due to water uptake by means of a tandem of nephelometer setup ([Fierz-Schmidhauser et al., 2010b](#)). The combination of both measurements, one at a reference RH (usually between 20 and 40%), the second at a high RH (up to 90%), allows to derive the scattering enhancement factor ( $f(\text{RH})$ ). This factor, which is relevant for climate studies, quantifies the amount of change of the particle light-scattering coefficient due to water uptake ([Titos et al., 2014](#)). As illustrated in [Table 1](#), which summarizes scattering enhancement factors from the literature, aerosol particles encountered in typical atmospheric environments have different hygroscopic properties. Especially, [Table 1](#) highlights that, for RH between 80 and 85%, in clean marine and maritime aerosol conditions  $f(\text{RH})$  values vary between 2.2 and 3, whereas  $f(\text{RH})$  values are generally lower, in the range 1.2-1.59 for dust dominated conditions.

Some recent studies, for example in northern Italy ([Adam et al., 2012](#)) and central France ([Holmgren et al., 2014](#)), have investigated aerosol hygroscopicity over periods of months to years based on HTDMA measurements, confirming the important variability of particles hygroscopicity according to location, air mass and associated dominant aerosol type, or season. Recently, during the DACCIIWA (Dynamics-Aerosol-Chemistry-Cloud interactions in West Africa) field campaign in West Africa (June-July 2016), aircraft and radiosonde data were used to estimate the hygroscopic growth of aerosols under different RH conditions. This approach has shown that, in this region, the presence of highly humid layers during the monsoon season has a high impact on aerosol optical depth, which may undergo an exponential increase as a function of RH ([Haslett et al., 2019](#)).

**Table 1:** *Hygroscopic growth factors from the literature measured for different aerosol types. The values of  $f(RH)$  correspond to the ratio of the aerosol light-scattering coefficient (near 550 nm wavelength) at high RH and at dry conditions ( $RH < 40\%$ ). From Titos et al. (2014).*

Observation site	Predominant aerosol	$f(RH)$	Reference
Cape Cod (MA, USA)	Clean marine	$f(80\%)=2.2$	Titos et al. (2014a)
Mace Head (Ireland)	Clean marine	$f(85\%)=2.2$	Fierz-Schmidhauser et al. (2010c)
Cabauw (The Netherlands)	Maritime	$f(85\%)=3$	Zieger et al. (2011)
Ny-Ålesund (NORWAY)	Arctic	$f(85\%)=2.35$	Zieger et al. (2010)
Southern Great Plains (OK, USA)	Continental	$f(85\%)=1.83$	Sheridan et al. (2001)
Bondville (IL, USA)	Continental	$f(82.5\%)=1.4-1.5$	Koloutsou-Vakakis et al. (2001)
Xin’An (China)	Dust dominated	$f(80\%)=1.2$	Pan et al. (2009)
Jungfraujoch (Switzerland)	Dust dominated	$f(85\%)=1.3$	Fierz-Schmidhauser et al. (2010b)
Southern Great Plains (OK, USA)	Dust dominated	$f(85\%)=1.59$	Sheridan et al. (2001)
Granada (Spain)	Dust dominated	$f(85\%)=1.3$	Titos et al. (2014)
Beijing (China)	Urban	$f(80\%-85\%)=1.26$	Yan et al. (2009)
Xin’An (China)	Urban pollution	$f(80\%)=1.57$	Pan et al. (2009)
Granada (Spain)	Urban	$f(85\%)1.6$	Titos et al. (2014)

Former global modeling studies dedicated to aerosols radiative effects have highlighted the importance of taking into account the variation of aerosols spectral optical properties with relative humidity (Grant et al., 1999). In the context of AeroCom intercomparison exercise of sixteen global aerosol models, Textor et al. (2006) have shown that various parametrizations of different complexity are used to describe water uptake by aerosol particles in the ambient atmosphere. These authors also highlight an extremely high diversity for the uptake of ambient water vapor that influences the particle size and other related processes (for example sink rate coefficients). Therefore, to help reducing the high diversity in current aerosol modeling studies for the water uptake, there is an urgent need to better constrain aerosol hygroscopicity parameterizations. Especially, using well-controlled laboratory experiments will contribute to a better understanding of fundamental processes occurring during humid-

ification and allow to test the robustness of current parameterizations of hygroscopicity in models.

Based on in situ measurements of aerosol optical and hygroscopic properties during a cruise in the Gulf of Mexico (TexAQS-GoMACCS, Texas Air Quality Study-Gulf of Mexico Atmospheric Composition and Climate Study), [Massoli et al. \(2009\)](#) have shown that including aerosol hygroscopic properties in climate calculations is critical for improving estimates of aerosol forcing on climate. Most aerosol models use the Zdanovskii-Stokes-Robinson (ZSR) ([Stokes and Robinson, 1966](#); [Clegg and Seinfeld, 2004](#)) method to determine the amount of condensed water at the surface of the particles ([Choi and Chan, 2002](#); [Svenningsson et al., 2006](#)) and rely on Mie codes to determine the refractive index of the wet aerosol ([Bond et al., 2006](#); [Bohren and Huffman, 2008](#)). The ZSR method, which allows to predict water uptake of pure and mixed aerosols, is relatively simple and relies on the assumption that individual compounds in a solution do not interact. In most cases, the ZSR mixing rule works fairly well, especially in describing the water uptake of both organic-organic and organic-inorganic aerosol mixtures, however there are large deviations in some other cases ([Kanakidou et al., 2005](#)). Especially, [Svenningsson et al. \(2006\)](#) have tested the ZSR mixing rule on the hygroscopic growth for mixed aerosol particles of inorganic and organic compounds of atmospheric relevance. Using a HTDMA instrument and a CCN spectrometer, these authors have shown in their laboratory experiment that, for mixtures including sodium chloride (a proxy for sea salt aerosols), hygroscopic growth showed a pronounced deviation from the ZSR mixing rule ([Svenningsson et al., 2006](#)). It can be noticed that these authors also reported deviations from ZSR for ammonium sulfate/sodium chloride mixtures, found in a previous study by [Cohen et al. \(1987\)](#).

### **Laboratory experiments and the complexity of aerosol mixtures**

Sea spray being both one of the most abundant natural aerosol specie in the atmosphere and an inherently hygroscopic aerosol type (as previously illustrated in [Table 1](#), with values of  $f(\text{RH})$ ), effects of humidity on sea salt particles and/or sodium chloride have been the subject of many studies ([Tang et al., 1997](#); [Wise et al., 2007, 2009](#); [Prather et al., 2013](#);

Zieger et al., 2017). Despite these efforts from the scientific community, the hygroscopicity of marine aerosols remains not fully understood, especially when NaCl is mixed with other inorganic compounds. Recent investigations focusing on inorganic sea salt particles continue to highlight the need to continuously constrain hygroscopicity parameterization implemented in aerosol models, in order to provide robust estimates of aerosol–radiation interactions (Zieger et al., 2017).

Some studies have examined the hygroscopic properties of aerosol mixtures of two inorganic salts having one ion in common (Tang et al., 1978; Tang and Munkelwitz, 1993, 1994a; Chang and Lee, 2002). Their results have shown that a three ions system is quite complex and the deliquescence point is clearly depending on the temperature as well as on the ions within the mixing. Tang et al. (1978) also concluded that field measurements should be cautiously interpreted when attempting to relate the measured growth of an unknown atmospheric aerosol to its chemical composition. Chang and Lee (2002) have shown large differences between measured values of deliquescence characteristics and thermodynamical model predictions for different molar fractions of aerosol mixtures having an ion in common, like  $NaCl/Na_2SO_4$ . Other studies have focused on the hygroscopicity of salt particles mixed with organic acids (Zardini et al., 2008; Ma et al., 2013; Jing et al., 2018), their results showing good agreement between the ZSR method and experimental data.

In general, it is now established that the mixing state of different inorganic salts with multiple ions remains uncertain. Indeed, adding a salt to another may strongly affect the hygroscopic behavior of the resulting aerosol mixture, modifying the deliquescence curve from one to two phase transitions, characterized by a MDRH (Mutual Deliquescence Relative Humidity) and a DRH (Seinfeld and Pandis, 2006). Moreover, while changes of particle size, water content and morphology during humidifying-dehumidifying are generally characterized, the chemical reactions that can be produced between coexisting components in mixed aerosol species have been largely neglected and not fully identified and quantified (Ma et al., 2013). To date, all the existing studies based on synthetic aerosols in chamber or laboratory experiments have been limited to (i) measurements of the physical and optical properties (HTDMA and Nephelometer, (Denjean et al., 2014)) dedicated to better understand the strength and

weakness of ZSR method or (ii) measurements of the physical and chemical properties (Optical microscopy and Raman microspectrometry (Yeung et al., 2009; Gupta et al., 2015; Tobon et al., 2017)) allowing observations of the mutual deliquescence point. Up to now, to our best knowledge, no study has attempted to investigate and measure the evolution of both aerosol optical/physical and chemical properties with increasing RH, based on synthetic aerosol mixtures with known chemical composition using a laboratory approach. One important advantage of this kind of approach, which relies on combination of different experimental techniques is that it is expected to lead to a more comprehensive understanding of the physico-chemical transformations that occur during the humidifying process of multiple ions mixtures.

### **Gaps of knowledge - Thesis objectives**

Particles of marine origin are among the most abundant aerosols in the atmosphere, due to the large production of sea spray over the open ocean (Seinfeld and Pandis, 2006). As underlined in the review of Meskhidze et al. (2013), the current understanding of the hygroscopic properties of ambient sea-salt aerosols is evaluated as “low”. Both *NaCl* (which constitutes around 80% of sea salts by mass) behavior and the contributions from other constituents, such as  $SO_4^{2-}$ , or other non-sea-salt species must be investigated. In this context, the main objective of this thesis is to contribute to a better understanding of the factors influencing the hygroscopic properties of pure sodium chloride (*NaCl*), potassium chloride (*KCl*), ammonium sulfate ( $(NH_4)_2SO_4$ ), and sodium nitrate (*NaNO\_3*), and a mixing of these salts. We will investigate the hygroscopic properties of these pure and mixed aerosol components and contribute to test the applicability of the ZSR method for aerosol inorganic mixtures composed of three and more than three ions. Deviations of the  $g(RH)$  retrieved by the ZSR method compared to laboratory measurements, found in previous experiments (Svenningsson et al., 2006), must be investigated for salt mixtures, especially those composed of three or more ions. Compared to previous investigations, one of the interests of the approach we propose in this thesis is that it will allow to analyze the evolution of aerosol chemical composition during the humidifying process. The methodology chosen is based on a laboratory experi-

mental approach, which combines several techniques that, to our best knowledge, have never been used together in the same study. Thus, we aim to perform aerosol hygroscopicity analysis for both single particles (optical microscopy) and aerosol populations (nephelometry). Additionally, these complementary measurements have the advantage to provide evolution of aerosol physical (i.e., size, based on optical microscopy), optical (i.e, scattering properties through Nephelometer measurements) and chemical (through Raman microspectrometry) properties for different humidity conditions. By using an humidificator-VDM (Vapor Delivery Model), we perform a humidification of particles with RH varying between around 30 and 90%. Using our instrumental setup, we examine several fundamental properties of aerosol hygroscopicity:  $f(\text{RH})$ ,  $g(\text{RH})$ , and phase transitions with experimentally measured DRH (deliquescence relative humidity) and MDRH (mutual DRH). For different types of aerosol mixtures and selected molar fractions, including the mixing of 3 ions ( $\text{NaCl}/\text{KCl}$ ,  $\text{NaCl}/\text{NaNO}_3$ ) or more ( $\text{NaCl}/(\text{NH}_4)_2\text{SO}_4$ ), our results are compared to ZSR, and E-AIM (Extended-Aerosol Inorganics Model) thermodynamic models (model calculations), which allow to predict DRH and MDRH.

The first chapter presents a scientific background of our current knowledge of aerosols and their properties, with special emphasis on their hygroscopic properties. Chapter 2 describes the different techniques and instruments used in this thesis including the systems for generating synthetic aerosols and devices for measuring aerosol optical, physical and chemical properties at dry conditions and at different relative humidities. Chapter 3 is dedicated to the measurement of aerosol properties at variable relative humidities for a single component aerosol or pure aerosol using two approaches. The first approach relies on the measurement of aerosol optical properties (i.e. scattering coefficient by nephelometry) for an aerosol population and the second one is based on the measurement of physical properties (i.e. particle size measurement from optical images) of single particles. Different pure aerosol species are studied, i.e, sodium chloride ( $\text{NaCl}$ ), ammonium sulfate ( $(\text{NH}_4)_2\text{SO}_4$ ), potassium chloride ( $\text{KCl}$ ), and sodium nitrate ( $\text{NaNO}_3$ ). In Chapter 4, we investigate the hygroscopic behavior of different aerosol mixtures, based on the use of measurement of scattering coefficient by nephelometry. In a first part, two types of mixtures are studied, i.e. the mixing of

*NaCl/KCl* and that of *NaCl/NaNO<sub>3</sub>* both composed of three ions. In a second part, we investigate the mixing of *NaCl* and *(NH<sub>4</sub>)<sub>2</sub>SO<sub>4</sub>* aerosols, that is composed of more than three ions. A comparison of the experimental results obtained for these different aerosol mixtures with the ZSR method is performed. Finally, in Chapter 5 we investigate the hygroscopic behavior of internally mixed *NaCl/(NH<sub>4</sub>)<sub>2</sub>SO<sub>4</sub>* particles, based on the change in particle size with the variation of RH observed using optical microscopy. Our experimental results are compared to the E-AIM thermodynamical model, and Raman microspectrometry is used to understand the evolution of the chemical composition of the mixture during the humidifying process.



---

## CHAPTER 1

---

# Aerosols characteristics and hygroscopic properties

Atmospheric aerosols are defined as a population of particles (solid, liquid or their mixtures) suspended in a gaseous medium. Generally, atmospheric aerosols are separated into two main categories, according to their origin: first, particles of natural origin resulting from different sources of emissions (i.e., wind erosion, volcanic eruptions, biogenic emissions, bubbling ...); secondly, anthropogenic, aerosols generated by different human activities (i.e., combustion of fuels, heating, transport, agriculture ...). Additionally, whether natural or anthropogenic, atmospheric aerosols can be classified into two groups according to the associated emission process: primary particles and secondary particles. Aerosols emitted directly in solid form into the atmosphere are called primary aerosols, such as sea salts, desert dust, volcanic ash, soot [...]. Conversely, aerosols formed in the atmosphere by chemical reaction processes that convert condensable gas into particles are called secondary aerosols, such as sulfates, nitrates, and the majority of organic particles. It should be noted that the different emitted gases, that are aerosol precursors, can also be of natural and anthropogenic sources. For example, sulfur dioxide precursor of sulfate particles, can be emitted into the atmosphere by both anthropogenic activities (industrial) or natural sources like volcanoes.

Table 1.1 shows the amount of aerosol natural and anthropogenic emissions and aerosol precursors per year. According to this table, the sea spray (generating sea salt particles) and wind erosion (generating desert dust particles) are the main sources of natural aerosols in the atmosphere. Their emission fluxes are between 1000 and 6000 Tg/year. Biomass burning aerosols and industrial dusts contribute significantly to the total amount of anthropogenic aerosols, with emission fluxes reaching 90 and 130 Tg/year, respectively. A factor of 10 is assessed between the natural and the anthropogenic mass emissions of primary aerosols. Secondary aerosols are emitted in smaller mass concentrations compared to primary aerosols (Boucher, 2015).

These different types of particles have different physical and chemical properties. In general, primary aerosols are relatively large particles (i.e., with diameter greater than 1  $\mu\text{m}$ ) while secondary particles are considered as fine particles (i.e., submicronic). Moreover, their chemical compositions are depending both on their sources and on the physico-chemical processes

**Table 1.1:** *Approximate emission of aerosol particles flux in Tg/year. Tg = 10<sup>12</sup>g, C=Carbon, S=Sulfur, N=Nitrogen (Boucher, 2015).*

<b>Aerosol type</b>	<b>Emission flux (Tg/year)</b>
<b>Natural primary aerosols</b>	
Desert dust	1000 - 3000
Sea spray	1000 - 6000
Biomass burning aerosols	20 - 35
Biogenic aerosols	≈ 1000
- including bacteria	0.040 – 1.800
- including spores	30
<b>Precursors of natural secondary aerosols</b>	
Dimethylsulphide (DMS)	20 – 40 S
Volcanic SO <sub>2</sub>	6 – 20 S
Terpenes	40 - 400
<b>Anthropogenic primary aerosols</b>	
Industrial dust	40 – 130
Biomass-burning aerosols	50 – 90
Black carbon (from fossil fuel)	6 – 10
Organic carbon (from fossil fuel)	20 – 30
<b>Anthropogenic secondary aerosols</b>	
SO <sub>2</sub>	70 – 90 S
Volatile organic compounds (VOCs)	100 – 560 C
NH <sub>3</sub>	20 – 50 N
NO <sub>x</sub>	30 – 40 N

they will experience in the atmosphere. These processes (aging, heterogeneous chemistry, humidification for example) will also modify their size and related optical properties, thus contributing to the complexity and the variability of the aerosol particle characteristics present in the atmosphere.

## 1.1 Physical properties

Aerosol size distribution in the troposphere has been observed by Junge (1963) and formalized by Whitby (1978). According to Seinfeld and Pandis (1998), aerosol populations

are divided into four major dimensional modes: the nucleation or ultra fine ( $<10$  nm), the Aitken ( $10$  nm  $<D_p <100$  nm), accumulation ( $100$  nm  $<D_p <1$   $\mu$ m), and the coarse mode ( $>2.5$   $\mu$ m). Figure 1.1 highlights the different modes of the aerosol size distribution.

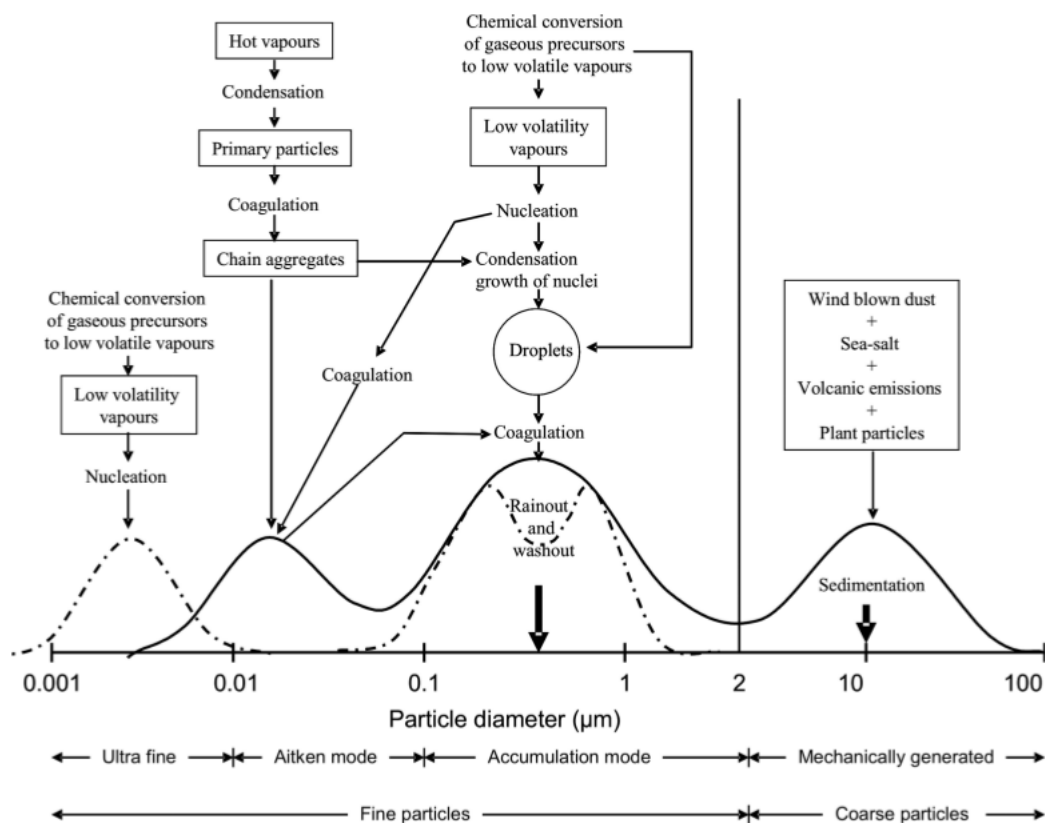


**Figure 1.1:** Description and process of formation of multimodal particle size distribution with typical transformations. From *Finlayson-Pitts and Hemminger (2000)*.

Knowledge of particle sizes is critical for an accurate description of their interactions with solar radiation. The aerosol sizes can be represented with a number, a surface area, and a volume size distribution, as represented in the following equations:

$$n_N(D_p) = \frac{dN}{dD_p}, \text{cm}^{-3} \quad (1.1)$$

$$n_S(D_p) = \frac{dS}{dD_p} = \pi D_p^2 n_N(D_p), \mu m^2 cm^{-3} \quad (1.2)$$

$$n_V(D_p) = \frac{dV}{dD_p} = \frac{\pi}{6} D_p^3 n_N(D_p), \mu m^3 cm^{-3} \quad (1.3)$$

In above equations  $D_p$  is the particle diameter,  $n_N(D_p)$ ,  $n_S(D_p)$  and  $n_V(D_p)$  are respectively the number, surface area, and volume concentrations of particles per volume of air. An integration should be applied to obtain the total number, surface area or volume of particles in this range.

In order to avoid scale problems, particle size distributions are usually given in logarithm scale. Thus, previous size distributions are usually expressed as follows:

$$n_N(\log D_p) = \frac{dN}{d\log D_p}, \quad n_S(\log D_p) = \frac{dS}{d\log D_p}, \quad n_V(\log D_p) = \frac{dV}{d\log D_p} \quad (1.4)$$

Figure 1.2 presents the number, surface area and volume size distributions of a rural continental aerosol population. The number size distribution shows two modes centered at about 0.02 and 0.08  $\mu m$ , and the volume distribution is characterized by a mode centered at about 7  $\mu m$  (Jaenicke, 1993). The number concentration of fine particles is greater than the one of the larger particles while the opposite is observed for their volume concentration. Therefore, the surface area and volume size distributions are shifted towards larger particle sizes. Particle number size distribution is generally used to highlight the fine particle modes, while the volume size distribution is used to highlight the coarse particle modes. Indeed, the mass concentration is proportional to the particle diameter to the cube. Finer particles, more numerous than the larger particles, do not contribute as much in terms of mass.

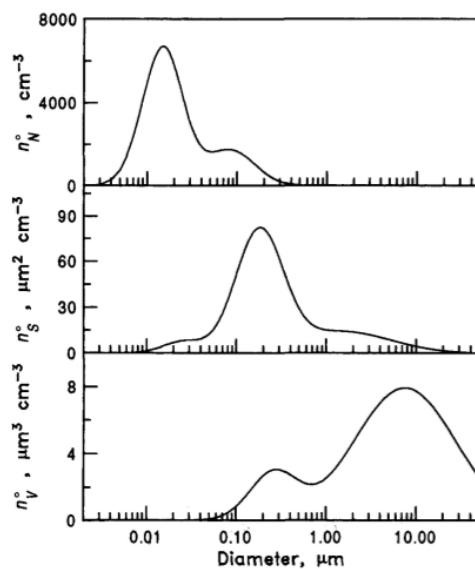


**Figure 1.2:** Particle size distribution in number, in surface area, and in volume of the same aerosol population (Seinfeld and Pandis, 1998),  $n_N^o$ ,  $n_S^o$ ,  $n_V^o$  represent respectively,  $n_N(\log D_p)$ ,  $n_S(\log D_p)$ , and  $n_V(\log D_p)$ .

## 1.2 Chemical properties and aging

Due to the diversity of natural and anthropogenic aerosol sources, a large variety of particles of different chemical composition are emitted into the atmosphere. Generally, aerosol chemical compounds are classified into the inorganic and the organic species. A third compound consists of soot or black carbon. The main inorganic compounds encompass species found in sea salt aerosols ( $NaCl$ ,  $KCl$ ), but also ammonium sulphate ( $(NH_4)_2SO_4$ ) and nitrate particles, and major elements like silica ( $Si$ ) and aluminum ( $Al$ ) found in mineral dust emitted by desert areas. Overall, in addition to sea salt and crustal aerosols, the inorganic aerosol fraction will include sulphates, nitrates, and ammonium resulting from the condensation of different precursor gases ( $SO_2$ ,  $NO_x$ ,  $NH_3$ ,...). Concerning the aerosol organic fraction, organic compounds and their concentrations remain poorly characterized (Cabada et al., 2004; Kanakidou et al., 2005) due to the multitude of organic compounds. Figure 1.3 illustrates the aerosol chemical composition of non-refractory submicron particles observed at various

locations. This figure highlights that organic aerosol fraction varies between 18 and 70% (average = 45%, Zhang et al. (2007)). Sulfate (10-67%, avg = 32%), nitrate (1.2-28%, avg = 10%), ammonium (6.9-19%, avg = 13%), and chloride (avg = 0.6%) account for the rest of the aerosol mass.

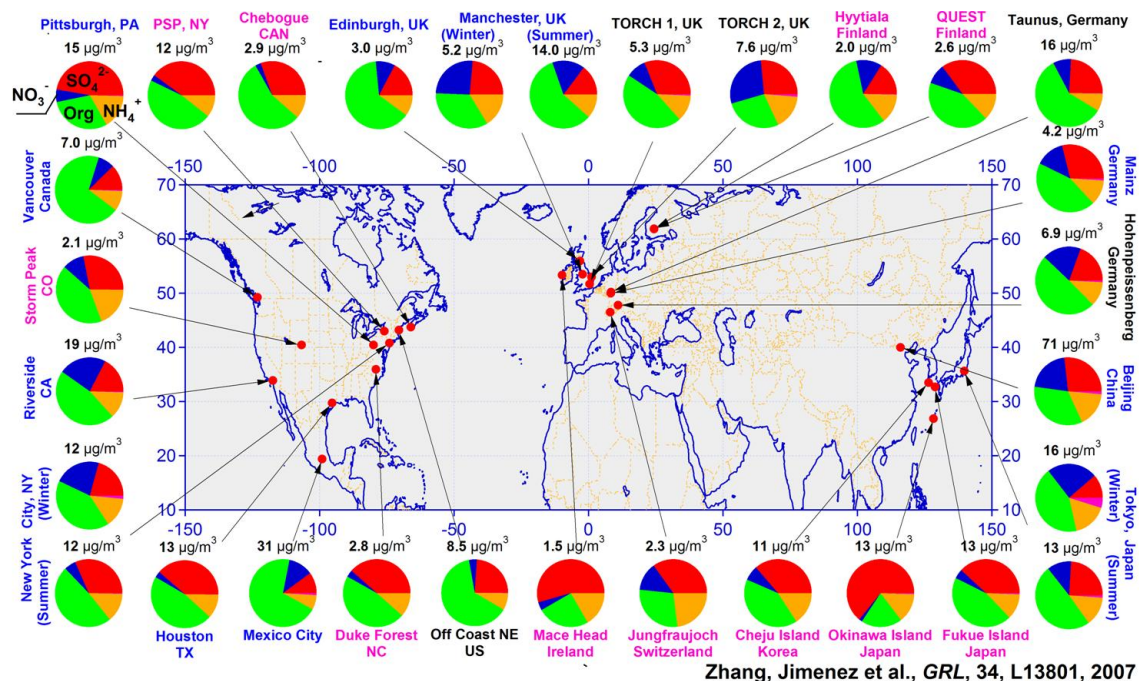


**Figure 1.3:** Pie charts of the average mass concentration and chemical composition of NR-PM1 (non refractive particulate matter of diameter less than 1 micron) derived from AMS (Aerosol Mass Spectrometer) datasets: organics (green), sulfate (red), nitrate (blue), ammonium (orange), and chloride (purple). From Zhang et al. (2007).

The hygroscopic behavior affects aerosol chemical composition since solubility is an essential factor to characterize the affinity of chemical compounds with water. Thus, the water soluble fraction of the aerosol is an important parameter to consider the aerosol efficiency to serve as CCN (cloud condensation nuclei) (Zappoli et al., 1999). In general, we differentiate water soluble aerosol particles from the insoluble ones. Therefore, it is essential to identify soluble organic and inorganic compounds (WSOC: water soluble organic compounds and WSIC: water soluble inorganic compounds) and insoluble organic and inorganic compounds (WISOC:

water insoluble organic compounds and WISIC: water insoluble inorganic compounds). The most soluble particles are made, for example, of ammonium sulfate compounds or sodium chloride. Conversely, the most mineral dust, volcanic ash and anthropogenic soot particles are assigned as insoluble particles (Sullivan et al., 2009; Tang et al., 2016).

The aerosol lifetimes in the atmosphere range from minutes to days or weeks. Gravitational sedimentation, rain-out, and impaction are effective processes to remove aerosol from the atmosphere (Pöschl, 2005). During their lifetime in the atmosphere, the majority of aerosol particles do not remain in their initial state. After their emission/formation, they are transported by air masses around the globe and interact with other pollutants (Jeong et al., 2014). The lifetime of aerosol particles is strongly depending on their size, the larger particles usually having a shorter lifetime in the atmosphere. On the one hand, particles with diameter greater than a few microns quickly sediment under the effect of their own weight and are deposited on the ground. On the other hand, fine particles, which are the most numerous, can be suspended for a longer time in the atmosphere. Sedimentation plays a minor role on the smallest particles, their deposition being mostly due to Brownian diffusion. Due to atmospheric processes, aerosol microphysical and chemical properties undergo modifications in time. Indeed, mineral dust can uptake nitrates and sulfates that transform their shape from nonspherical mineral dust into more spherical particles and also change their hygroscopic properties (Zhang et al., 2000b; Matsuki et al., 2005; Tang et al., 2016). It has also been shown that sea salt particles, which are dominant aerosols in many oceanic regions of the world, can react with acidic pollutants, leading to changes in their hygroscopic properties (Chi et al., 2015). Particles can grow by condensation of condensable gases or coagulation with other particles (Delmas et al., 2005). Both phenomena contribute to a size growth of aerosol particles and to a change of their chemical composition (Ramabhadran et al., 1976). All these processes will, then, modify the atmospheric aerosol mixing state: (i) **external mixture** corresponds to two (or more) aerosol populations each containing one chemical compound; (ii) **internal mixture** corresponds to a homogeneous aerosol population containing several chemical compounds. The internal mixture corresponds usually to an aerosol, issued from a single source, whose physical and chemical properties have been modified over

time. In general, as a particle population is not totally represented by an external or an internal mixing state, it can be characterized by its degree of mixture (Winkler, 1973). Jacobson (2001) studied the evolution of aerosol chemical composition and showed that the state of mixing can strongly influence the radiative impact of aerosols. Lesins et al. (2002) have shown that an external mixture of aerosols will cool the atmosphere more efficiently in comparison to an internal mixture. Their study has highlighted that the single scattering albedo ( $\varpi_0$ ) is 25% lower for an internal mixture of aerosols compared to an external mixture.

## 1.3 Optical properties

The amount of energy reaching the Earth's surface, hence influencing the climate at a global scale, is affected by the interaction of sunlight with clouds and aerosol particles. The optical properties of aerosols describe their ability to interact with light and are directly related to the size and the chemical composition of particles. The mixing state and the surface properties of aerosols have also a strong influence on aerosol optical properties. Indeed, the thickness of the coating of the “core shell” structure has strong influence on the single scattering albedo (SSA (or  $\varpi_0$ )), Ramachandran and Srivastava (2013). Absorption gets enhanced in core-shell mixing of absorbing and scattering aerosols when compared to their external mixture. Moreover, this “core shell” structured aerosol has been found to represent better the observed aerosol SSA in comparison to pure external or internal mixing states (Pere et al., 2009).

### 1.3.1 Extinction, scattering and absorption coefficients

An aerosol population interacting with electromagnetic radiation (i.e solar or telluric radiation) leads to the deviation of the latter in multiple directions (Figure 1.4 shows one arbitrary direction). This phenomenon is called “scattering”. The scattering of light is a fundamental physical process that occurs at all wavelengths and is usually accompanied by

the absorption process. The dissipation of the electromagnetic radiation in the form of heat describes the absorption phenomenon (Bohren and Huffman, 2008).

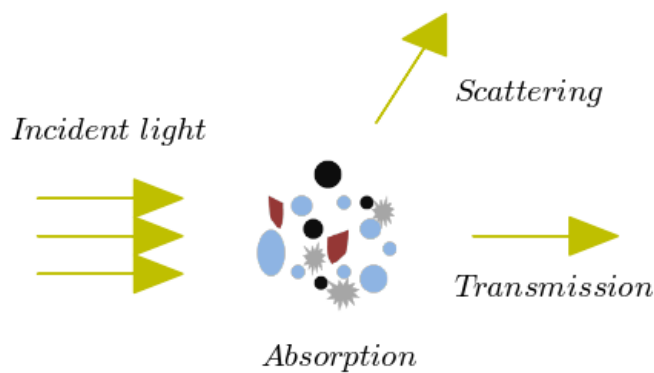


**Figure 1.4:** Mechanisms of interaction between incident electromagnetic radiation and aerosol population.

If we consider that the incident light (of intensity  $I$  ( $W.m^{-2}$ )) is propagating perpendicularly inside a homogenous medium (or aerosol population as shown in Figure 1.4) of a known thickness ( $dz$ ), the intensity of the incident light will suffer of some losses and will become  $I+dI$  with:

$$dI = -I\sigma_{ext}(z)dz \quad (1.5)$$

$\sigma_{ext}$ , is the extinction coefficient defined in the equation (1.6) for an aerosol population described by its size distribution  $n(r)dr$ . The extinction coefficient is obtained while multiplying the number of particles per unit volume by the extinction cross section.

$$\sigma_{ext} = \int_0^{\infty} \pi r^2 Q_{ext}(m, r, \lambda) n(r) dr \quad (1.6)$$

$Q_{ext}$  is defined as the extinction efficiency and obtained by dividing the extinction cross

section by the geometrical cross-section of the particle. If we consider that all the particles are spherical, the geometrical cross-section is equal to  $\pi r^2$ . As the light can be attenuated either by scattering or by absorption, for a wavelength ( $\lambda$ ) (equation (1.7)), the extinction coefficient can be decomposed into the scattering plus the absorption coefficient:

$$\sigma_{ext}(\lambda) = \sigma_{scat}(\lambda) + \sigma_{abs}(\lambda) = \int_0^{\infty} (Q_{scat}(m, r, \lambda) + Q_{abs}(m, r, \lambda)) \pi r^2 n(r) dr \quad (1.7)$$

By integrating equation (1.5) over a finite path between  $z_1$  and  $z_2$  we obtain Beer's law:

$$I(z_2) = I(z_1) e^{-\tau_e} \quad (1.8)$$

with:

$$\tau_e = \int_{z_1}^{z_2} \sigma_{ext}(z) dz \quad (1.9)$$

$\tau_e$  is defined as the extinction optical thickness over a finite thickness between  $z_1$  and  $z_2$ . Thus, when the extinction coefficient is high, visibility will be reduced and vice versa. Mie theory, published by Gustav Mie (1908) while solving Maxwell equations, gives a mathematical solution to the phenomenon of the scattering of a monochromatic plane wave by a homogeneous and spherical particle. It describes the scattering by a particle, with a size comparable to the wavelength of the incident light. Thus the scattering depends on Mie parameter, which is defined as the ratio between the size of the particle ( $2\pi r$ ;  $r$  is the radius of the particle) and the wavelength of the incident light  $\lambda$ :

$$x = \frac{2\pi r}{\lambda} \quad (1.10)$$

Depending on the value of  $x$ , three domains of scattering can be defined: Rayleigh scattering

occurs if  $x \ll 1$ , Mie scattering if  $x \approx 1$ , and the geometrical optics laws apply when  $x \gg 1$  (Bohren and Huffman, 2008).

### 1.3.2 Refractive index

The chemical composition of the aerosol is represented by its refractive index which is spectrally dependent, and composed of a real and an imaginary part:

$$m(\lambda) = n(\lambda) + ik(\lambda) \quad (1.11)$$

The refractive index is dimensionless and measures for a material or aerosol the reduction factor of the speed of light relative to its speed in vacuum. The scattering is mostly connected to the real part ( $n$ ) and the absorption mostly to the imaginary part ( $k$ ). The real part usually ranges from 1.333 for liquid water to 1.55 for mineral particles and reaches 1.95 (within the visible range) for soot particles (Bergstrom and Russell, 1999). The aerosol radiative impacts are strongly determined by the refractive index of the particle. Thus, if the real part varies from 1.40 to 1.45, Pilinis et al. (1995) estimate that the aerosol direct radiative forcing can be increased by 30%.

## 1.4 Hygroscopic properties

Aerosols present in the atmosphere have their properties (i.e. size, chemical composition, residence time) and impacts (as radiative effects) influenced by variable humidity conditions.

The hygroscopicity of a particle denotes its ability to adsorb liquid water on its surface. Thus, aerosols with high hygroscopic properties will take up more liquid water, which will have an impact on their size distributions, their chemical composition and on their optical and radiative properties (Randriamiarisoa et al., 2006). The amount of water condensed on the surface of an aerosol particle is defined by its chemical composition (Raoult effect) and

its size (Kelvin effect) and is directly related to the water activity:

$$a_w = \frac{p_w}{p_w^0} \quad (1.12)$$

where  $p_w$  is the water vapor pressure and  $p_w^0$  is the water vapor saturation pressure at the same temperature. When the pure liquid water is in equilibrium with its vapor phase, then  $p_w = p_w^0$  and the activity of the water  $a_w$  is equal to 1. If the surrounding air is in equilibrium with the water surface, we can connect the  $a_w$  to the relative humidity, RH, which quantifies the sub-saturation of the water vapor. The relation between  $a_w$  and RH is therefore written as:

$$RH = a_w \times 100 \quad (1.13)$$

### 1.4.1 Hygroscopic conditions and phase transitions

Aerosols can serve as a support of the condensation of atmospheric water vapor. In the atmosphere, the humidity conditions are highly variable as a function of locations, period of the day and season. Therefore, there are different regimes of interaction between water vapor and aerosol.

- **Super-saturation:** When  $p_w > p_w^0$ , i.e.  $a_w > 1$  and  $RH > 100\%$ , within this range of RH, aerosol can activate into a droplet. Köhler's first work (1936) highlights the link between the size of a water droplet and the relative humidity (RH).
- **Saturation:** When  $p_w = p_w^0$ , i.e.  $a_w = 1$  and  $RH = 100\%$ , the water is in liquid form. The air contains the maximum amount of water vapor, corresponding to  $p_w^0$ .
- **Sub-saturation:** When  $p_w < p_w^0$ , i.e.  $a_w < 1$  and  $RH < 100\%$ , the water is in vapor form. Within this range of RH, the size of the aerosol can double (Tang, 1996b).

In this thesis we focus our work on the sub-saturation conditions.

### 1.4.1.1 Köhler's theory

Aerosols can serve as a support of the condensation of atmospheric liquid water. Hence, the activation of an aerosol particle as CCN is described by Köhler's theory. The link between the size of a water droplet and the relative humidity (RH) is now well proven from the Köhler equation:

$$RH = a_{w,s} \exp\left[\frac{2M_w\sigma}{RT r \rho}\right] \quad (1.14)$$

with  $a_{w,s}$  being the activity of the water in the solution,  $M_w$  the molar mass of the water,  $\sigma$  the surface tension of the solution,  $R$  the constant of the perfect gases,  $T$  the temperature,  $r$  the droplet radius at equilibrium and  $\rho$  the density of the droplet of aqueous solution.

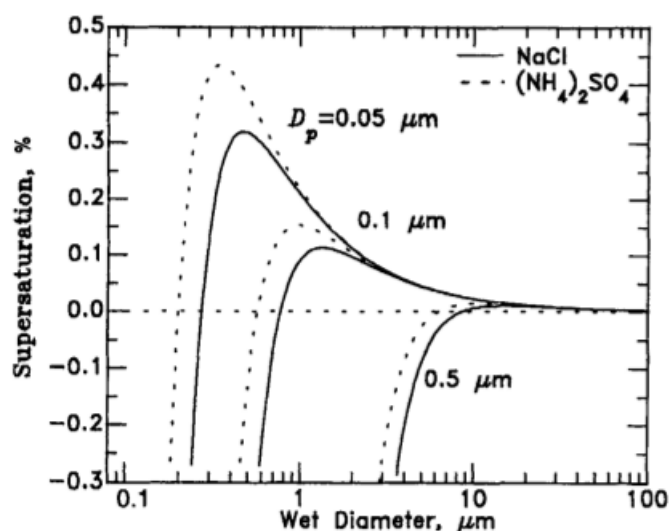


**Figure 1.5:** Köhler curve for NaCl (solid lines) and  $(\text{NH}_4)_2\text{SO}_4$  (dashed lines) with dry diameters of 0.05, 0.1, et 0.5  $\mu\text{m}$  at 293 K. Source: [Seinfeld and Pandis \(1998\)](#).

The term  $\exp\left[\frac{2M_w\sigma}{RT r \rho}\right]$  is related to the Kelvin curve. It considers the effect of curvature of the aerosol on the studied equilibrium and shows that the relative humidity required to

activate an aerosol in droplet, increases when the size of this aerosol decreases. On the other hand, the term  $a_{w,s}$  is related to the Raoult curve and shows that the presence of a hydrophilic solute in the water reduces the relative humidity required for activation of the aerosol in droplet. The rassemblement of these two physical (Kelvin effect) and chemical (Raoult effect) contributions gives the Köhler curve represented in Figure 1.5, showing the relation between the supersaturation and aerosol size.

#### 1.4.1.2 Sub-saturation (RH<100%)

Two phenomena are associated with the interaction between water vapor and crystals: deliquescence and efflorescence (i.e. point of recrystallization, Richardson and Spann (1984)). The **deliquescence** is a first-order phase transformation that occurs when the deliquescent substance is in contact with water vapor and forms an aqueous solution. This transformation occurs at a well-defined relative humidity that depends on the initial properties of the solid compound and the environmental conditions, i.e. the temperature (Wexler and Seinfeld, 1991). Starting from an aerosol exposed to low RH (RH=30%), the particle remains solid and its scattering coefficient as well as its diameter remain constant until a specific RH value is reached (Figure 1.6). An increase of the relative humidity, beyond this specific RH, leads to spontaneously water adsorption (at 80%, for example given in Figure 1.6). The aqueous solution becomes the thermodynamically favorable phase and the deliquescence begins. This characteristic RH is referred to as the deliquescence relative humidity (DRH).

The **efflorescence** is a first-order transition that occurs when the solution is starting to form a crystal, which characterizes the inverse process of deliquescence (i.e. deshydration process associated with RH decrease). At its critical relative humidity that refers to efflorescence relative humidity, the solution becomes so concentrated that a spontaneous nucleation of the solid phase occurs. A hysteresis phenomenon between deliquescence and efflorescence is shown since the efflorescence process generally occurs at a lower RH than the DRH. The hysteresis phenomenon, illustrated in Figure 1.7, describes the behavior of particle diameter or scattering as a function of the relative humidity. Thus, aerosol particles

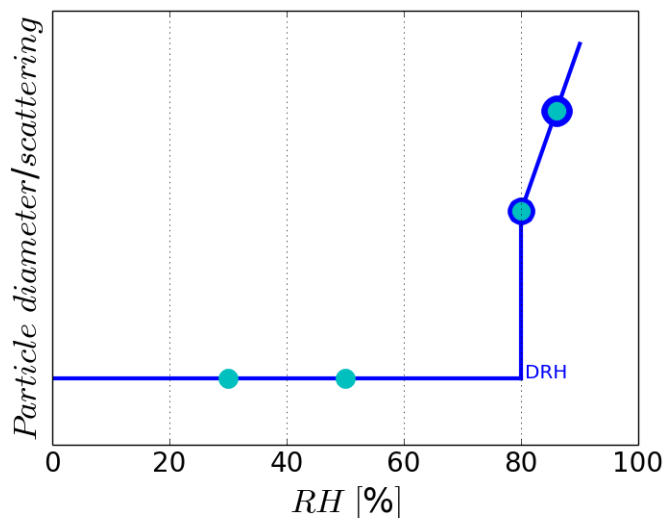


**Figure 1.6:** Schematic of particle diameter or scattering evolution as a function of RH.

The deliquescence branch show the phenomenon that occurs by humidifying particles.

can exist in solid and liquid phase at the same RH. Table 1.2 gives the DRH and ERH of some pure components (solution made of one electrolyte) and binary mixtures measured or calculated using different approaches (single levitated particle, visibility model...). Some aerosols, such as  $NH_4HSO_4$  and  $NaHSO_4$ , deliquesce at low RH (40 and 52%) while others, such as  $Na_2SO_4$  and  $KCl$ , will interact with water at high humidities (84.2%). Once these particles are hydrated, the ambient relative humidity needs to decrease drastically (down to 35% for  $(NH_4)_2SO_4$  to remove all the water uptaken. The ERH for  $NaNO_3$ ,  $NH_4HSO_4$ , and  $NH_4NO_3$  is so low that it has not been observed within the laboratory meaning that these hydrated aerosols never dry up within the atmosphere.

Different studies have been performed in order to characterize the behavior of atmospheric aerosol properties as a function of RH. Covert et al. (1972) have shown that pure aerosols are deliquescent and others show a continuous increase of light scattering with RH. However, atmospheric aerosols are mainly composed of internal mixtures (Winkler, 1973). Jing et al.

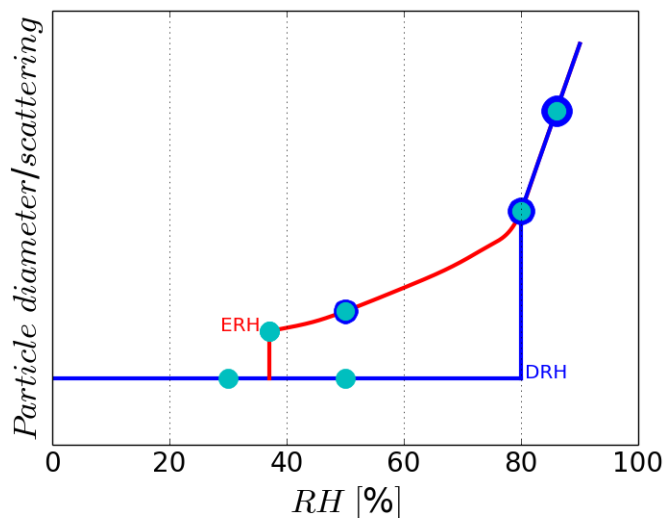


**Figure 1.7:** Schematic of particle diameter or scattering evolution as a function of RH. The deliquescence (blue curve) and efflorescence (red curve) branches show the hysteresis phenomenon that occurs by humidifying and drying particles.

**Table 1.2:** Deliquescence and efflorescence relative humidities of electrolyte solutions at 298 K. Sources: [Tang \(1996b\)](#); [Tang and Munkelwitz \(1993, 1994a\)](#); [Martin \(2000\)](#)

Salt	DRH(%)	ERH(%)
<i>KCl</i>	84.2±0.3	59
<i>Na<sub>2</sub>SO<sub>4</sub></i>	84.2±0.4	56±1
<i>NH<sub>4</sub>Cl</i>	80.0	45
<i>(NH<sub>4</sub>)<sub>2</sub>SO<sub>4</sub></i>	79.9±0.5	35±2
<i>NaCl</i>	75.3±0.1	43±3
<i>NaNO<sub>3</sub></i>	74.3±0.4	Not observed
<i>(NH<sub>4</sub>)<sub>3</sub>H(SO<sub>4</sub>)<sub>2</sub></i>	69.04	-
<i>NH<sub>4</sub>NO<sub>3</sub></i>	61.8	Not observed
<i>NaHSO<sub>4</sub></i>	52.0	-
<i>NH<sub>4</sub>HSO<sub>4</sub></i>	40.0	Not observed
<i>NaCl – KCl</i>	72.7	-
<i>NaCl – NaNO<sub>3</sub></i>	68	-

(2018) conclude, after working on aerosols containing nitrate salts mixed with water-soluble organic acid, that a better understanding of the interactions between water and aerosols that contain several compounds is needed.

The deliquescence behavior of salt mixtures is different than that of single salt and does not correspond to the sum of the DRH of each salt (i.e.  $NaCl/KCl$  and  $NaCl/NaNO_3$  in table 1.2). The deliquescence curve for a mixture does not have a single transition but several, and is characterized by several DRH values associated with the molar fraction of the component in the mixture (Tang et al., 1978). For a binary electrolytes mixture, two values of DRH are observable. The particle phase remains solid during the humidifying process until a first change of state called MDRH (Mutual Deliquescence Relative Humidity). After this point, water is adsorbed by the particle and two phases coexist: a solid phase and a liquid phase. The particle, existing in two phases, continues to adsorb water until it becomes liquid. This second transition is characterized by a value of DRH. This phenomenon occurs for all the molar fractions of a mixture at different MDRH and DRH values. However, at the eutonic point, the solid has only one transition at the value of the MDRH. This point is indicated by DRH\* in Figure 1.8.

Equations of Gibbs-Duhem proved the fact that the DRH of an electrolyte is lowered when a second electrolyte is added (Wexler and Seinfeld, 1991). Using this equations and by applying Harnerd's rule (Harned and Owen, 1958), Wexler and Seinfeld (1991) plot the water activity ( $a_w$ ) as a function of the molar fraction of  $NH_4NO_3$  in  $NH_4Cl/NH_4NO_3$  mixture. Figure 1.8 represents the obtained diagram. While the MDRH (51%) depends only on the nature of the salts, the 2<sup>nd</sup> DRH (black line) varies as a function of the molar fraction of the mixture (black curve, Figure 1.8). The phase transition at the eutonic point is represented in this diagram as DRH\*. Similar deliquescence diagrams can be calculated and plotted using E-AIM model, described in section 1.4.3 Clegg et al. (1998). Seven different regimes exist in Figure 1.8, four main separate areas are described below:

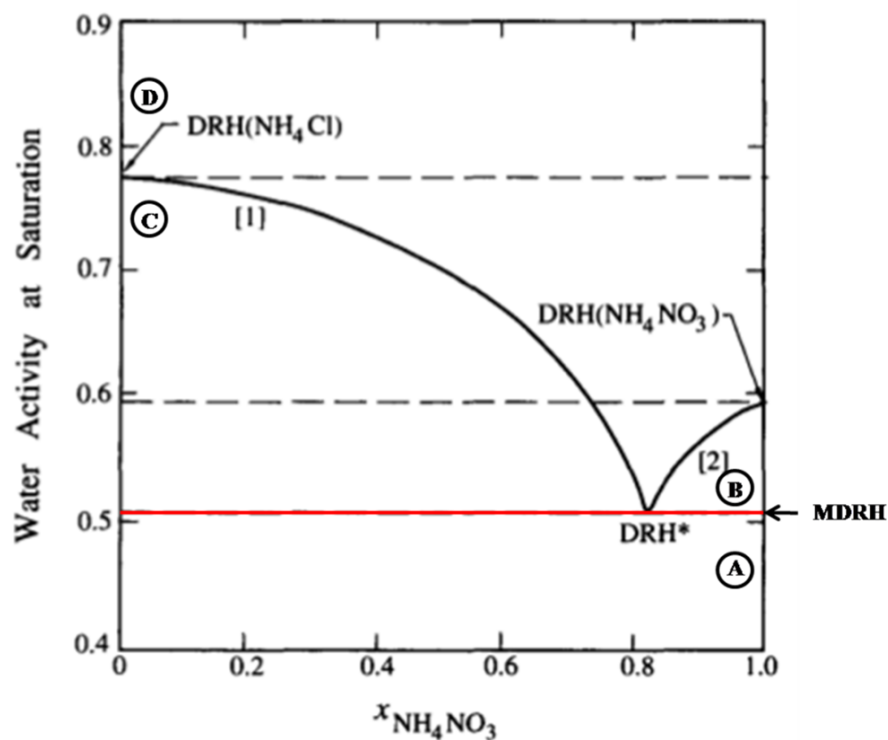


**Figure 1.8:** Deliquescence diagram of  $\text{NH}_4\text{NO}_3/\text{NH}_4\text{Cl}$  mixture. A, B, C and D correspond to the four main regimes (see text for more details). The water activity at saturation is represented as a function of  $\text{NH}_4\text{NO}_3$  fraction in the mixing. Red lines (black) correspond to the MDRH (DRH). Source: [Seinfeld and Pandis \(2006\)](#) with some extra notions.

- A-**  $\text{NH}_4\text{NO}_3$  and  $\text{NH}_4\text{Cl}$  both are mixed in the solid state for a RH below the MDRH and for all the molar fractions.
- B-** Solid  $\text{NH}_4\text{NO}_3$  is in equilibrium with an aqueous phase in the eutonic composition, between the MDRH and the 2<sup>nd</sup> DRH, for  $X_{\text{NH}_4\text{NO}_3}$  greater than 0.811.
- C-** Solid  $\text{NH}_4\text{Cl}$  is in equilibrium with an aqueous phase in the eutonic composition, between the MDRH and the 2<sup>nd</sup> DRH, for  $X_{\text{NH}_4\text{NO}_3}$  less than 0.811.
- D-**  $\text{NH}_4\text{NO}_3$  and  $\text{NH}_4\text{Cl}$  both are mixed in aqueous form for a higher RH than the 2<sup>nd</sup> DRH and for all the molar fractions.

More complex diagrams of phase transitions can be obtained for aerosol mixture composed of more than three salts (Potukuchi and Wexler, 1995). Spann and Richardson (1985) have shown that for some aerosol mixtures of inorganic salts, crystallization of particles is not possible under atmospheric conditions, even at very low RH.

## 1.4.2 Hygroscopic factors

### 1.4.2.1 Growth Factor $g(\text{RH})$

As previously stated, aerosol particles may adsorb water vapor and their sizes generally (be aware of some cases of exception, see later with soot) increase from dry diameters  $D_p(\text{dry})$  to wet diameters  $D_p(\text{RH})$  as shown in Figure 1.9. This phenomenon is called hygroscopic growth and is described by the hygroscopic growth factor  $g(\text{RH})$  or  $GF(\text{RH})$  (Growth Factor) defined by the following equation:

$$g(\text{RH}) = \frac{D_p(\text{RH})}{D_p(\text{dry})} \quad (1.15)$$

This parameter is easily determined experimentally by observing the evolution of particle size when the relative humidity varies. It is calculated by dividing the measured wet diameter by the respective dry diameter and may be obtained directly from **optical image analysis** (Figure 1.9, Seng et al. (2018a)) or indirectly using two systems that measure the entire particle size distributions (**H**umidified **T**andem **D**ifferential **M**obility **A**nalyzer: **HTDMA**, Zieger et al. (2017)) as a function of the relative humidity.

Table 1.3 presents the  $g(\text{RH})$ , measured or calculated, for several main aerosol species or types. The growth factors vary significantly according to the aerosol chemical composition and type. Indeed,  $g(\text{RH})$  can reach high values (i.e.  $>2$ ) for highly hygroscopic aerosols (for example  $g(\text{RH})[\text{NaCl}(90\%)]=2.34$ ) (Gupta et al., 2015). Conversely, other aerosol types, as for example mineral dust, remain indifferent to humidification ( $g(\text{RH})$  of mineral dust

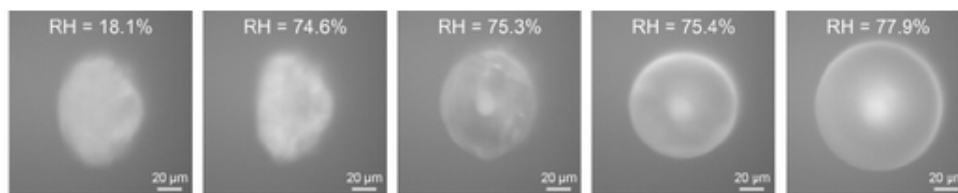


**Figure 1.9:** *Optical images of a single levitated  $\text{NaNO}_3$  particle undergoing humidifying process (Seng et al., 2018a).*

**Table 1.3:** *Growth factors measured using a HTDMA or calculated using thermodynamic models for some main aerosol species or types of 100 nm diameter.*

GF at 90% relative humidity		
Compound	GF	References
$(\text{NH}_4)_2\text{SO}_4$	1.68	Topping et al. (2004) Petters and Kreidenweis (2007) Clegg et al. (1998) Hämeri et al. (2001)
$\text{NH}_4\text{NO}_3$	1.77	
$\text{NaCl}$	2.34	
$\text{H}_2\text{SO}_4$	2.27	
$\text{NaNO}_3$	2.02	
$\text{NaHSO}_4$	2.16	
$\text{Na}_2\text{SO}_4$	1.92	
$(\text{NH}_4)_3\text{H}(\text{SO}_4)$	1.7	
Mineral Dust	<1.05	Vlasenko et al. (2005)

<1.05). Thus, the size of these hydrophobic particles will not change with the relative humidity. It is also possible to observe growth factors <1 for the most hydrophobic soot particles, i.e. shrinking of particle. Indeed, under the effect of humidification, the molecule that composes the aerosol will collapse on itself to form a more spherical particle; hence its initial diameter decreases ( $\text{GF} \approx 0.9-0.95$ ) (Weingartner et al., 1997).

#### 1.4.2.2 Scattering enhancement factor $f(\text{RH})$

In addition to the particle size increase, when RH increases, the aerosol optical properties may be altered. The scattering enhancement factor is defined by the ratio between the scattering coefficient at ambient relative humidity and the scattering coefficient at dry conditions

(typically RH less than 40%) (Kotchenruther and Hobbs, 1998; Fierz-Schmidhauser et al., 2010a; Ziemba et al., 2013). This factor is defined as follows:

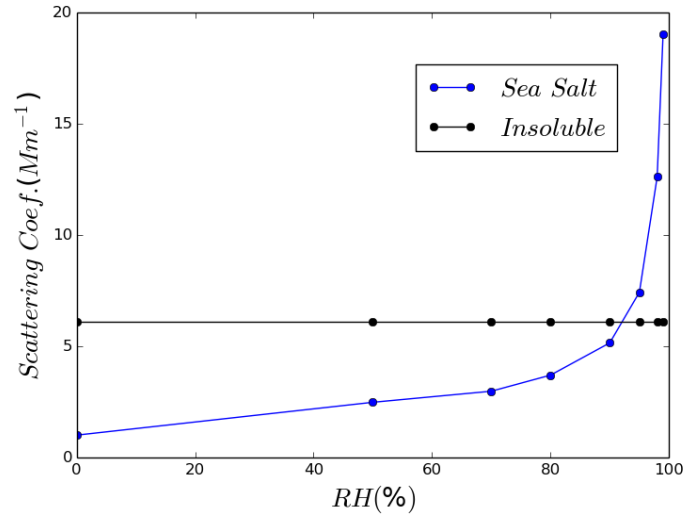
$$f(RH, \lambda) = \frac{\sigma_{scat}(RH, \lambda)}{\sigma_{scat}(dry, \lambda)} \quad (1.16)$$

Figure 1.10 illustrates the variation of the scattering coefficient for an insoluble aerosol (hydrophobic) and a sea salt aerosol (hygroscopic) (Hess et al., 1998). As previously observed for the  $g(RH)$ , an insoluble aerosol (i.e soot generated by combustion) subjected to different RH undergoes no change in its chemical composition and size, and therefore its optical properties and in particular its scattering coefficient will be constant during the humidifying process. In contrast, the scattering coefficient of an aerosol derived from sea salts, increases with increasing RH. Most of the sub-saturation hygroscopicity measurements (RH <100%) are performed at 90% RH. Higher humidity could lead to instrumental problems during measurements.

As many authors, Chen et al. (2014) have shown the sudden increase of  $f(RH)$  with increasing RH, based on their nephelometer measurements obtained in a field-campaign in China. Thus at higher RH, the water uptake has a large influence on the aerosol optical properties and thus on the aerosol direct radiative forcing (Schwartz, 1996). Different studies have investigated the variation of the  $f(RH)$  with relative humidity, this variation being expressed as an exponential function (Carrico et al., 1998; Malm and Day, 2001). They also show a continuous uptake of water by aerosol particles at relatively low RH (20-30% RH).

### 1.4.2.3 Link between Hygroscopic factors

Generally, growth factor and scattering enhancement factor are not measured simultaneously. Thus, in order to allow comparison of one method to the other, one need to find a relation linking optical enhancement to growth factor as a function of humidity. Starting from the scattering enhancement factor described above:



**Figure 1.10:** Variation of the scattering coefficient at  $\lambda=525\text{nm}$  as a function of the relative humidity for sea salt aerosols (blue curve) and insoluble aerosols (black curve) using the software package OPAC (Optical Properties of Aerosols and Clouds).

$$f(RH, \lambda) = \frac{\sigma_{scat}(RH, \lambda)}{\sigma_{scat}(dry, \lambda)} = \frac{\int \frac{\pi}{4} Q_s(RH) D_p(RH)^2 N(D_p) dD_p}{\int \frac{\pi}{4} Q_s(dry) D_p(dry)^2 N(D_p) dD_p} \quad (1.17)$$

Where  $Q_s(RH)$  and  $Q_s(dry)$  represent the scattering efficiencies at ambient and dry conditions,  $N(D_p)$  is the number size distribution. If  $N_t$  represents the total number concentration, equation 1.17 becomes:

$$f(RH) = \frac{\sigma_{scat}(RH, \lambda)}{\sigma_{scat}(dry, \lambda)} = \frac{\overline{\frac{\pi}{4} Q_s(RH) D_p(RH)^2} N_t}{\overline{\frac{\pi}{4} Q_s(dry) D_p(dry)^2} N_t} = \frac{\overline{Q_s(RH) D_p(RH)^2}}{\overline{Q_s(dry) D_p(dry)^2}} \quad (1.18)$$

Thus:

$$\overline{D_p(RH)} = \overline{D_p(dry)} \sqrt{f(RH) \frac{\overline{Q_s(dry)}}{\overline{Q_s(RH)}}} \quad (1.19)$$

Now by assuming that the scattering efficiencies at ambient and dry conditions are equal.

$$\frac{\overline{Q_s(RH)}}{\overline{Q_s(dry)}} \approx 1 \quad (1.20)$$

The relationship between the scattering enhancement factor and the growth factor of aerosol particles is obtained by combining equations 1.19 and 1.20 (Guo et al., 2015; Bougiatioti et al., 2016). (See Annex 4)

$$g(RH) = \sqrt{f(RH)} \quad (1.21)$$

### 1.4.3 Aerosols thermodynamic models

As measurements for all aerosol mixtures are not available, simulations of aerosol hygroscopic properties are deemed essential for a more comprehensive understanding of aerosol properties evolution as a function of RH and particularly for modelers. Indeed, modification of aerosol hygroscopic properties, for example due to aging during transport, may affect CCN concentrations as well as their wet deposition rate and therefore modify their impact on health and on climate. In this thesis, laboratory measurements of hygroscopic properties of inorganic mixtures of aerosols are compared to thermodynamic model (E-AIM) results and to Zdanovskii–Stokes–Robinson (ZSR) calculations in order to validate these methods and/or estimate their biases.

The **Extended-Aerosol Inorganics Model (E-AIM)**, an additional development of AIM (Wexler and Seinfeld, 1991), is an online available thermodynamic model. E-AIM is a community model for calculating gaz/liquid/solid partitioning in aerosol systems containing different components (inorganic, organic) and water. Partitioning of aerosols  $<0.1 \mu\text{m}$  influenced by the Kelvin effect is not included in this model. The chemical model (Model III) used in this work is the  $H^+ - NH_4^+ - Na^+ - SO_4^{2-} - NO_3^- - Cl^- - H_2O$  system, taken at a temperature of 298.15 K. The number of moles of the specific inorganic species composing

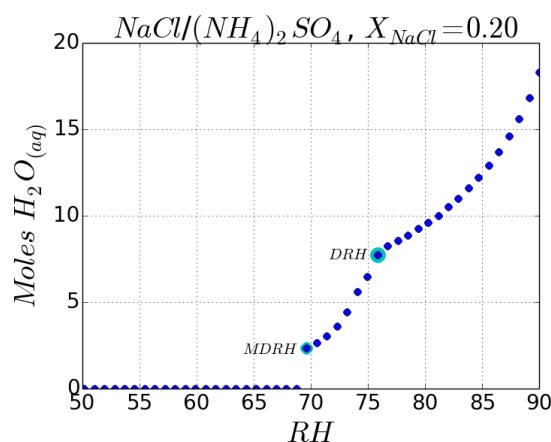


**Figure 1.11:** Variation of number of moles of  $H_2O$  with the relative humidity for  $NaCl/(NH_4)_2SO_4$  mixture containing 20% of  $NaCl$  calculated using E-AIM. The MDRH and the DRH are represented by the light blue dots.

the system are used as input data. In the model, the formation of gas phase species and the formation of new solids can either be allowed or not during RH variation. In this thesis we used both options. The user specifies the range of the relative humidity or the total water content of the system. The mole fraction of aqueous  $H_2O$  is then the output data. The model contains all known solid phases of the system presented, in addition to the double salts, and does not contain simplifying assumption. The E04UCF (Numerical Algorithms Group) is used in E-AIM to achieve the calculations (Wexler and Clegg, 2002). The DRH is defined for each salt and compared to the experimental results by plotting the number of moles of  $H_2O$  as a function of RH calculated using E-AIM. Figure 1.11 shows an example of these plots, with determination of MDRH and DRH using E-AIM output data.

This figure illustrates the variation of the number of moles of  $H_2O$  as a function of RH, for  $X_{NaCl}=0.2$  in the  $NaCl/(NH_4)_2SO_4$  mixture. Both phase transitions are represented: MDRH (70%) and the DRH (76%).

Gupta et al. (2015) have shown good agreement between experimental measurements of MDRH and DRH values using SEM/EDX (Scanning Electron Microscope/Energy Dis-

persive X-ray) elemental mapping in comparison to E-AIM model predicted values for  $NaCl/NaNO_3$  mixture. Moreover, the growth factors of ammonium sulfate and ammonium nitrate particles, measured by a HTDMA, match well with E-AIM calculations over the entire RH range (Liu et al., 2016). Based on these results, we choose to use E-AIM model that calculate the molar fraction of  $H_2O$  uptaken by the particle during the humidifying process, in order to deduce the DRH for pure aerosol and the MDRH/DRH values for aerosol mixtures, to finally compare the results with experimental data.

In addition to E-AIM model, different thermodynamic models are used to calculate the aerosol liquid water content (ALWC) condensed on the aerosol surface. One of the most used is ISORROPIA-II (Fountoukis and Nenes, 2007) in which temperature, RH, and total aerosol concentration ( $NH_3$ ,  $H_2SO_4$ ,  $HCl$ ,...) serve as input data (see details in Annex 4). The aerosol liquid water content (ALWC) is then calculated. In this work, we used ISORROPIA-II only to verify the deliquescence values (DRH) of pure aerosols.

#### 1.4.4 Application of ZSR relation (Zdanovskii-Stokes-Robinson) to multicomponent aerosols

The ZSR (Zdanovskii-Stokes-Robinson) relationship (Zdanovskii, 1948; Stokes and Robinson, 1966) is a simplification of the hygroscopic growth factor calculation of a multicomponent aerosol, usually used in atmospheric aerosol models (Hanel and Zankl, 1979; Cohen et al., 1987; Pilinis and Seinfeld, 1987; Wexler and Seinfeld, 1991). Cohen et al. (1987), using a levitated single particle in an electrodynamic balance to compare experimental results with three different thermodynamical models (Pitzer's virial coefficient model, Chen's local composition model and BET-based model of Robinson and Stokes), have shown that the models are in agreement but inconsistent with the experimental data. The ZSR theory assumes that there is no interaction that occurs between the various compounds of the solution, and consists in calculating the hygroscopicity of the multicomponent aerosol by summing the growth factors of each compound, weighted by their mass or molar fractions according to the following formula:

$$g(RH)_{global} = \sqrt[3]{\varepsilon_a g(RH)_a^3 + \varepsilon_b g(RH)_b^3} \quad (1.22)$$

Where  $\varepsilon_a$  and  $\varepsilon_b$  are the mass (or molar) fractions of the various compounds, and  $g(RH)_a$  and  $g(RH)_b$  are the respective growth factors of compounds a and b. In the next chapters we use  $X_a$  to define the molar fraction of the compound (a). [Tong et al. \(2008\)](#) have compared different models that calculate the activity coefficient for atmospheric aerosols containing mixtures of salts, organic compounds and water. According to them, since the chemical composition and the physical properties of the organic fraction are poorly known, the ZSR which is a simplified approach is easier than complicated models like the model X-UNIFAC.3 ([Erdakos et al., 2006](#)). In most cases, when describing the growth factors of organic-organic and organic-inorganic mixtures, this theory works quite well and can be used as a good estimate of the growth factor of a multicomponent aerosol according to [Chan and Chan \(2003\)](#) and [Zardini et al. \(2008\)](#).

However, several studies ([Ma et al., 2013](#); [Jing et al., 2018](#)) have highlighted deviations of the  $g(RH)$  calculated with ZSR theory in comparison to observed  $g(RH)$  for some specific organic-inorganic mixtures (for example nitrate salts and water-soluble organic acids). [Moore and Raymond \(2008\)](#) have compared the ZSR theory results to measurements of the  $g(RH)$  for salt-containing synthetic aerosols and organic mixtures of dicarboxylic acids, in order to model the incomplete dissolution of some species. According to their results, the different chemical species (organics vs inorganics) do not necessarily contribute in the same way to the aerosol mixture hygroscopic properties. Recent studies have shown that some organic compounds decrease or increase (depending on organic mass fraction) the hygroscopicity of inorganic salts ([Cruz and Pandis, 2000](#); [Prenni et al., 2003](#)). No general theory could be drawn for all aerosol mixtures existing within the atmosphere due to the multitude of organic compounds.

Another difficulty arises from the surface properties of the aerosol. The coating on aerosol surface does not completely mask the hygroscopic behavior of aerosol nucleus. Using volatil-

ity measurements, [Michaud \(2009\)](#) has explained the impact on the  $g(\text{RH})$  of paraffin coating on  $\text{NaCl}$  particles. One would expect that the paraffin coating would avoid any water uptake on the aerosol surface. However, The  $g(90\%)$  of the coated particles is about  $1.85 \pm 0.02$  for a 130 nm particle while the pure  $\text{NaCl}$   $g(90\%)$  is 2.35 for a 100 nm particle. Despite this effect, this study has shown a good agreement between the  $g(\text{RH})$  calculated from the ZSR theory and the  $g(\text{RH})$  provided by HTDMA for this organic/inorganic mixture.

[Svenningsson et al. \(2006\)](#) have performed a study on the hygroscopicity of different aerosol mixtures at different relative humidities. These mixtures were supposed to be representative of certain categories of air masses. In fact, by using data on the chemical composition of different types of aerosols, they have prepared several mixtures of various types of air masses: the mixture “MIXBIO” that represents an aerosol emitted in regions dominated by biomass burning, “MIXSEA” representing a marine aerosol and “MIXPO” that represents a continental and polluted aerosol. The application of the ZSR theory on these different mixtures gave good results, except for the “MIXSEA” mixture, whose hygroscopicity was overestimated by the ZSR theory. Consistently, [Cohen et al. \(1987\)](#) have also found a deviation between the ZSR theory and measurements for  $(\text{NH}_4)_2\text{SO}_4/\text{NaCl}$  mixture. They explained the differences by several hypotheses, such as the density and crystalline form factor of sodium chloride, as well as the evaporation of certain compounds. According to our knowledge and up to date, [Cohen et al. \(1987\)](#) and [Svenningsson et al. \(2006\)](#) are the only studies comparing ZSR  $g(\text{RH})$  calculations to experimental results for inorganic/inorganic mixtures. Therefore, more work need to be achieved on inorganic-inorganic mixtures to validate and/or test the applicability of the ZSR theory in order to better understand the reasons behind the observed deviations.

## 1.5 Conclusion

Aerosol particles are emitted via different processes (primary or secondary aerosol) and quickly after these emissions their physical, chemical and optical properties evolve due to presence of other particles and condensable material within the atmosphere. In particular,

water vapor which is adsorbed by aerosol particles, drastically changes their properties, even within the sub-saturation regime. As these properties are key parameters to estimate the aerosol impacts on climate change as well as on population health, a better knowledge of the modification of aerosol properties due to water uptake is needed.

Different parameters have been defined to better characterize the evolution of the aerosol physical ( $g(RH)$ ) and optical ( $f(RH)$ ) properties as a function of RH. Few instrumental techniques allow the scientific community to measure these parameters such as HTDMA, optical microscopy, and nephelometry. Numerical methods also exist to predict the evolution of the aerosol physical properties such as E-AIM for a single particle and the Zdanovskii-Stokes-Robinson (ZSR) for an aerosol population. E-AIM results have been validated for different types of aerosol, whereas the ZSR has been validated only for organic mixtures. Indeed, some unexplained discrepancies still exist for organic-inorganic and inorganic-inorganic mixtures between calculated and observed  $g(RH)$ . Therefore, in this thesis we will focus on better understanding of the reasons behind these discrepancies by measuring and calculating the hygroscopic factors and the DRH for inorganic-inorganic mixtures made of sodium chloride ( $NaCl$ ), ammonium sulfate ( $(NH_4)_2SO_4$ ), potassium chloride ( $KCl$ ) and sodium nitrate ( $NaNO_3$ ), and their mixtures.



---

---

## CHAPTER 2

---

# Methodology and instrumentation

The analysis of the evolution of synthetic aerosol hygroscopic properties relies on most sophisticated in-situ and laboratory instruments presented herein. As previously stated in chapter 1, aerosol particle impacts on health and climate are highly dependent on the aerosol physical, chemical and optical properties. Moreover, it has been proven that these properties evolve constantly within the atmosphere due to several processes (coagulation, condensation, heterogeneous reactions, etc...). As a result of these modifications, the water uptake and including their interaction with water within the sub-saturation regime. Indeed, the particle diameter can double (Tang, 1996b), the mixing state, i.e. whether components are homogeneously mixed or phase separated the aerosol within the mixture, can evolve (Laskina et al., 2015), and the aerosol optical properties will therefore be modified. The hygroscopic factors ( $g(\text{RH})$  and  $f(\text{RH})$ ), described in chapter 1, are defined as the ratio of the wet vs dry physical and optical parameters (diameter and scattering coefficient). These parameters could be measured using different instruments working in a wide range of RH (<100%) to study the aerosol property evolution with RH. In the literature, various instruments have been used to quantify modifications of aerosol properties during the humidifying process. The most common are (i) humidified nephelometer in order to measure the variation of the scattering coefficient ( $f(\text{RH})$ : ratio of wet and dry scattering coefficients) due to relative humidity (Fierz-Schmidhauser et al., 2010a; Zieger et al., 2011; Titos et al., 2014, 2016) and (ii) HTDMA (Hygroscopicity Tandem Differential Mobility Analyzer) to study the hygroscopic growth factor  $g(\text{RH})$  (ratio of wet and dry particle diameters) (Prenni et al., 2003; Meyer et al., 2009; Zieger et al., 2017). Both methods alone or coupled (Denjean et al., 2014) suffer from the lack of information on the chemical composition evolution during the humidifying process. Indeed, while mixing different aerosol components, the probability of the appearance of new species in the mixture is not negligible. As an example, either for laboratory generated aerosol studies (pure and mixed SOA: Michaud et al. (2009) or real atmospheric aerosols (continental-rural aerosols: Gysel et al. (2004)), the studies assume that the aerosol composition is similar to the original aerosol composition, throughout the humidifying process. On the other hand, other studies are only studying the aerosol chemical composition evolution with the relative humidity. Lee et al. (2008) have characterized the

partial deliquescence of  $(NH_4)_2SO_4/NH_4NO_3$  by analyzing Raman peaks. Moreover, the Raman observations provide information about the phase transition of each compound of the mixture (Ling and Chan, 2008) that may modify the aerosol hygroscopic properties. Finally, some studies were devoted to the characterisation of the phase transition and aerosol growth properties using an optical microscopy and Raman spectroscopy (Yeung et al., 2009).

To our best knowledge, no study has analyzed the evolution of aerosol chemical, physical and optical properties considering the same aerosol species. In this thesis, we aim to perform aerosol hygroscopicity measurements for aerosols generated in the laboratory considering both a single particle and the aerosol population. The first experimental setup includes an optical particle counter (OPC) and a nephelometer, described in section 2.1, and was mounted during this thesis. Whereas, the second experimental setup (section 2.2) pairs a Raman microspectrometer with a levitation cell equipped with a high-speed high-resolution video camera, already existed at LASIR laboratory. The approach developed in this thesis, based on these two experimental setups, has been possible through a close collaboration between LOA and LASIR in the frame of the Labex CaPPA. The various devices that have been used during the experiments presented in this thesis will be presented herein. These experimentations allow the observation of aerosol properties during the increase of RH thereby using different techniques. In particular, the evolution of optical, physical, and chemical properties will be studied.

## 2.1 Experiment 1: Size and optical properties of aerosol population

Only few studies used HTDMA coupled with a nephelometer to measure the variation of aerosol size simultaneously with scattering coefficient as a function of the relative humidity (Denjean et al., 2014). The experimental setup (Figure 2.1) used in this study also provide simultaneously measurement of the scattering enhancement factor ( $f(RH)$ ) as well as the growth factor ( $g(RH)$ ).

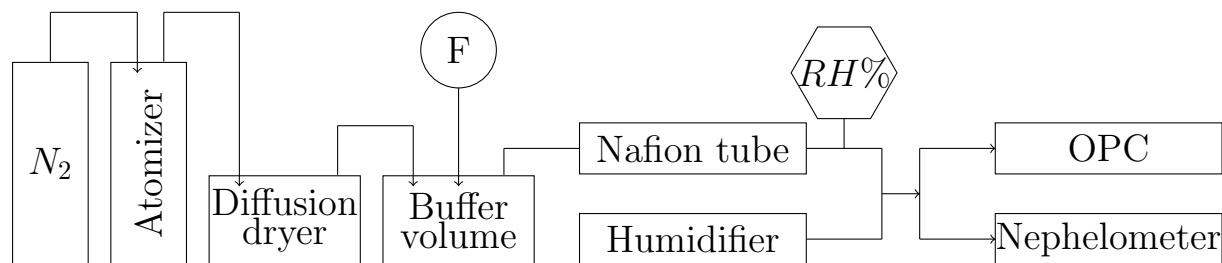


**Figure 2.1:** *Experimental setup used to measure aerosol optical and physical properties at variable relative humidity.*

Where:

- F is defined as the HEPA filter.
- $RH\%$  is the relative humidity sensor.

The experiments are carried out at room temperature ( $T \approx 298$  K) and at atmospheric pressure ( $P \approx 1.013$  hPa). The key variables in the experiments were aerosol composition and relative humidity.

**Generation system:** The aerosol generation system consists of a TSI particle generator. The operational principle of the atomizer is based on the mechanical dispersion of liquid into droplets. The production of a simple aerosol consists of nebulizing a chemical compound dissolved in a solution. During our experiment, 1 litre of solution was formed from ultrapure water (18.2 M $\Omega$ ), in which 100 mg of the chemical compound ( $NaCl$ ,  $(NH_4)_2SO_4$ ,...) has been dissolved. Then, a supply of nitrogen ( $N_2$ ) pressure (2 bars) allows the solution to vaporize through a small orifice to form a population of polydispersed aerosols. Nitrogen is a chemically inert gas that is transparent in the visible. The atomizer produces aerosols with a stable size distribution and number density, of approximately  $2 \times 10^6$  particles/cm<sup>3</sup>. It generates droplets. In order to produce crystalline particles, an additional drying step is required, thus the use of a silica gel unit or some other types of a drier are mandatory. From these solutions, the generated aerosols have sub-micronic diameters, their median diameter

being measured around 300 nm, as shown Figure 2.3.

**Aerosol drying and homogenization:** During this study we have used two different methods for aerosol drying: a silica gel type of dryer and a membrane (Nafion) dryer. At the output of the generator, the aerosol flow is dried through a tube containing silica gel beads. This silica gel diffusion dryer is commonly used to reduce the RH of the aerosol flow. During the path of the aerosol through the silica gel filling, the water vapor of the carrier gas diffuses to the silica gel and is adsorbed by it. The reduction of RH may be controlled by the length of the dryer or by the residence time of the aerosol inside the dryer. Silica gel can remove a large amount of water of a sample but it must be reactivated and dried on a daily basis. In order to obtain an homogeneous particle size distribution, the aerosols penetrate into a buffer volume (2 L). In this volume, the RH remains higher than the ERH of most of the studied aerosols (>40%). Therefore, another drying system has been used: a nafion tube of  $\approx 30$  cm long. The aerosol flow is then dried to RH lower than 35% just before being subjected to humidification. Nafion is highly resistant to chemical attack, selective and permeable to water and impermeable to most gases. A humidity sensor (Sensirion SHT75) (RH%) is placed at the exit of the nafion tube to check the RH before the humidification.

**Humidificator - Vapor Delivery Model (VDM):** The humidifier type VDM (Vapor Delivery Model), allows a humidification of aerosol particles. This VDM contains a chamber in which ultrapure water (18.2 M $\Omega$ ) and nitrogen ( $N_2$ ) are mixed, and controlled by liquid and gas flow regulator. The VDM temperature controller allows the temperature to be adjusted according to the needs of the operator. Using specific software (Flow DDE, Flow view, Flow plot), it was possible to regulate the flow rate of water, air and the temperature of the VDM. During the experiment, a first ramp of humidity was performed to estimate the deliquescence point for each aerosol type generated. From this information, specific “scripts” for each aerosol were written to change the RH step and gain in accuracy close the DRH. One humidity ramp takes between 1 hour 30 minutes and 1 hour 45 minutes depending on the hygroscopicity of the salt. Ramp of a very hygroscopic salt takes longer time than a

salt with low hygroscopicity, in order to get a high precision on our results. During the measurements the temperature of the VDM was set to 100°C, since hot air may contain more water than cold air. The gas flow rate is set at 4 L/min. Thus by changing the flow of water in the VDM we could play on the relative humidity in the measuring instruments. The RH in our system is varied between  $\approx 30 - 90\%$  with a step of 1% RH.

After undergoing evaporation down to 30% in average and humidification up to 90% RH, aerosols arrive simultaneously in the measuring instruments (i.e. the nephelometer and the OPC). In order to avoid any turbulences within the system, both instrument flow rates were adjusted to 3 L/min each.

### **2.1.1 Aerosol size distribution measured by Optical Particle Counters (OPC)**

In order to measure the size distribution of aerosol particles, an optical particle counter (OPC) (Welas-Palás 2300) is used in this thesis as the particle sizer. The main advantage of the WELAS is that it could perform measurements at variable relative humidity ( $40\% < \text{RH} < 90\%$ ). The WELAS (WhitE Light Aerosol Spectrometer) (Palas, model 2300) is a very high resolution spectrometer. It can count and classify aerosols in 64 size bins over a wide range of diameters (0.12 to 105  $\mu\text{m}$ ), allowing to determine the number size distribution. It has excellent particle counting efficiency and can measure at high temperature (250°C) and high pressure (10 bar). The descriptive diagram of WELAS operation is shown in [Figure 2.2](#).

To analyze the scattered light of a single particle, the WELAS sizer uses the white light scattered at 90° by particles to determine their concentration and their diameter. The different parts of the instrument are: a white light source emitted by a Xenon lamp, using two biconcave lenses and a measurement volume uniformly enlightened with white light. The particle passing through this volume of measurement scatters light in all directions.

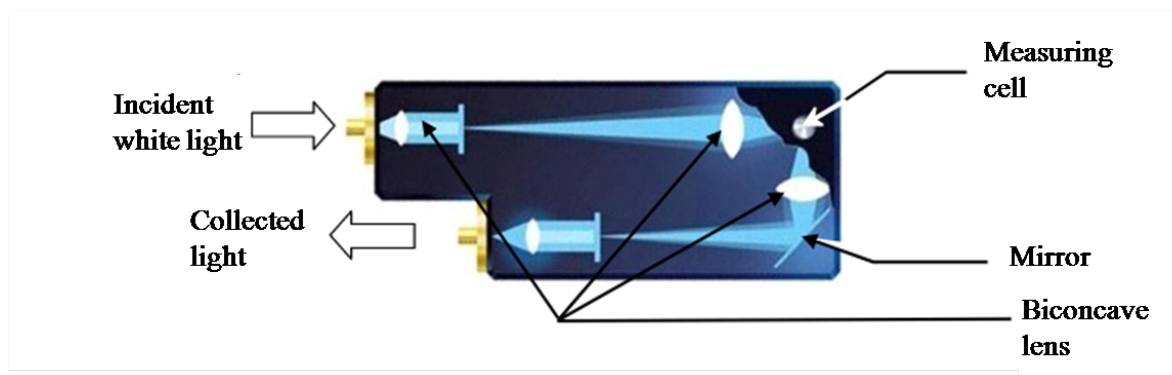


**Figure 2.2:** *WELAS operating diagram (Palas 2300) (Source:Wikipedia).*

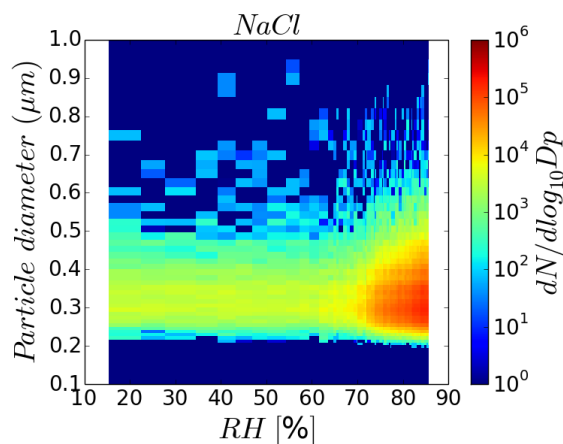


**Figure 2.3:** *Variation of the diameter and the number concentration of sodium chloride in the WELAS.*

The scattered light is then collected at an angle of  $90^\circ$ . An optical fiber allows the focusing of this signal via a set of two lenses and a mirror. This optical fiber conducts the collected signal to a photomultiplier that measures in real time the luminous intensity of the scattered signal by each particle. The height of the scattered light pulse of a single particle gives information about particle diameter, hence the optical measurement is transformed into aerosol diameter using Mie theory with the refractive index of a specific compound, and the quantity of particles is measured by the number of pulses. The coincidence of particles error is detected by the runtime measurement and is indicated by an optical warning signal. The OPC is calibrated with dust (CalDust 1100) so the scattered light equivalent diameters

related to dust is measured. A calibration curve is determined using the ratio between the white light source and the scattered light detection at  $90^\circ$ .

The relative humidity (RH) was controlled in the WELAS by the humidifier (VDM: Vapor Delivery Model) placed upstream. Figure 2.3 shows the variation of the diameter and the concentration of sodium chloride (*NaCl*) in the WELAS during the humidifying process.

### 2.1.2 Aerosol scattering coefficient measured by Nephelometer

Among aerosol properties, the light scattering coefficient ( $\sigma_{scat}$ ) is a key parameter used to characterize the radiative effect of atmospheric particles. In this study, a nephelometer (ECOTECH AURORA 3000) was used to measure the scattering ( $\sigma_{scat}$ ) and backscattering  $\sigma_{bksp}$  coefficients at different relative humidity ( $40\% < RH < 90\%$ ). The integrating nephelometer was first introduced by [Beuttell and Brewer \(1949\)](#). It can be used for ambient air monitoring as well as for laboratory measurements. The nephelometer (Figure 2.4) makes continuous and real time measurements of the light scattering at multiple wavelengths of ambient air. The light used in this instrument is LED (Light Emitting Diode) light source at three wavelengths (450 nm Blue, 525 nm Green, and 635 nm Red). The backscattering measurements are made between  $90^\circ$  and  $170^\circ$  allowing a thorough analysis of light scattering of particles, so by subtracting the backscattering measurements from the total scattering, the forward scattering can be calculated. Different parameters, such as the single scattering albedo ( $\varpi_0$ ), Angstrom exponent ( $\mathring{A}$ ), can be derived by combining this measurement to data measured by other aerosol instruments (aethalometer, particle counter...) ([Uchiyama, 2014](#)).

The presence of atmospheric particles within the measurement cell induces scattering of light, which is detected by a photo multiplier tube (PMT) that produces electrical signals proportional to the intensity of the incident light. Thus the produced signal is proportional to the scattering coefficient of the volume of air. A temperature and RH sensor measuring the temperature and the relative humidity inside the cell is mounted on top of the cell. This

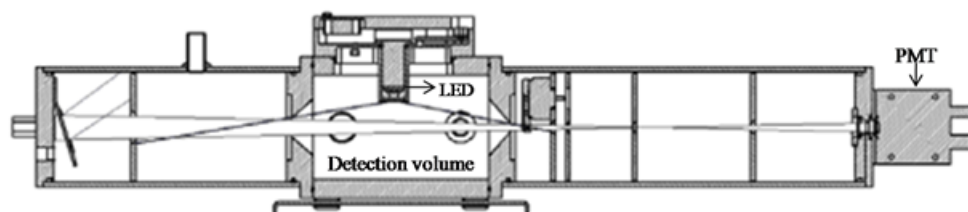


**Figure 2.4:** *Operating diagram of the nephelometer (Aurora 3000).* (Adapted from: Müller *et al.* (2011))

RH sensor will be the one used to draw the humidogramm (see Figure 2.6) used in the results sections. Therefore, a validation of nephelometer RH sensor was achieved in comparison to another sensor (Sensirion SHT75) and the RH difference between both sensors was about 1%. Furthermore, a pressure sensor that measures the pressure inside the cell is mounted on a microprocessor board, this latter converts the data from the PMT to the real values. Calibration is made by spanning a gas of well-known optical properties (carbon dioxide in this study) allowing to set the calibration coefficients for the scattering and backscattering coefficients. Moreover, to make sure the measurement cell is clean, a zero calibration is performed everyday. The nephelometer measures values between 0 and 20000  $\text{Mm}^{-1}$ , with a detection limit of 0.3  $\text{Mm}^{-1}$  over 60 seconds integration. Angular truncation errors and the non-Lambertian nature of the light source were taken into account as suggested by Müller *et al.* (2011).

Correlation between aerosol populations ( $\text{PM}_{10}$ ) measured by the OPC and the corresponding scattering coefficient at 525 nm measured by the nephelometer is described in Figure 2.5. At dry conditions ( $\text{RH} \approx 35\%$ ), aerosol were generated by atomizing synthetic solutions with two different concentrations of sodium chloride ( $\text{NaCl}$ : 500 mg/L and 1 g/L) and natural sea water collected in the North Sea out of the Dunkirk coast (1 g/L) separately. Figure 2.5 shows a linear relationship between the scattering coefficient (at 525 nm) and the particulate matter  $\text{PM}_{10}$  with a correlation factor “R” of 0.94. From the linear relation for  $\text{NaCl}$  and sea salt, one can see that the sodium chloride is a major component of sea salt particle. This result validates the use of  $\text{NaCl}$  as a proxy for sea salt aerosols.

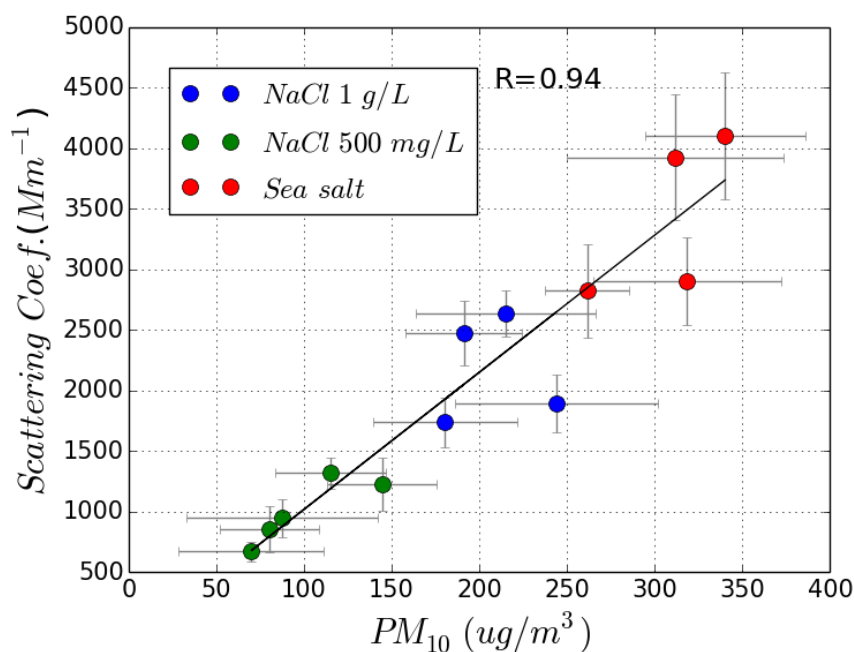


**Figure 2.5:** Scattering coefficient measured at 525 nm by the nephelometer as a function of the  $PM_{10}$  of aerosol particles with a diameter  $<10 \mu m$  measured by the OPC (GRIMM Mini-WRAS) for three different aerosol types.

In addition, to validate the use of the Beer-Lambert law described in Chapter 1, the simple scattering criterion must be valid. This criterion specifies that the total scattered intensity is the sum of the intensities scattered by each particle. Therefore, the scattering cross section, just like the absorption cross section, must be proportional to the aerosol concentration. As Figure 2.5 shows this proportionality, two conclusions can be drawn: (1) the Beer-Lambert law is verified, (2) the volume of the cell of the nephelometer can be considered as a diluted aerosol medium.

In this study, the relative humidity (RH) was controlled in the nephelometer by the humidifier (VDM: Vapor Delivery Model) placed upstream the nephelometer. By increasing the relative humidity slowly, we obtain humidograms, as shown in Figure 2.6, representing the evolution of the scattering coefficient as a function of RH measured within the nephelometer cell. The deliquescence curve of  $NaCl$  particles is shown at three different wavelengths.

Hence, based on the scattering coefficient measured both at ambient conditions and at dry conditions, we derived the scattering enhancement factor described in equation 1.16 of chapter 1. In the next section we will only show the deliquescence curve at 525 nm.

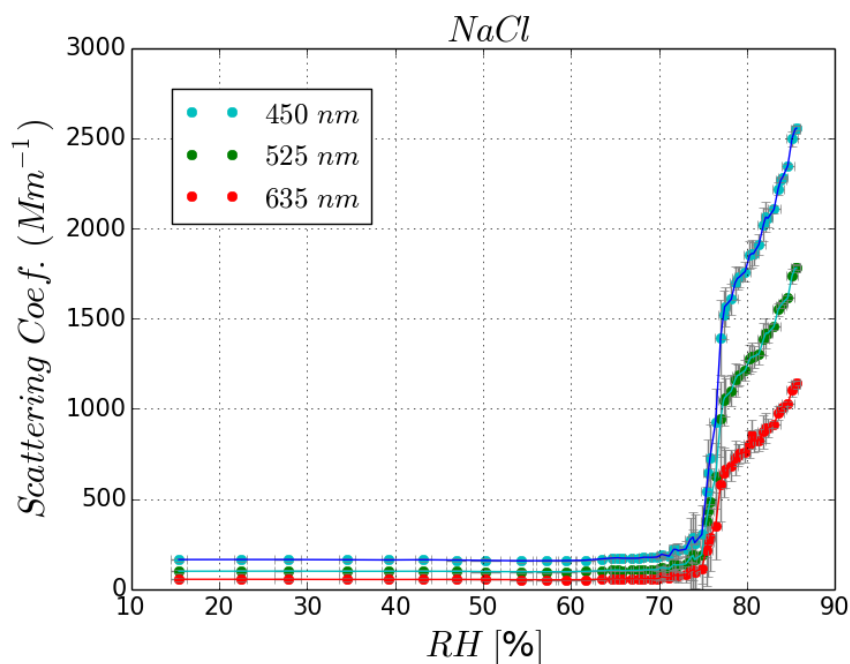


**Figure 2.6:** Humidogram representing the variation of the scattering coefficient as a function of the relative humidity for sodium chloride particles generated by atomization. The blue, green and red curves correspond to 450, 525 and 630 nm wavelengths respectively.

## 2.2 Experiment 2: Physico-chemical properties of a single particle

This second phase of the experimental work, performed during this thesis, was based on levitated particles and Raman microspectrometry. Indeed, a better understanding of the particle evolution during a humidifying process requires the characterisation of all aerosol

properties including their chemical composition. This information is provided by Raman measurements along with the phase of each compound within the aerosol.

### 2.2.1 Levitation system: Acoustic levitation

Hygroscopic growth of submicrometer aerosol particles is typically studied using HTDMA (Jing et al., 2016; Peng et al., 2016; Moore and Raymond, 2008), whereas water uptake of supermicrometer aerosol particles is generally studied by means of Raman microspectrometry Lee et al. (2008); Laskina et al. (2015). In the last case, particles are often substrate-deposited (Zhou et al., 2014). Alternatively, Raman microspectrometry is combined with levitation technique, which is a substrate-free method. Levitation devices have been particularly developed over the past ten years and used to study single particles of atmospheric interest (Cotterell et al., 2015; Krieger et al., 2012; Signorell and Reid, 2010; Lee and Chan, 2007). Indeed, these devices allow studying the physicochemical properties of single particles, with size ranges of a few microns to several hundreds of microns, without constraints of a contacting surface. Moreover, if the system is equipped with an environmental cell, it allows measurements of particle area equivalent diameter variation during the humidification. Several levitation techniques are used to study aerosol particles:

- Electrodynamic balance that allows to levitate particles ranging between 1 and 150  $\mu\text{m}$ , but require charged particles.
- Optical levitation and optical tweezers to study particles between 1 and 20  $\mu\text{m}$  in size, but adapted only for transparent and non-absorbing particles.
- Acoustic levitation to levitate particles without constraint on the physicochemical properties, but having a diameter larger than 30  $\mu\text{m}$ .

In this study, we used acoustic levitation (APOS BA 10, Tec5, Germany), which has the advantage of generating stable particles over time (Tobon et al., 2017; Seng et al., 2018b). Figure 2.7 shows the levitation system used during this work. The system used in the present

study works at 100 kHz frequency and with a 3.4 mm sound wavelength. The operating principle of acoustic levitation is described in the Annex 1. The environmental cell developed during the PhD thesis of Dr. Samantha Seng (Seng, 2017) is equipped with inlet and outlet valves for gas circulation. Aerosol particles are introduced into the cell through a hole in the lower part of the chamber. A medical nebulizer (OMRON MicroAIR U22) generates a cloud of droplets of about 5  $\mu\text{m}$  that coalesce to form larger particles. One of the three windows, made of quartz and installed on the environmental cell, allows the optical microscopic observation of a trapped droplet. A high-speed high-resolution video camera CMOS monochrome (Basler Ace NIR, 2048 $\times$ 2048 pixels), was used to take photos of the particle during the experiment to follow the morphological evolution of the individual particle with a temporal resolution of 180 images per second. This camera is connected to a computer to view the image and record photos and videos in real time, using HIRISx64 and Camera Tool software.

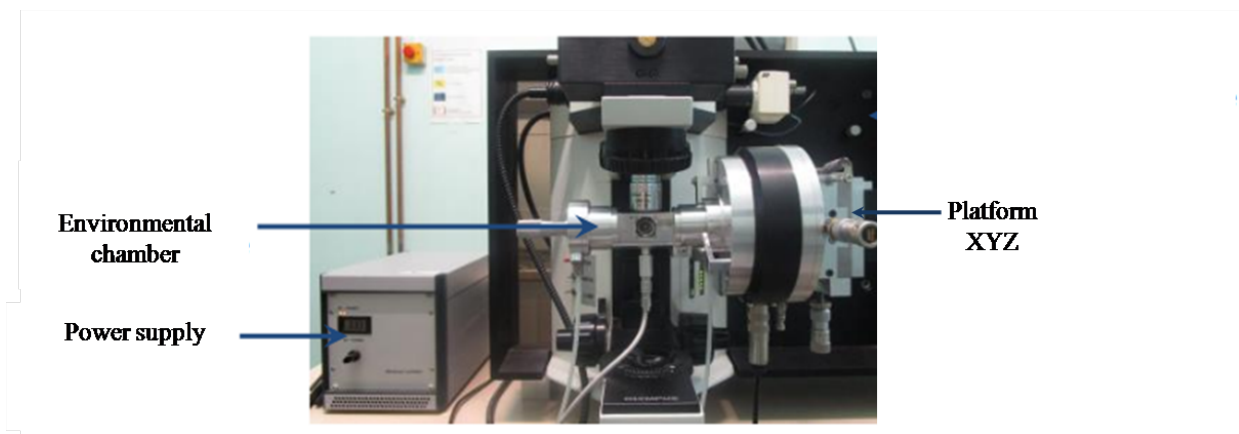


**Figure 2.7:** *Photo of the experimental levitation device coupled to the Raman microscope.*

To avoid dehydration of the particle and to ensure its stability during the experiments, maintaining a constant humidity in the cell is required. Relative humidity control is provided using a humidifier which is connected to the environmental chamber. The humidifier is a bubbler equipped with a flowmeter that allows the user to control the vapor quantity at the output. The relative humidity and the temperature are measured by a sensor (Sensirion

SHT75) in the environmental chamber at about 6 mm of the trapped particles with accuracy of  $\pm 0.9\%$ . Within the cell, the RH values vary between 10 and 90% with a step of 1% RH. This system has demonstrated to give confident results in the deliquescence point determination (Seng et al., 2018b). Figure 2.8 show an example of optical images for *NaCl* particle obtained during the humidifying process.

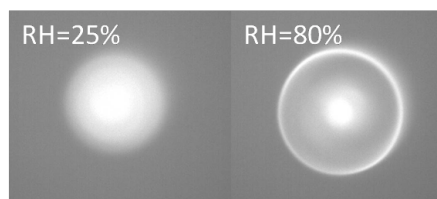


**Figure 2.8:** *Optical image of sodium chloride particle levitated in air at different relative humidities.*

## 2.2.2 Aerosol chemical composition and physical properties

Adapted environmental cells coupled to Raman microspectrometry were used in our study to monitor the physical and the chemical properties of substrate-deposited and acoustically levitated single particles. Thus, modifications of the aerosol diameter and chemical composition can be observed simultaneously during the humidifying process.

During this study, LabRAM HR Evolution(Horiba Scientific), a fully integrated confocal Raman microscope, was used. A HeNe laser that delivers a monochromatic radiation at 633 nm with an output power of approximately 8.4 mW has been used. The Raman effect consists in the inelastic scattering of light involving the elementary vibrations of matter. Raman scattering is the result of the light-matter interaction and comes from molecular and crystalline vibrations. For an isolated nonlinear molecule with  $n$  atoms,  $3n-6$  normal modes of vibration are expected. Each normal vibrational mode corresponds to a normal coordinate  $Q$  (Wilson et al., 1955). Figure 2.9 shows the vibrational states involved during

the excitation of a molecule.

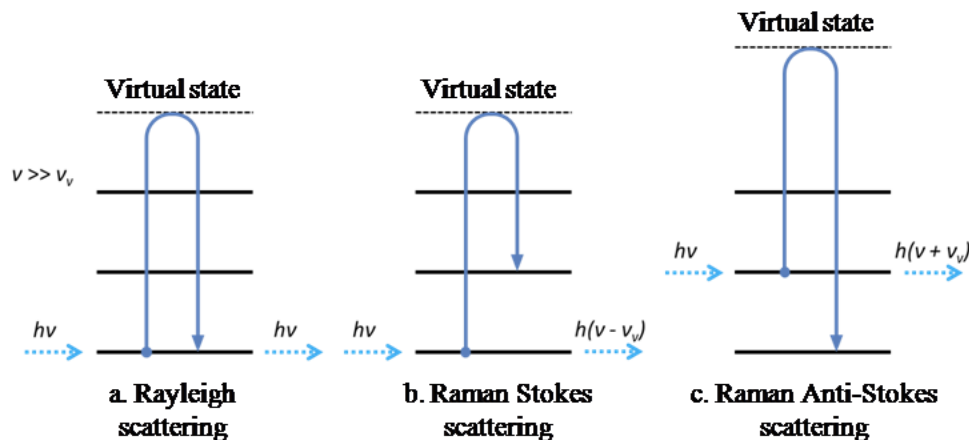


**Figure 2.9:** Principle of Raman scattering (Source: *Barbillat et al. (1999)*).

The  $\nu$  frequency incident radiation is very large compared to the  $\nu_v$  vibrational transition. Under the effect of excitation, molecules diffuse light in all directions of space. This light is composed of two types of radiation: (i) an elastically scattered radiation: Rayleigh scattering in which incident and reemitted photons have the same energy and (ii) inelastically scattered radiation. It consists of two contributions: (i) Raman Stokes scattering in which the frequency of scattered photons is shifted by  $(-\nu_v)$  with respect to incident light. (ii) Anti-Stokes scattering in which the frequency of scattered photons is shifted by  $(+\nu_v)$  with respect to incident light.

A unique and characteristic information of the bond vibrations in the molecule is given by the scattered light (Stokes and Anti-Stokes). The difference of energy between two vibrational levels is represented by the Raman shift. The Raman spectrum shown in Figure 2.10 consists of peaks or bands marked by the Raman shift expressed in wavenumber ( $\text{cm}^{-1}$ ). The Raman spectrum contains various information, thus each band of the spectrum can be characterized mainly by its position in the spectrum, that is related to the frequency of a vibrational mode, and by its intensity, that is related to the number of scattered molecules

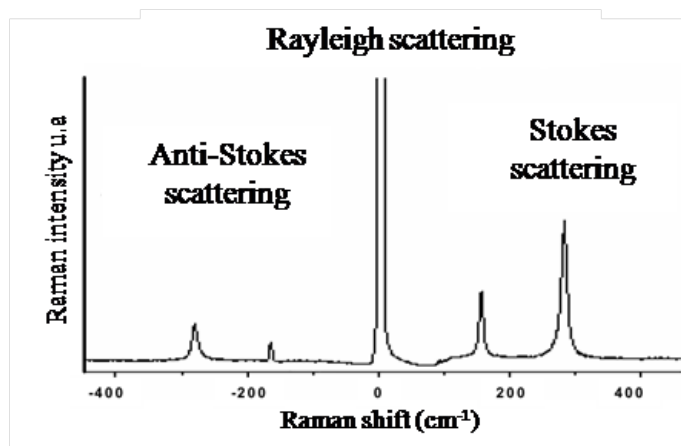


**Figure 2.10:** Raman scattering spectrum Stokes and anti-Stokes of calcite,  $\lambda_{ex} = 632 \text{ nm}$ .

as well as the considered vibrational mode. Hence, the Raman spectrum of a liquid particle is representative of the molecular vibrations in the different orientations of the molecules and their dynamics. Thus, the Raman bands of a liquid particle are larger in comparison to a solid particle in which the molecular vibrations are weak. The vibrational spectroscopy of crystals has been detailed in earlier work (Turrell, 1972).

Raman spectrometry enables us to get a deeper view of the chemical composition of multi-component aerosol particles, levitated or substrate-deposited, placed inside an environmental cell. Using the medical nebulizer (OMRON MicroAIR U22), aerosol particles were generated and levitated or deposited on a  $\text{CaF}_2$  substrate. The choice of this substrate was made according to its spectrum that has a limited number of bands in the spectral range of interest in this study (Figure 2.11).

As there is no specific band in the region between  $850$  and  $4000 \text{ cm}^{-1}$ ,  $\text{CaF}_2$  can be used as a substrate for our aerosol mixtures of interest. The humidifier (the same as the one used for the levitation system) was connected to the environmental cell. Images of substrate-deposited particles were taken during the humidification. Acquisition of spectra at different RH was conducted using LabSpec 6 (Horiba Jobin Yvon). During this work, Raman spectra of single particles were acquired using an excitation laser operating at  $633 \text{ nm}$  and using a

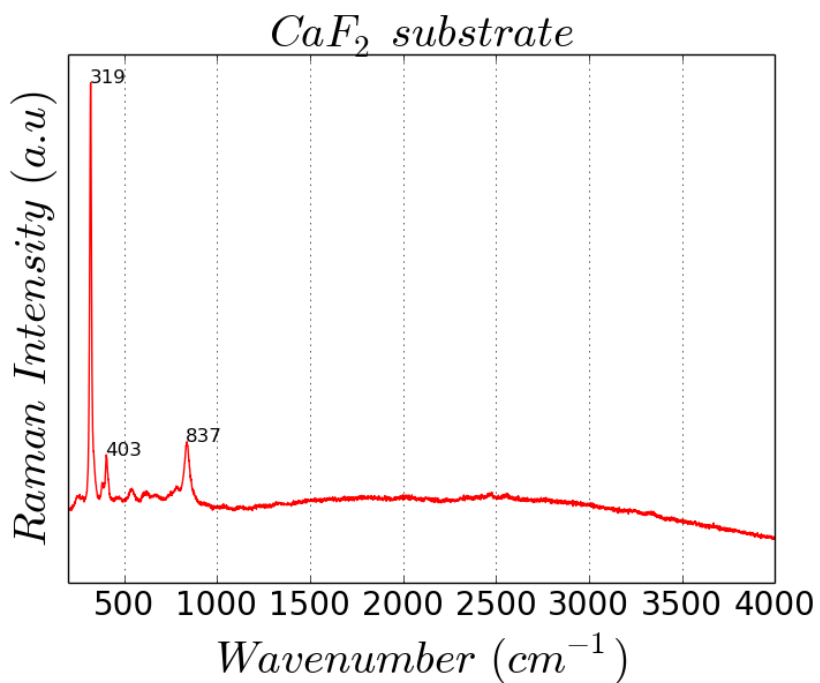


**Figure 2.11:** Raman spectra of  $CaF_2$  substrate obtained with HeNe laser light at 633 nm.

diffraction grating with 600 gr/mm (pixel resolution: 1  $cm^{-1}$ /pixel).

## 2.3 Conclusion

In this chapter, we describe the operating mode of the devices that allowed us to generate aerosols, as well as the various instruments used to measure aerosol optical (nephelometer), chemical (Raman microspectrometer) and physical (optical microscope) properties. All these instruments were adapted or modified to perform measurements over a large range of RH (up to 95%). The observations performed could therefore be used to better characterize and understand the evolution of aerosol chemical, physical and optical properties during the humidifying process, with in particular the phase transition. Up to date, there is no study that coupled all these instruments together. This unique set up will allow to achieve the main objective of this thesis, which is to determine the variation of aerosol properties while increasing the relative humidity, and to compare results given by different measurement techniques, and models.

---

---

## CHAPTER 3

---

# Hygroscopic growth properties of pure aerosols

Aerosol particles produced in the atmosphere can be pure (a single chemical component) or more complex (internal mixture of 2 or more compounds). In the case of mixed particles, aerosol properties, such as hygroscopicity, optical and physico-chemical properties are more difficult to predict. Indeed, complex interactions of aerosols with water are difficult to quantify without making separate measurements of pure compounds. By working in a controlled atmosphere, single or multi-component mixtures of aerosols can be studied under chosen temperature and humidity conditions, while limiting additional chemical reactions. A huge array of literature reports laboratory studies of specific aerosol properties of single-component aerosols (Denjean et al., 2014; Zieger et al., 2017; Jing et al., 2017; Lee and Hsu, 2000). These laboratory measurements of single-component aerosols under controlled atmospheric conditions enable to establish or to verify parameterizations to describe their interactions with water. This approach mimics/simulates simplified aerosol under idealised atmospheric conditions. This chapter is dedicated to the hygroscopic measurements of single component aerosols generated in the laboratory. We will focus on four main pure inorganic aerosol species of atmospheric relevance: sodium chloride ( $NaCl$ ), ammonium sulfate ( $(NH_4)_2SO_4$ ), potassium chloride ( $KCl$ ), and sodium nitrate ( $NaNO_3$ ).  $NaCl$  is representative of sea-salt aerosols, one of the most abundant aerosol species in the troposphere, due to their production over the oceans that cover more than 70% of the Earth's Surface (Seinfeld and Pandis, 2006). Ammonium sulfate aerosols are a well-known dominant component of the aerosol mass in the atmosphere, especially in the  $PM_{2.5}$  fraction. Potassium chloride is representative of biomass-burning aerosol particles, in which the inorganic fraction includes different compounds such as  $KCl$ ,  $KNO_3$ , and  $K_2SO_4$  (Freney et al., 2009). Generally, potassium and chloride are the most abundant ions from the biomass smoke emissions (Jing et al., 2017). Compared to potassium nitrate and potassium sulfate,  $KCl$  has a lower deliquescence relative humidity (DRH at 85%, from Freney et al. (2009)) and stronger hygroscopicity after deliquescence. Finally, nitrate salt particles are ubiquitous in the troposphere, especially in urban/polluted areas, because of their secondary production due to anthropogenic emissions of  $NO_x$  from the combustion of fossil fuels (Seng et al., 2018a; Jing et al., 2018). The majority of nitrate salts in ambient particles exist as  $NH_4NO_3$ ,  $NaNO_3$

and  $Ca(NO_3)_2$  depending on the environmental conditions and chemical formation mechanisms. Field measurements and laboratory studies have indicated that sea salt ( $NaCl$ ) emitted from natural sources could undergo atmospheric aging through the heterogeneous reactions with nitric acid or nitrogen oxides, resulting in the formation of  $NaNO_3$ .

Both experimental setups, described in Chapter 2, have been used to investigate the effect of variable relative humidity on aerosol optical, physical and chemical properties. These two approaches are complementary, however one needs to keep in mind that the size of the aerosols generated in each experimental setup differs by 1-2 orders of magnitude. Such a difference could generate differences on hygroscopic parameters. Despite this limitation, combining the two approaches provides measurements of the variability of diameter (using particle sizers), morphology (using optical microscopy), hygroscopicity (physical state, i.e. liquid/deliquesced/solid, provided by Raman spectroscopy), and optical properties (scattering coefficient measured by nephelometry) of synthetic aerosols undergoing simplistic atmospheric processing limited to one variable, i.e. RH (using a humidification system).

### 3.1 Determination of the DRH

The ZSR method is generally applied in atmospheric aerosol models to retrieve the aerosol hygroscopic properties. According to previous studies, ZSR method has not been validated for aerosol mixtures composed of sea salt ([Svenningsson et al., 2006](#)). Therefore, we will, first, focus on single-component aerosols such as sodium chloride  $NaCl$ , ammonium sulfate  $(NH_4)_2SO_4$ , potassium chloride  $KCl$  and sodium nitrate  $NaNO_3$ . Table 3.1 gives the density, the molar mass and the purity of each of these components.

The density is a key parameter to define in the OPC settings (WELAS) and the molar mass is used to calculate the molar fraction of a component in an aerosol mixture (chapter 5).

**Table 3.1:** *Parameters of synthetic aerosol particles used in the laboratory experiments.*

Salt	Density (g/cm <sup>3</sup> )	M (g/mol)	Purity (%)
<i>NaCl</i>	2.165	58.44	99.99
$(NH_4)_2SO_4$	1.77	132.14	99.999
<i>KCl</i>	1.98	74.55	-
<i>NaNO<sub>3</sub></i>	2.26	85.01	>99.0

### 3.1.1 Aerosol population

Using the experimental setup described in section 2.1, the variation of the scattering coefficient measured by the nephelometer as a function of the relative humidity allowed us to calculate the scattering enhancement factor (described in section 1.4.2.2). For each pure aerosol component considered in this experiment, i.e., *NaCl*,  $(NH_4)_2SO_4$ , *KCl*, and *NaNO<sub>3</sub>*, the dry scattering coefficient is first measured at low RH (20% in this work). Then, humidograms of the  $f(RH)$  variation as a function of RH are determined, as shown Figure 3.1. Each experiment for the four aerosol components has been repeated for at least three times in order to validate the determination of the DRH value as well as the value of the  $f(RH)$  at the highest relative humidity (around 90%).

The values of the deliquescence relative humidity (DRH), specific to each aerosol component, are retrieved from these humidograms using two different methods. The first method, developed during this work, defines the DRH point as  $f(RH)$  differences larger than 0.5 for two successive points. The second method defines the DRH point as the value corresponding to a first derivative of the cubic interpolation of the curve equal to 0. Both methods give similar DRH values. DRH for *NaCl*,  $(NH_4)_2SO_4$  and *KCl* are retrieved at  $75.6\pm 1\%$ ,  $79.9\pm 1\%$  and  $82\pm 1\%$  respectively (represented by light blue dots on the deliquescence curves, Figures 3.1a, 3.1b and 3.1c). In a general point of view, these values are consistent with the values previously reported within the literature, i.e,  $75.3\pm 0.1\%$  for *NaCl*,  $79.9\pm 0.5\%$  for  $(NH_4)_2SO_4$ , and  $84.2\pm 0.3\%$  for *KCl*, as previously shown in Table 1.2 of Chapter 1 (Tang (1996b));

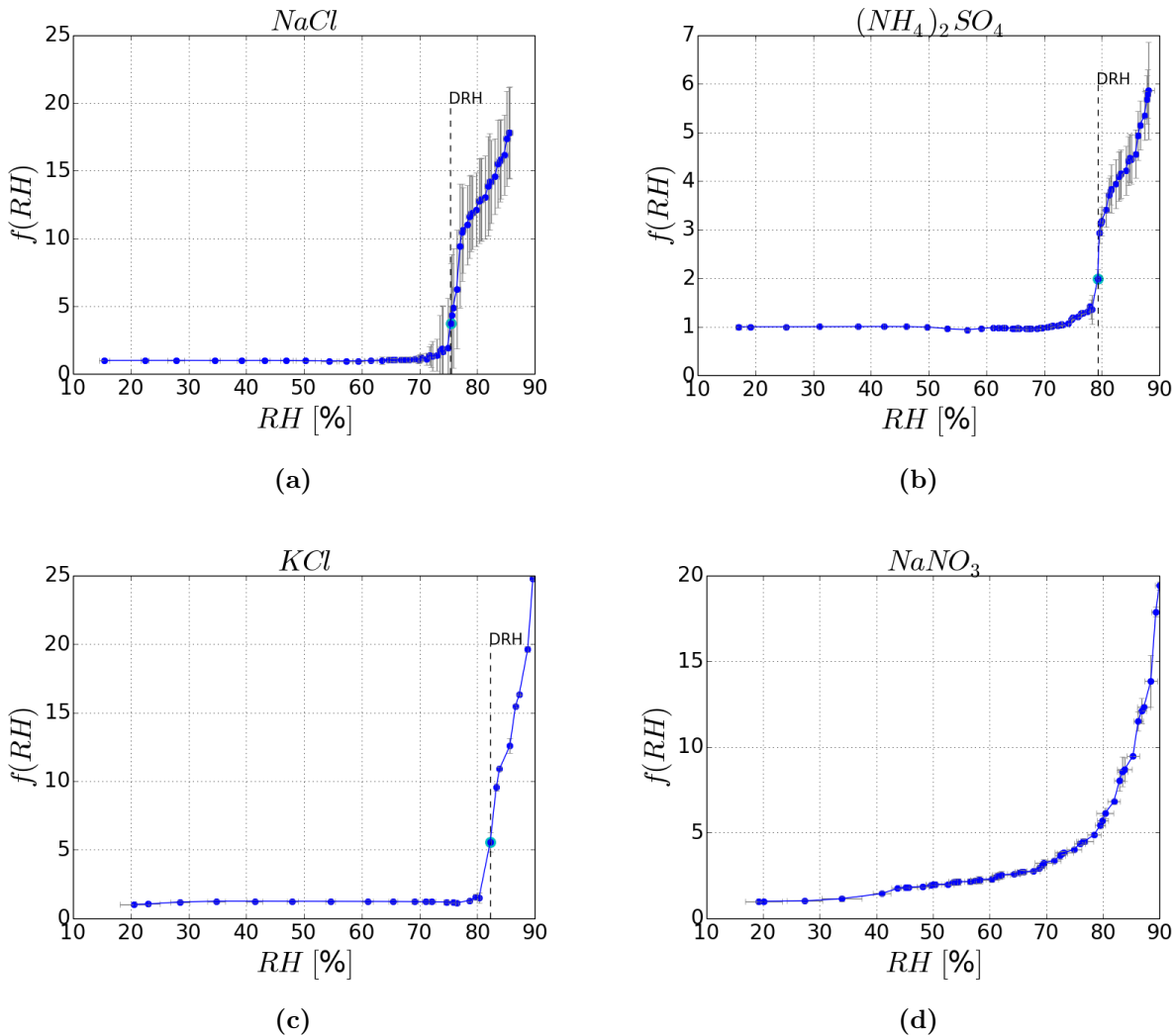


**Figure 3.1:** Variation of the scattering enhancement factor as a function of relative humidity for sodium chloride (a), ammonium sulfate (b), potassium chloride (c) and sodium nitrate (d). The light blue dots represent the deliquescence relative humidity for each component. Sodium nitrate shows no DRH (see text for more details).

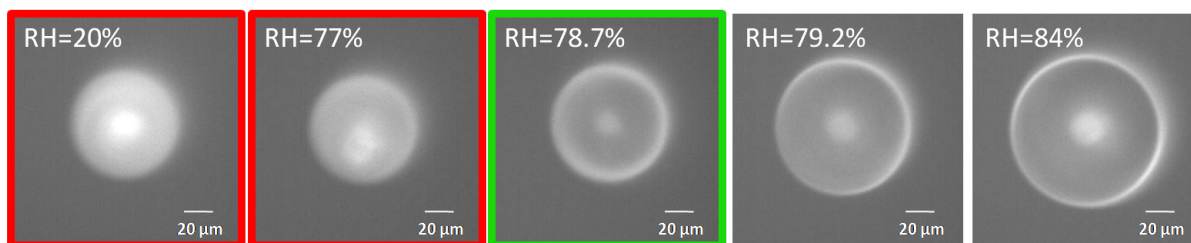
Tang and Munkelwitz (1993, 1994a); Martin (2000)). Despite a small difference of 2% in the DRH determined with our method and the literature value for *KCl*, this relatively good agreement between literature results and DRH determinations allows us a first validation of the experimental approach and method used here to determine the DRH. As shown in

Figure 3.1d,  $NaNO_3$  particles show no DRH, but a continuous increase in  $f(RH)$  with RH. Although not systematic, such a behavior has been previously reported by some studies, like Lee and Hsu (2000), with the absorption of water by  $NaNO_3$  particles beginning at around 25% of RH.

From these results, it is clearly observed that,  $NaCl$  particles are the most hygroscopic aerosol type, with the lowest DRH and the higher  $f(RH)$  values at each RH. As an example,  $f(85\%)$  of  $NaCl$  is observed at 17, while  $f(85\%)$  of  $(NH_4)_2SO_4$ ,  $KCl$ ,  $NaNO_3$  are observed at 4.5, 13 and 13, respectively. It is interesting to note that, even if the DRH of  $KCl$  particles is high (82%), the increase of  $f(RH)$  is steep and the  $f(RH)$  can reach a value of 25 at RH equal to 90%.

### 3.1.2 Single particle

The levitation experimental setup, described Section 2.2, allows to observe the evolution of the particle diameter with increasing RH from the optical images, which are used to calculate  $g(RH)$ . Figure 3.2 presents the optical images of  $(NH_4)_2SO_4$  particles levitated in air during the humidifying process. The images with red borders show the dried particle and the one with green borders represent the particle at the DRH point. This DRH point is determined using two methods: first, when visually observing a white layer (of water) bordering the particle and secondly, by calculating the growth factor as a function of RH, the DRH being reached when  $g(RH) > 1$  (see section 3.3 for more details). As illustrated in Figure 3.2, for RH values lower than 78.7%, the diameter of the particle remains constant at 60  $\mu m$ . At RH=78.7% we observe a small increase in size (about 15%). For RH values beyond 78.7%, the particle size is steadily increasing with the RH. DRH values determined by this approach for  $(NH_4)_2SO_4$  and  $NaCl$  are listed in Table 3.2. Unfortunately,  $KCl$  and  $NaNO_3$  were not studied using the optical microscope approach during this thesis.



**Figure 3.2:** *Optical images of an ammonium sulfate ( $(NH_4)_2SO_4$ ) particle levitated in air during humidifying process. The images with red and green borders represent the dried particle and the particle at the DRH respectively.*

**Table 3.2:** *Results of the deliquescence relative humidities of synthetic aerosol particles measured and calculated in comparison with literature data. The method used in the literature are based on HTDMA for  $NaCl$ ,  $(NH_4)_2SO_4$  and  $KCl$  and on optical microscopy for  $NaNO_3$ .*

Salt	DRH(%)				
	optical microscopy	nephelometry	ISORROPIA-II	E-AIM	literature
$NaCl$	$76.1 \pm 0.5$	$75.6 \pm 1$	75.3	75.3	$74.3 \pm 1.5$ (Zieger et al., 2017)
$(NH_4)_2SO_4$	$78.7 \pm 0.5$	$79.9 \pm 1$	79.9	80.3	$78.9 \pm 4.3$ (Denjean et al., 2014)
$KCl$	-	$82 \pm 1$	84	-	84 (Jing et al., 2017), 85 (Freney et al., 2009)
$NaNO_3$	-	Not observed	74	74	$74.0 \pm 0.5$ (Gupta et al., 2015), Not observed (Lee and Hsu, 2000)

For  $NaCl$  and  $(NH_4)_2SO_4$ , the DRH values derived from the nephelometer measurements of the aerosol population and from the optical microscope analysis of a single particle are in good agreement. For  $NaCl$  aerosol particles, the value of DRH obtained for a single particle using the levitation cell coupled to the optical microscope and the one obtained with the setup of optical properties based on  $\sigma_{scat}$ , are very close, i.e. DRH of about 76.1% and 75.6%, respectively. Moreover, ISORROPIA-II and E-AIM (Clegg et al. (1998)) calculations are also presented in Table 3.2. Both thermodynamic models retrieve a DRH value of 75.3%, which is in rather good agreement with our experimental values. Based on the HTDMA method,

Zieger et al. (2017) found a DRH at  $74.3\% \pm 1.5$ , a value which is slightly lower than those derived by the two experimental methods deployed in this thesis, but which remains within the error bars of DRH determinations from these different methods, which vary between 0.5 and 1.5%. As reported in Table 3.2, for  $(NH_4)_2SO_4$  aerosol particles, the DRH are determined at 78.7% and 79.9% based on the optical microscope analysis of a single particle and on  $f(RH)$  measurements of the aerosol population, respectively. The DRH calculated by thermodynamic models are 79.9% with ISORROPIA-II and 80.3% with E-AIM. Thus, our experimental and simulated values of DRH are within 1% difference, which correspond to the uncertainties of the RH sensors. In addition, our results are consistent with those of Denjean et al. (2014), who observed a DRH value equal to  $78.9 \pm 4.3\%$  for ammonium sulfate particles, using a HTDMA in an atmospheric simulation chamber.

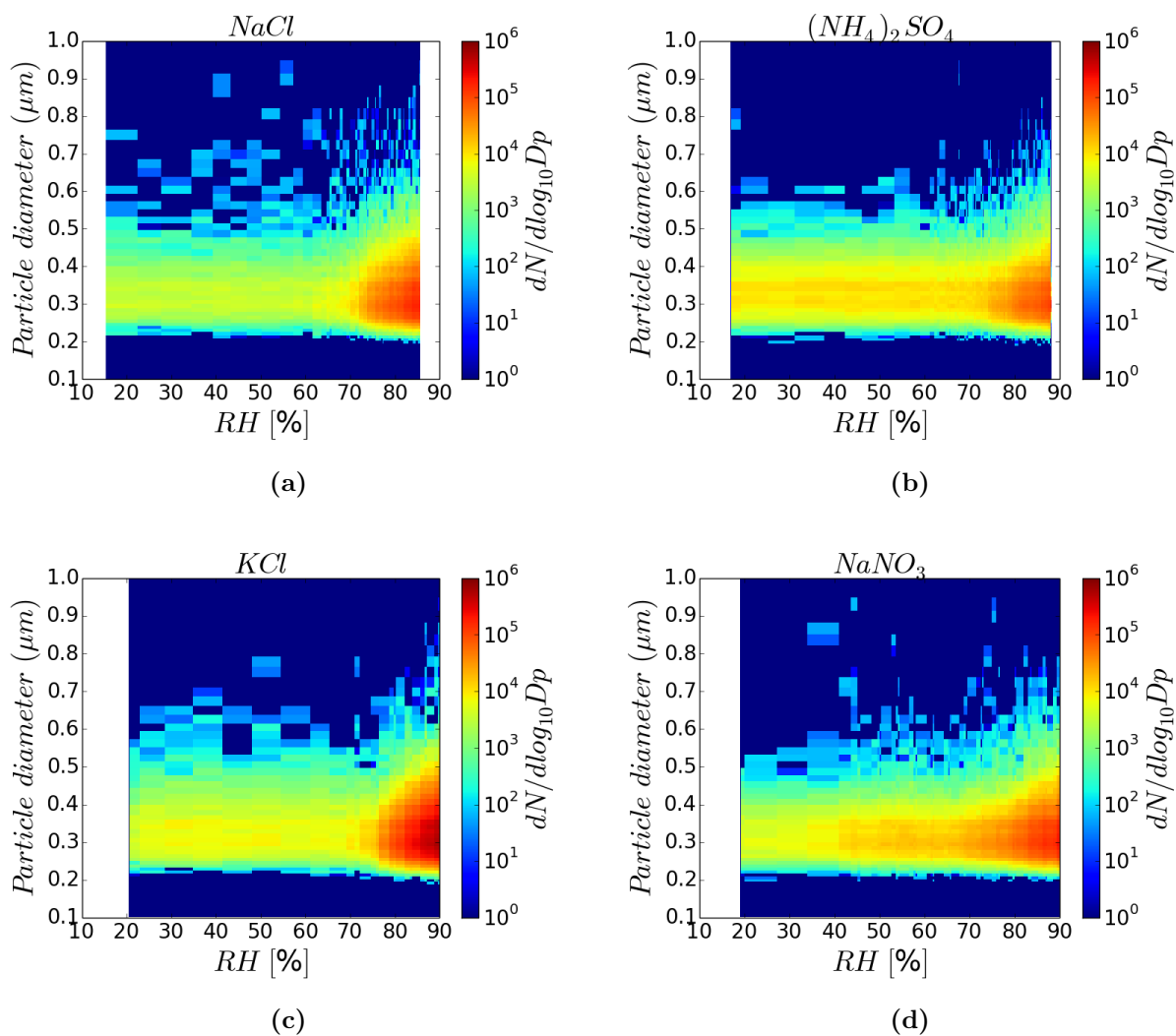
For *KCl* particles, the DRH experimental value ( $82 \pm 1\%$ ) determined by the nephelometer measurements of the aerosol population shows good agreement with both the ISORROPIA-II model (84%) and previous measurements based on optical microscopy reported in the literature (84%, Jing et al. (2017)). Indeed, the difference between these values is moderate (2%).

During our experiments, based on nephelometer measurements,  $NaNO_3$  particles did not show any deliquescence point based on  $f(RH)$  evolution. This result, which is consistent with the study of Lee and Hsu (2000), is probably due to the presence of some seeds in bigger particles. Indeed, the probability to find seeds decreases with the size of the particle. However, recently, Seng et al. (2018a) found a DRH of 75% for a  $NaNO_3$  acoustically levitated particle, using the same setup than the one used in this study, which is in agreement with the value of 74% calculated by the ISSORROPIA-II and E-AIM models and determined experimentally by Gupta et al. (2015). These discrepancies between different experimental approaches to measure or not the phase transition (DRH) during the humidifying may be attributed to different nucleation mechanisms (i.e. homogeneous and heterogeneous) for pure and impure (seed containing)  $NaNO_3$ , as previously discussed in Kim et al. (2012).

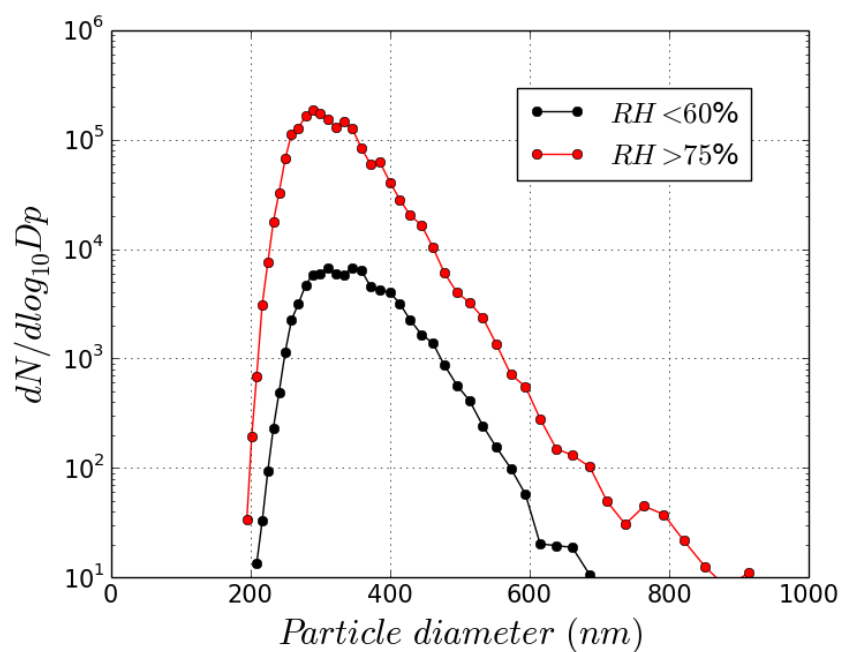
## 3.2 Effect of RH on aerosol population diameter

Figure 3.3 shows the variation of the diameter and the number concentration of aerosol particles measured by the OPC (WELAS) as a function of relative humidity, for the four compounds considered in this thesis. The aerosol number concentrations are represented by the color bar. Each figure correspond to different aerosol types:  $NaCl$ ,  $(NH_4)_2SO_4$ ,  $KCl$ ,  $NaNO_3$ . At RH lower than DRH, the mean particles diameters are observed at 300 nm for  $NaCl$ ,  $(NH_4)_2SO_4$  and  $KCl$ , as illustrated Figure 3.4 for  $NaCl$ . A shift towards particles of larger diameter (second mode at 765 nm, shown Figure 3.4) can be observed at RH corresponding to or larger than the DRH.

Figure 3.3 illustrates that the aerosol total concentration increases after the DRH value, which is specific for  $NaCl$ ,  $(NH_4)_2SO_4$  and  $KCl$  particles. For  $NaNO_3$  particles (Figure 3.3d), the concentration increase starts at lower relative humidity, i.e. at 40% of RH. The only explanation of this result is that aerosols, smaller than the OPC cut off diameter, can be generated and are not counted at RH lower than the DRH. When the RH reaches the DRH, aerosol size increases and the uncounted particles are now measured by the OPC. It can be noted that this increasing has also been shown by Denjean et al. (2014), while working on  $(NH_4)_2SO_4$  aerosol particles. As an example, Figure 3.4 shows the size distribution modification associated to different RH conditions, for  $NaCl$  particles. The mean size distribution is shown for RH conditions less than 60%, where the diameter remains constant while increasing RH, and for RH values greater than 75%, where the deliquescence point of  $NaCl$  appears and the size of particles increases. Each dot represents an average of (9 and 20 values for RH <60% and RH >75% respectively) the particle concentration for a specific diameter. When the RH is lower than 60% (black curve), only one mode is observed and centered at 300 nm as previously stated. Whereas, for wet aerosols (red curve), size distribution shows 2 modes with a new mode of smaller intensity centered at 765 nm.



**Figure 3.3:** Variation of the diameter (*y* axis) and the number concentration (colorbar) of aerosol particles as a function of relative humidity for sodium chloride (a), ammonium sulfate (b), potassium chloride (c) and sodium nitrate (d).



**Figure 3.4:** Averaged size distributions of NaCl aerosol particles measured for dry ( $<60\%$ ) and wet ( $>75\%$ ) conditions.

### 3.3 Hygroscopic growth factor measurements

As previously stated, in the second experimental setup, the aerosol diameter of a single particle has been measured from the optical images obtained with an optical microscope coupled to the levitation cell. From images measured at different RH,  $g(\text{RH})$  of the single particle is derived. The directly measured  $g(\text{RH})$  is reported in Figure 3.5. For *NaCl* and  $(\text{NH}_4)_2\text{SO}_4$ , this directly measured  $g(\text{RH})$ , is compared to  $g(\text{RH})$  determined from the scattering enhancement factor  $f(\text{RH})$  (derived from scattering measurements of the aerosol population) using Guo's equation (see demonstration in chapter 1 equation 1.21) (Guo et al., 2015; Bougiatioti et al., 2016). Figure 3.5 compares the evolution of the directly measured (black curve) and from  $f(\text{RH})$  measurement (red curve) derived  $g(\text{RH})$  as a function of the relative humidity. The  $g(\text{RH})$  evolutions are relatively similar for *NaCl* and  $(\text{NH}_4)_2\text{SO}_4$  particles, except some small differences. The  $g(\text{RH})$  of *NaCl* particles, directly measured in the levitation cell shows a decrease to a value of 0.93 before the deliquescence transition (black curve of Figure 3.5a). This slight decrease in size is due to the water absorption in the lattice defects of the solid particle, which produces a rearrangement of the crystal lattice (Gupta et al., 2015).

At the DRH,  $g(\text{RH})$  derived from the  $f(\text{RH})$  measurements on the aerosol population is observed around 1.93 for *NaCl* and 1.41 for  $(\text{NH}_4)_2\text{SO}_4$ , particles. For comparison,  $g(\text{RH})$  directly measured from the optical microscopy images are observed at 1.31 for *NaCl* and 1.56 for  $(\text{NH}_4)_2\text{SO}_4$  particles. These differences between the  $g(\text{RH})$  measured by these two approaches may be due to the differences of aerosol initial sizes in each experiment. Indeed, to measure  $f(\text{RH})$  within the nephelometer, aerosols are generated as a population of particles with a main mode centered at 300 nm. Within the levitation cell, a single particle with a dry diameter around 60  $\mu\text{m}$  is observed. One would expect that the  $g(\text{RH})$  should be larger for larger particles as observed for  $(\text{NH}_4)_2\text{SO}_4$  particles. However, the opposite trend is found for *NaCl*. Further analysis and measurements would be necessary to better understand this behavior for a monodisperse aerosol of different size as highlighted by Alshawa et al. (2009) and Hewitt and Jackson (2009).

The  $g(\text{RH})$  values derived from the scattering enhancement factor at the DRH are consistent with previous studies (Wise et al., 2003; Topping et al., 2005; Gupta et al., 2015; Hu et al., 2010; Hewitt and Jackson, 2009). Indeed, as shown Table 3.3 the difference is at maximum about 1.5% and 3.5% for  $\text{NaCl}$  and  $(\text{NH}_4)_2\text{SO}_4$  particles, respectively. For RH values higher than the DRH, the difference we observe between the directly measured  $g(\text{RH})$  and  $g(\text{RH})$  derived from  $f(\text{RH})$  measurements is about 10% for both aerosol types. Moreover, at 80% RH, the value of  $g(\text{RH})$  derived from  $f(\text{RH})$  is about 3.4 for  $\text{NaCl}$  particles and 1.7 for  $(\text{NH}_4)_2\text{SO}_4$ , which confirms that  $\text{NaCl}$  is more hygroscopic.

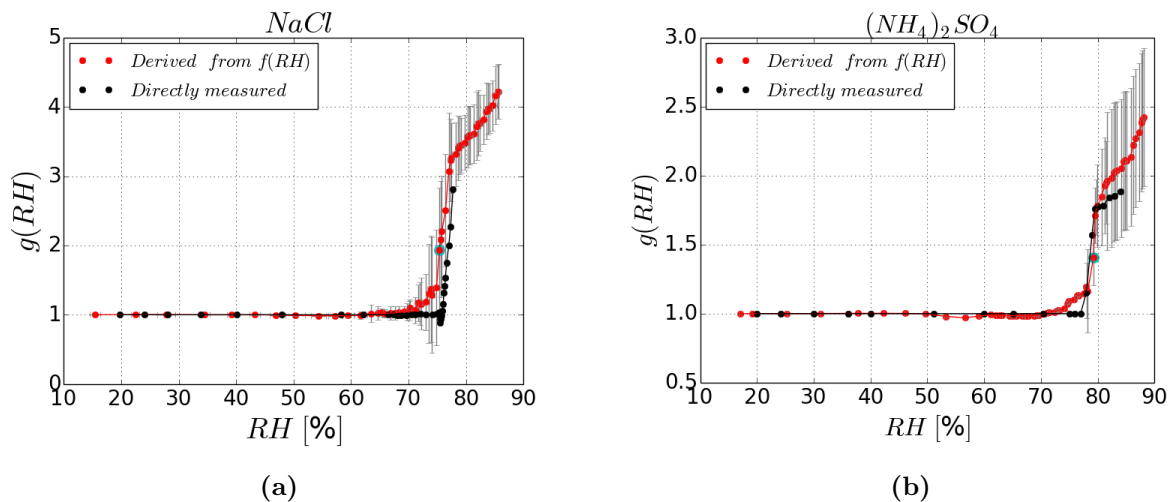


**Figure 3.5:** Hygroscopic growth factors retrieved from the scattering enhancement factor for an aerosol population (red) and measured from the optical images provided by the optical microscope of the levitation setup for a single particle (black) for sodium chloride (a) and ammonium sulfate (b) aerosols.

For  $\text{KCl}$  particles, we only retrieved the  $g(\text{RH})$  from  $f(\text{RH})$  nephelometer measurements. Compared to previous studies, the retrieved  $g(\text{RH})$  for  $\text{KCl}$  at DRH is equal to 2.36, while Jing et al. (2017) as well as Carrico et al. (2010) observed  $g(\text{RH})$  of 1.8 at the DRH (Table 3.3). It is important to note that Jing et al. (2017) performed their study using 100 nm particles. Thus, measurements with a DMA would be mandatory to be able to compare

more robustly these studies taking into account the differences in the particles sizes. This is valid for all compounds investigated in this study.

**Table 3.3:** *Hygroscopic growth factor retrieved and measured at the deliquescence relative humidity of each component and comparison to literature data.*

Salt	g(RH) at DRH		
	Directly measured (optical microscopy)	Derived from f(RH) (nephelometry)	Litterature
<i>NaCl</i>	1.31	1.93	$\approx 1.9$ (Topping et al., 2005; Hewitt and Jackson, 2009; Hu et al., 2010; Gupta et al., 2015)
$(NH_4)_2SO_4$	1.56	1.41	$\approx 1.45$ (Wise et al., 2003; Topping et al., 2005; Hewitt and Jackson, 2009; Hu et al., 2010)
<i>KCl</i>	-	2.36	$\approx 1.8$ (Jing et al., 2017; Carrico et al., 2010)

From our study of pure synthetic aerosols we deduce the values of the DRH for different compounds then we calculate the g(RH) at different RH using both experimental setups for *NaCl* and  $(NH_4)_2SO_4$  and we compare the values of the g(RH) at DRH with literature data. We choose now to study the effect of the relative humidity on aerosol mixtures of both compounds.

### 3.4 Conclusion

In this chapter, we presented the optical and physical properties of pure aerosols (*NaCl*,  $(NH_4)_2SO_4$ , *KCl* and *NaNO<sub>3</sub>*) measured using two experimental setups. The first one for an aerosol population based on nephelometer, the second one for a single particle from optical microscopy. To provide a first validation of both approaches, we first present the

methods allowing to retrieve the DRH from the measured  $f(\text{RH})$  (aerosol population) and  $g(\text{RH})$  (single particle). The retrieved DRH from these two experimental setups are relatively consistent, as well as in reasonable agreement with calculations from thermodynamic models (E-AIM, ISORROPIA-II) and previous values reported in the literature. As an example, the  $\text{NaCl}$  DRH is retrieved at 75.3% from both models and at 76.1% from the optical microscopy images analysis and measured at 75.6% from the nephelometer measurements performed in our laboratory approach. Good consistency is also obtained from the comparison of the two experimental setups used in this work, models and literature for  $(\text{NH}_4)_2\text{SO}_4$ . These results bring us confidence in our setups as well as on the database to further study aerosol properties evolution with RH.

In order, to harmonize the hygroscopic factors measured from both methodologies, we used the Guo's equation to convert the measured scattering enhancement factor ( $f(\text{RH})$ ) to a growth factor ( $g(\text{RH})$ ). Our results show that  $g(\text{RH})$  derived from  $f(\text{RH})$  measurements of an aerosol population, and directly measured from optical microscopy images, for a single particle, are not similar, with differences which may be explained by the size difference of aerosols considered in the two experiments. The  $g(\text{RH})$  for  $(\text{NH}_4)_2\text{SO}_4$  is retrieved at 1.41 from  $f(\text{RH})$  measurements, while the optical microscopy image analysis suggest  $g(\text{RH})$  of 1.56. A larger  $g(\text{RH})$  is expected from optical microscopy analysis, where the particle is super-micronic, in comparison to nephelometer measurements where aerosols are sub-micronic. If this is verified for  $(\text{NH}_4)_2\text{SO}_4$ , the opposite behavior is observed for  $\text{NaCl}$ . To fully understand this result, additional measurements, using a classifier would be necessary.  $g(\text{RH})$  values for  $\text{NaCl}$ ,  $(\text{NH}_4)_2\text{SO}_4$  have been directly measured by optical microscopy and compared to retrievals from Guo's equation applied to measurements of the scattering coefficient ( $f(\text{RH})$ ). Both approaches for  $g(\text{RH})$  can be used to evaluate the application of the ZSR method for the calculation of the  $g(\text{RH})$  of aerosol mixtures. Except for  $\text{KCl}$ ,  $g(\text{RH})$  retrieved with Guo's equation are consistent with measurements from previous studies (Topping et al., 2005; Gupta et al., 2015; Hewitt and Jackson, 2009). Therefore, in the next chapter, the retrieved  $g(\text{RH})$  from  $f(\text{RH})$  measurements will be used to test and validate the ZSR method for aerosol binary mixtures.



---

---

## CHAPTER 4

---

# Hygroscopic behavior of mixed aerosol population

Complex particles (mixture of compounds) can be present in the atmosphere due to processes like condensation of condensable gases or particle coagulation. Among the synthetic aerosols analysed in this thesis, we will first focus on aerosols of simple composition and whose hygroscopic properties are relatively well known from a theoretical point of view. Since *NaCl* is the dominant component of the sea-salt mixture (Figure 2.5), aerosol properties of mixed-salt that contain *NaCl* are predominant within the atmosphere. Therefore a better knowledge of these aerosols is deemed essential. This chapter is dedicated to the study of hygroscopic properties of multi-component synthetic aerosols generated in the laboratory, by using optical and physical properties measured by in-situ instruments.

These measurements will be then used to test the ZSR (Zdanovskii-Stokes-Robinson) method (described in section 1.4.4) currently used in atmospheric aerosol models to calculate the growth factor of an aerosol mixture as a function of the RH. According to [Cohen et al. \(1987\)](#) this ZSR method gives good results except for aerosol mixtures composed of salts. Experimental results of three and more than three ion mixtures, including  $Na^+$  and  $Cl^-$ , will be used to verify this mathematical relation and try to better understand the discrepancies between measured and calculated  $g(RH)$ . The  $g(RH)$  of mixed aerosols will be estimated using the ZSR method with pure aerosols  $g(RH)$  as inputs. The calculated  $g(RH)_{ZSR}$  values will then be compared to the  $g(RH)$  derived from the  $f(RH)$  measurements (equation 1.21 [Guo et al. \(2015\)](#); [Bougiatioti et al. \(2016\)](#)).

[Choi and Chan \(2002\)](#) found that the growth factors of *NaCl* mixed with organic compounds were lower than the growth factor of pure *NaCl*. We will see that even a small fraction of *NaCl* can greatly influence the hygroscopic behavior of other salts.

## 4.1 Mixing of 3 ions

During this thesis, we observed that the complexity of the mixing is related to the number of ions interacting within the solution. Therefore, as a first step, simple mixtures composed of 3 ions (i.e  $Na^+$ ,  $Cl^-$ ,  $K^+$  and  $Na^+$ ,  $Cl^-$ ,  $NO_3^-$ ) were generated.

## 4.1.1 NaCl/KCl mixing

### 4.1.1.1 Experimental results

The effect of aerosol composition and the potential interactions between its constituent species have an impact on the hygroscopicity. Aerosol properties of internally-mixed aerosols having an ion in common, i.e an aerosol formed by 3 ions, have been reported in previous studies (Gupta et al., 2015; Jing et al., 2018). We choose to study the case of *NaCl/KCl* mixture formed by  $Na^+$ ,  $K^+$  and  $Cl^-$  ions. Aerosol particles composed of *NaCl* and *KCl* were generated. A solution of these latter was prepared by mixing both components. Figure 4.1a shows the measured scattering enhancement factor ( $f(RH)$ ) as a function of RH for *NaCl/KCl* mixture containing 56% of *NaCl* in comparison with pure salts (*NaCl* -gray- and *KCl* -black-). The results are averaged over a window of 10% RH (Figure 4.1b) (representing an average of approximately 10 values for  $RH < DRH$  and approximately 20 values when the RH values approach to the DRH).

By applying both methods on raw measurements (described in chapter 3 section 3.1.1 (Aerosol population)) to estimate DRH, we observe that the mixed aerosol DRH ( $DRH_{mixture}$ ) is lower than each pure aerosol DRH. Indeed, the  $DRH_{mixture}$  is equal to  $71.8 \pm 1\%$  while for  $X_{NaCl} = 0$  (pure *KCl*) the DRH is equal to  $82 \pm 1\%$  (black curve) and for  $X_{NaCl} = 1$  (pure *NaCl*) the DRH is equal to  $75.6 \pm 1\%$  (gray curve). Previous studies studying the same mixing but with different fraction of *NaCl* have been published. According to Tang and Munkelwitz (1993), using single-particle levitation technique, the mixed aerosol DRH containing 66% mass of *KCl* and 34% mass of *NaCl* occurs at RH of 72.7%. Similarly, using single-particle levitation technique, Tang (2000) has observed the DRH at 72.5% for a mixture containing 80% *KCl* and 20% *NaCl*. Furthermore, the DRH at the eutonic point (70% of *KCl* and 30% of *NaCl*), which represents the molar fraction for which only one phase transition is observed, at  $72.2 \pm 0.5\%$  (Li et al., 2014). During their study they used a “see-through” inertial impactor apparatus equipped with an optical microscope to study the hygroscopic properties of the particle (Ahn et al., 2010). All these results, for *NaCl/KCl*

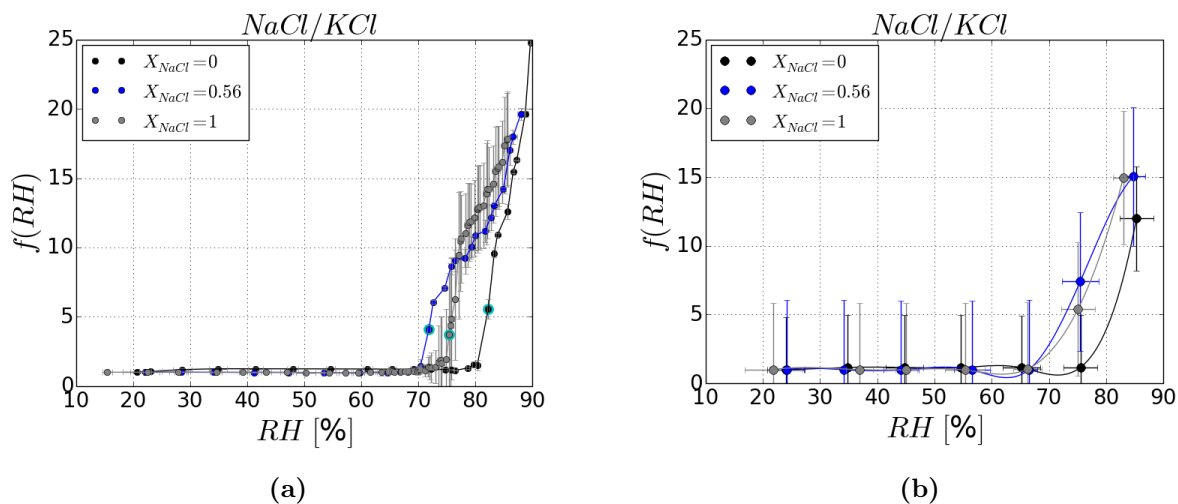


**Figure 4.1:** Variation of the scattering enhancement factor with the relative humidity for  $\text{NaCl}/\text{KCl}$  mixture containing 56% of  $\text{NaCl}$  and 44% of  $\text{KCl}$  (blue curve) and for pure components ( $\text{NaCl}$ : grey,  $\text{KCl}$ : black) that compose this mixture obtained directly from measurements (a) and averaged over a window of 10% RH (b). The DRH is represented by the light blue dots in figure a.

mixing with different fractions of  $\text{NaCl}$ , show a lower  $\text{DRH}_{\text{mixture}}$  in comparison to each pure component DRH. As previously explained, equations of Gibbs-Duhem proved the fact that the DRH of an electrolyte is lowered when a second electrolyte is added (Wexler and Seinfeld, 1991).

Figure 4.2 shows the results obtained during this work (red dots) in comparison to those found in the literature (black dots) cited above. We can observe that the DRH values for the mixture of these 3 ions ( $\text{Na}^+$ ,  $\text{K}^+$  and  $\text{Cl}^-$ ) are approximately the same, and independent of the molar fraction of  $\text{NaCl}$  within the mixture. Moreover, one can see that the  $\text{DRH}_{\text{mixture}}$  value is close (about 3% of difference) to the DRH of pure  $\text{NaCl}$ .

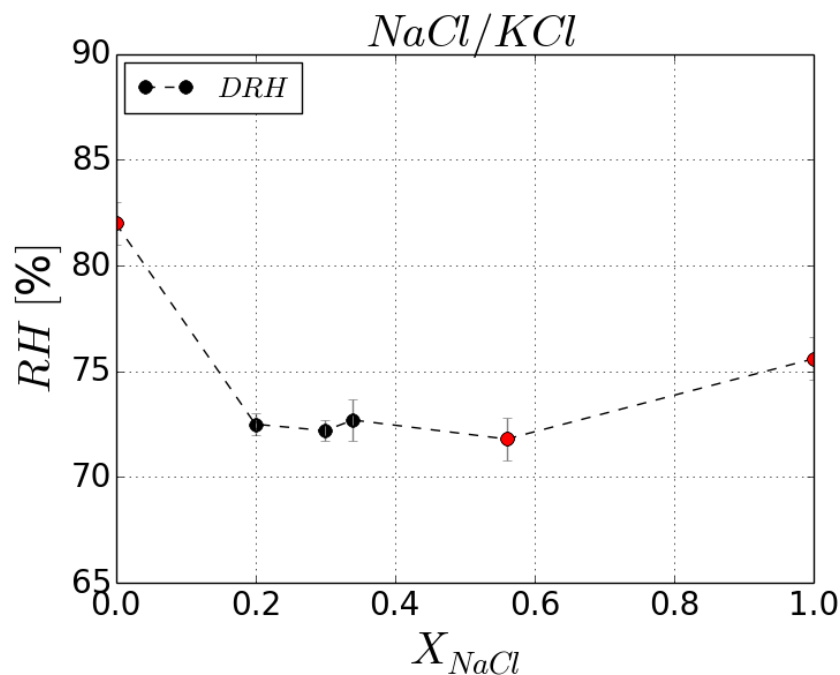


**Figure 4.2:** DRH variation of  $NaCl/KCl$  with the different molar fractions of  $NaCl$  obtained during this study (red dot) and based on literature data (black dots). Sources: [Tang \(2000\)](#); [Li et al. \(2014\)](#); [Tang and Munkelwitz \(1993\)](#)

#### 4.1.1.2 Comparison to the ZSR

From the growth factor of pure aerosols ( $NaCl$  and  $KCl$ ), the calculation of the  $g(RH)_{ZSR}$  of this mixture by applying the ZSR method is achievable.  $g(RH)_{ZSR}$  was calculated using mean value of the  $g(RH)$  averaged over a 10% window of  $RH$ . These  $g(RH)_{ZSR}$  (black curve) will be then compared to the retrieved growth factor deduced from  $f(RH)$  measurements (blue curve) for the  $NaCl/KCl$  mixture (Figure 4.3).

This figure demonstrates that for  $NaCl/KCl$  mixing ( $X_{NaCl} = 0.56$ ), composed of 3 ions, there is a good agreement between the  $g(RH)$  derived from  $f(RH)$  measurements and the  $g(RH)_{ZSR}$ . The largest discrepancies are observed at  $RH$  values close to the DRH. Indeed, at the DRH,  $g(RH)$  retrieved from the  $f(RH)$  is equal to 1.86, while the  $g(RH)_{ZSR}$  is still

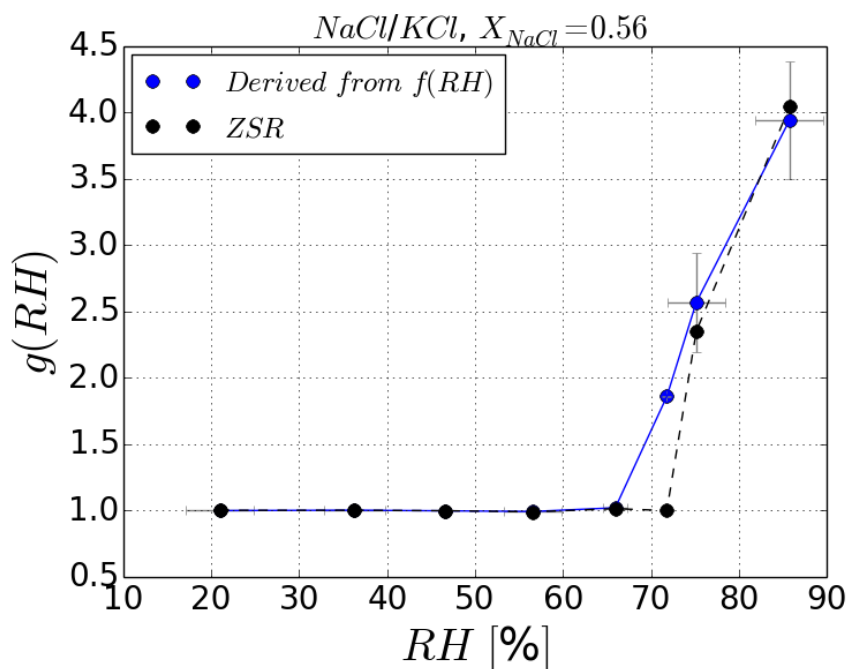


**Figure 4.3:** Comparison of the growth factor retrieved from optical measurements (scattering enhancement factor) and predicted using the ZSR method for the  $NaCl/KCl$  mixture ( $X_{NaCl} = 0.56$ ).

equal to one. When the RH reaches the  $DRH_{mixture}$  (71.8%), both pure aerosols have not yet desiccated. As the  $DRH_{mixture}$  is close to the DRH value of pure  $NaCl$ , the  $g(RH)$  underestimation by the ZSR is then limited to a small range of RH. For larger RH ( $RH > DRH_{NaCl}$ ), a better agreement between measured and ZSR computed  $g(RH)$  is observed. As the  $DRH_{mixture}$  for all fractions of  $NaCl$  are very similar (Figure 4.2), one can conclude that  $g(RH)$  evolution with RH for all fractions of  $NaCl$  will be similar to those shown in Figure 4.3. Therefore  $g(RH)_{ZSR}$  seems to be a good approximation of the measured  $g(RH)$ , at least for this  $NaCl/KCl$  mixture.

## 4.1.2 NaCl/NaNO<sub>3</sub> mixing

### 4.1.2.1 Experimental results

To evaluate the validity of the ZSR for another aerosol mixture made of 3 ions, measurements were performed on aerosol mixtures composed of *NaCl* and *NaNO<sub>3</sub>* (3 ions : i.e *Na<sup>+</sup>*, *Cl<sup>-</sup>*, *NO<sub>3</sub><sup>-</sup>*). Figure 4.4 shows the  $f(RH)$  variation with the relative humidity for pure *NaNO<sub>3</sub>* (black curve), pure *NaCl* (gray curve) and for the mixture containing 26 (red curve), 49 (blue curve), 68 (yellow curve) and 85% (green curve) of *NaCl*.

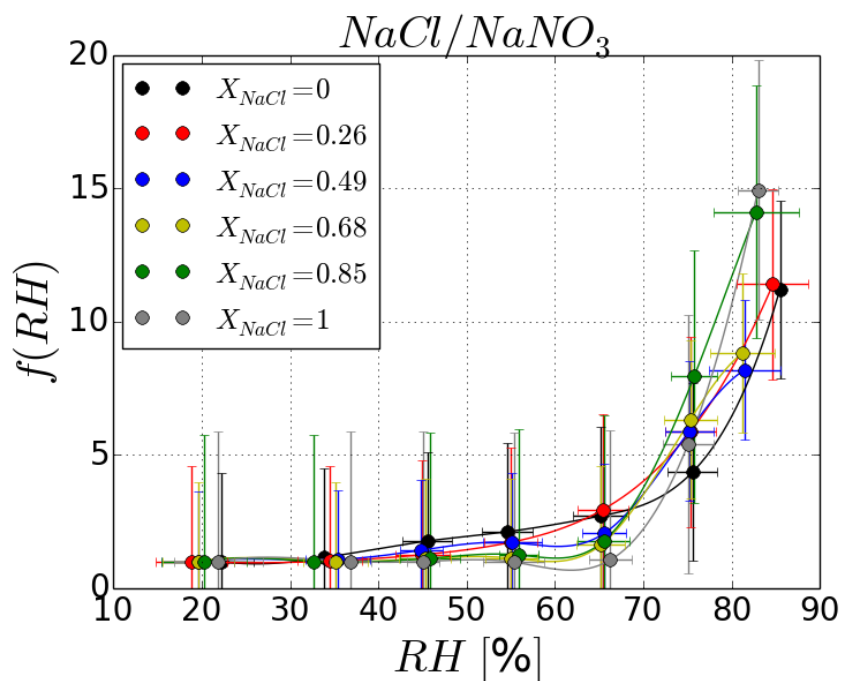


**Figure 4.4:** Variation of the scattering enhancement factor as a function of the relative humidity for *NaCl/NaNO<sub>3</sub>* mixture containing 0 (black), 26 (red), 49 (blue), 68 (yellow), 85 (green), 100% (grey) of *NaCl*.

Each dot represents the mean value of the  $f(RH)$  averaged over a 10% window of RH. As previously reported, the  $f(RH)$  of *NaNO<sub>3</sub>* ( $X_{NaCl} = 0$ , black curve) particles is increasing constantly with RH, while the *NaCl* deliquesced at  $75.6 \pm 1\%$  ( $X_{NaCl} = 1$ , gray curve). The

$f(\text{RH})$  value at high RH conditions, i.e.  $\text{RH} > 80\%$  is equal to  $15 \pm 3$  for pure  $\text{NaCl}$  and  $11 \pm 3$  for pure  $\text{NaNO}_3$  (black curve), due to the more hygroscopic properties of  $\text{NaCl}$ . Logically,  $f(\text{RH})$  of the mixture of these two compounds is getting closer to the pure aerosol  $f(\text{RH})$ , when the fraction of one of the two components is minimum.

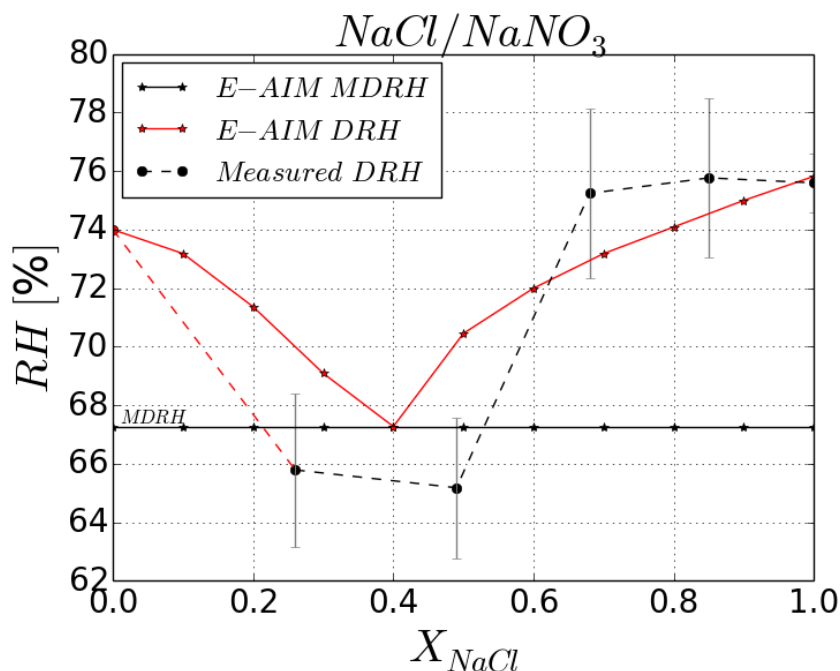


**Figure 4.5:** DRH variation of  $\text{NaCl}/\text{NaNO}_3$  as a function of  $\text{NaCl}$  molar fractions obtained during this study (black dots, dashed line) and DRH and MDRH values calculated using E-AIM (red and black lines)

From the  $f(\text{RH})$  measurements (Figure 4.4),  $\text{DRH}_{\text{mixture}}$  composed of 3 ions ( $\text{Na}^+$ ,  $\text{Cl}^-$ ,  $\text{NO}_3^-$ ) were calculated as a function of  $\text{NaCl}$  fraction (Figure 4.5). Contrariwise to the  $\text{NaCl}/\text{KCl}$  mixture, the  $\text{DRH}_{\text{mixture}}$  values for aerosols containing  $\text{NaCl}$  and  $\text{NaNO}_3$  critically depend on  $\text{NaCl}$  molar fraction in the mixture. Moreover, in this case ( $\text{NaCl}/\text{NaNO}_3$ ), the lowest  $\text{DRH}_{\text{mixture}}$  value does not correspond to the lowest DRH of the pure compounds within the mixing.  $\text{NaNO}_3$ , in comparison to  $\text{NaCl}$ , has the lowest theoretical DRH, with a value of 74% computed by thermodynamical models (see Table 3.2 of Chapter 3), and the lowest  $\text{DRH}_{\text{mixture}}$  is observed at  $65.2 \pm 2\%$ . This large difference (about 9%) may have large

impact on the ZSR calculations.

To better understand the observed  $DRH_{mixture}$  values, we choose to use the E-AIM model to calculate the MDRH (black line) and the DRH (red line) for this mixing (Figure 4.5). The computed MDRH value of this mixture is equal to 67.3%. The lowest  $DRH_{mixture}$  values measured ( $65.2 \pm 2\%$  and  $65.8 \pm 2.6\%$ ) are close to the computed MDRH of the mixing, and the associated  $NaCl$  fractions (0.26 and 0.49) are close to the eutonic composition ( $X_{NaCl} = 0.38$ ). While for molar mixture fractions  $X_{NaCl} = 0.68$  and 0.85, the obtained  $DRH_{mixture}$  values, of  $75.2 \pm 2.6\%$  and  $75.8 \pm 2.4\%$ , are close to the theoretical  $DRH_{mixture}$  values, computed with E-AIM model (73 and 74.5% respectively).

#### 4.1.2.2 Comparison to the ZSR

Figure 4.6 represents  $g(RH)$  of the  $NaCl/NaNO_3$  mixture predicted by the ZSR at different RH values (black curves) and retrieved from  $f(RH)$  measurements (colored curves). Each dot represents the mean value of the  $g(RH)$  calculated from pure aerosol  $g(RH)$ , or derived from  $f(RH)$  measurements averaged over a 10% window of RH. For  $X_{NaCl} = 0.26$ ,  $g(RH)_{ZSR}$  underestimates the one retrieved from  $f(RH)$  measurements by 32% at  $RH = 65\%$  and up to 40% at  $RH = 75.7\%$ . At high RH ( $RH = 85\%$ ),  $g(RH)_{ZSR}$  overestimates by 19% the measurement retrievals. As shown in Figure 4.6b, the same discrepancies can be observed for  $X_{NaCl} = 0.49$ .

Figure 4.6c and 4.6d show that for larger fractions of  $NaCl$  ( $X_{NaCl} = 0.68$  and 0.85),  $g(RH)$  retrieved from  $f(RH)$  measurements show no increase for RH values up to  $< 70\%$ . The effect of  $NaNO_3$ , characterized by a  $g(RH)$  constantly increasing with RH, is lowered by the high  $NaCl$  fraction. Indeed, the  $g(RH)_{ZSR}$  computed value is equal to 1.14 while it is equal to 1 when retrieved from the measurements (Figure 4.6c). This result highlights the effect of NaCl on the measurements. Adding  $NaCl$  to the mixing has, indeed, a strong effect on the hygroscopic properties of the mixing. This effect is again unpredictable by the ZSR parametrisation. For  $X_{NaCl} = 0.85$ , Figure 4.6d shows that the differences between both computed and measured  $g(RH)$  are lowered in comparison to lower  $NaCl$  fractions. ZSR

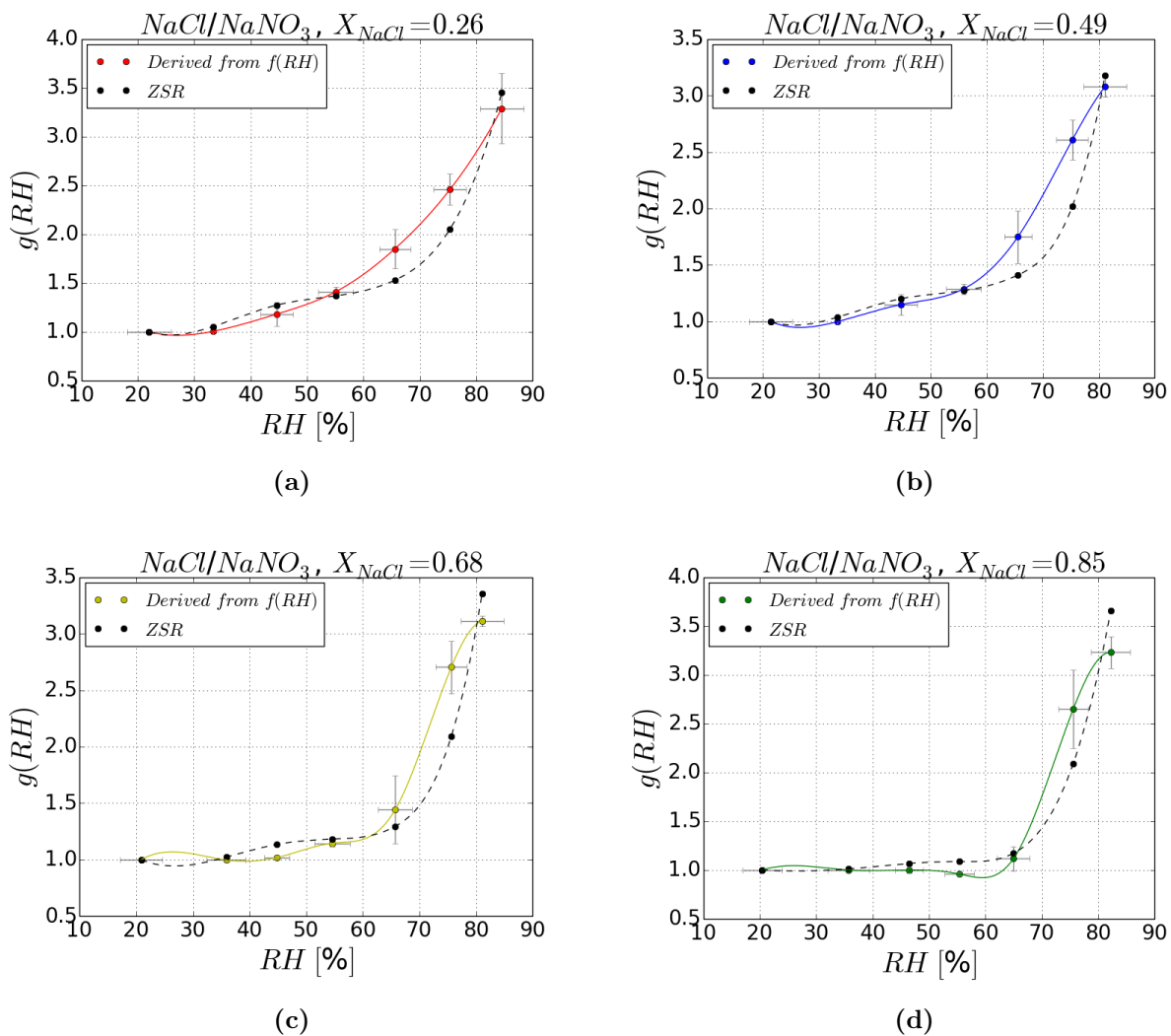


**Figure 4.6:** Comparison of the growth factor retrieved from optical measurements (scattering enhancement factor) (colored curves) and predicted using the ZSR method (black curves) for 26 (a), 49 (b), 68 (c), 85 (d) % of  $NaCl$  in  $NaCl/NaNO_3$  mixture.

underestimates (overestimates) retrieved  $g(RH)$  by 52% (42%) at  $RH=75.5\%$  ( $RH=82.5\%$ ). Indeed, at  $RH=75.5\%$   $g(RH)$  retrieved from measurements is equal to 2.64 while  $g(RH)_{ZSR}$  is 2.12. Conversely, at  $RH=82.5\%$ ,  $g(RH)$  value retrieved from our measurements is equal to 3.23, while the computed  $g(RH)$  is 3.65, highlighting an overestimation of the value derived from the ZSR relationship.

To conclude, our experimental results have highlighted a few discrepancies between ZSR calculations and the measurements performed over a large range of RH. ZSR is a mathematical relation allowing to retrieve  $g(\text{RH})_{\text{mixture}}$  based on the pure compounds  $g(\text{RH})$ . Therefore, if  $\text{DRH}_{\text{mixture}}$  occurs at lower RH than that of its pure compounds (meaning that mixed particle adsorbs water at lower RH than the pure compounds), the  $g(\text{RH})_{\text{ZSR}}$  will be underestimated from the  $\text{DRH}_{\text{mixture}}$  until the DRH lowest value for pure compounds. As the  $\text{DRH}_{\text{mixture}}$  of the first fractions of the  $\text{NaCl}/\text{NaNO}_3$  mixing ( $X_{\text{NaCl}} = 0.26$  and  $X_{\text{NaCl}} = 0.49$ ) are much lower than the pure compounds, there are large differences between  $g(\text{RH})_{\text{ZSR}}$  in comparison to measurements. For the two higher fractions of  $\text{NaCl}$  in  $\text{NaCl}/\text{NaNO}_3$  mixture, ZSR results are more reliable because the  $\text{DRH}_{\text{mixture}}$  ( $\approx 75\%$ ) is very similar to the DRH of pure  $\text{NaCl}$  ( $75.6 \pm 1\%$ ). While studying the case of  $\text{NaCl}/\text{KCl}$  the ZSR has shown relatively good results (except at the  $\text{DRH}_{\text{mixture}}$ ). Similarly to the last two fractions of the  $\text{NaCl}/\text{NaNO}_3$  mixture, the difference between  $\text{DRH}_{\text{mixture}}$  ( $\approx 72\%$ ) and pure  $\text{NaCl}$  DRH ( $75.6 \pm 1\%$ ) is low. Overall, from our results obtained from the two 3 ion aerosol mixtures considered in our mixture experiments, i.e.,  $\text{NaCl}/\text{KCl}$ , and  $\text{NaCl}/\text{NaNO}_3$ , we can infer that the ZSR method is validated only when  $\text{DRH}_{\text{mixture}}$  is close to the DRH of one of the pure aerosol compounds composing the mixture. A more complex mixture is studied in the next section.

## 4.2 Mixing of more than 3 ions

An internally mixture of aerosols having no ion in common, i.e an aerosol composed by more than 3 ions, is more complicated and uneases the study of aerosol hygroscopicity. This kind of mixture is often observed in real atmospheric aerosols. It is therefore fundamental to study this kind of multiple ion aerosol mixtures: in this section we will focus on the analysis of hygroscopic behavior of  $\text{NaCl}/(\text{NH}_4)_2\text{SO}_4$  mixture.

### 4.2.1 Experimental results

To test the ZSR on an aerosol made of more than 3 ions, we generated aerosol particles composed of  $NaCl$  and  $(NH_4)_2SO_4$  aerosols. Figure 4.7 represents the variation of the  $f(RH)$  with the relative humidity for pure  $(NH_4)_2SO_4$  (black curve), pure  $NaCl$  (gray curve) and for the mixture containing 36, 60, 77, 89% of  $NaCl$  (colored curves). Each curve represents values of the  $f(RH)$  derived from the measurements of the scattering coefficients at different RH. Each dot is a representation of the mean  $f(RH)$  averaged within a 10% window of RH ( $\approx 10$  values for  $RH < DRH$  and  $\approx 20$  values when the RH values approach to the DRH). At maximum RH values (i.e.  $RH > 80\%$ ),  $f(RH)$  values are about 15 and 4.5 for pure  $NaCl$  and  $(NH_4)_2SO_4$ , respectively. The variation of the maximum of  $f(RH)$ , related to the hygroscopic behavior of the aerosol mixture, can be observed as a function of  $NaCl$  molar fraction. The maximum  $f(RH)$  (at  $\approx 85\%$  RH) (Figure 4.7) is increasing with the increased molar fraction of  $NaCl$  in the mixture. The  $f(RH)_{max}$  increases from 4.5 for pure  $(NH_4)_2SO_4$  to 5.8 when adding  $NaCl$  at a molar fraction of 0.36 and it reaches 13.2 when the molar fraction of  $NaCl$  is 0.89.

Moreover, one can see that the absorption of water and the deliquescence of  $NaCl$  start at a lower RH than  $(NH_4)_2SO_4$ . In our experiments, the DRH are measured at  $75.6 \pm 1\%$  and at  $79.9 \pm 1\%$  for  $NaCl$  and  $(NH_4)_2SO_4$ , respectively (Laskina et al., 2015). The  $DRH_{mixture}$  for the different fractions of  $NaCl$  ( $X_{NaCl} = 0.36, 0.6, 0.77, 0.89$ ) are observed around  $56 \pm 3\%$ ,  $66 \pm 2.5\%$ ,  $75 \pm 3\%$ , and  $75.2 \pm 3\%$ , respectively. Once more, one can observe that  $DRH_{mixture}$  are lower than those of individual pure aerosol components, a feature which is consistent with previous results. The more the mixture is enriched in  $NaCl$ , the more  $DRH_{mixture}$  approaches the value of DRH of pure  $NaCl$ . This is not the case for  $(NH_4)_2SO_4$ . Consequently, our results show that even a small fraction of  $NaCl$  changes drastically the hygroscopic behavior of the mixture.

Figure 4.8 shows  $DRH_{mixture}$  for each  $NaCl$  fraction of the  $NaCl/(NH_4)_2SO_4$  mixing retrieved from measurements of Figure 4.7. The general tendency highlights a “V” shape with

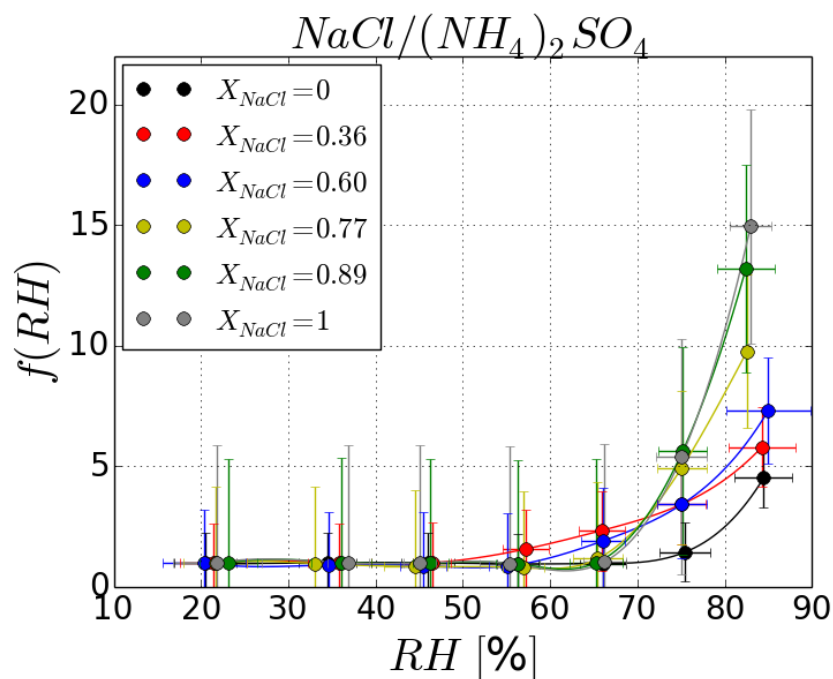


**Figure 4.7:** Variation of the measured scattering enhancement factor as a function of the relative humidity for  $\text{NaCl}/(\text{NH}_4)_2\text{SO}_4$  mixture containing 0 (black), 36 (red), 60 (blue), 77 (yellow), 89 (green), 100% (grey) of  $\text{NaCl}$ .

a minimum  $\text{DRH}_{\text{mixture}}$  (56%) for a fraction of  $\text{NaCl}$  equal to 0.36. The  $\text{DRH}_{\text{mixture}}$  is then increasing above the 0.36 fraction until it reaches a plateau at 75% for  $X_{\text{NaCl}}=0.77$ .

Rood et al. (1985) have shown the deliquescence diagram of an internal mixture of  $(\text{NH}_4)_2\text{SO}_4/\text{Na}_2\text{SO}_4$  having  $\text{SO}_4^{2-}$  in common but composed of more than 3 ions ( $2\text{NH}_4^+$ ,  $\text{SO}_4^{2-}$  and  $2\text{Na}^+$ ) (Figure 4.8) using a similar experimental setup as the one used in this study (red curve). Their results represent the  $\text{DRH}_{\text{mixture}}$  value measured for a specific molar ratio of  $\text{Na}^+/\text{SO}_4^{2-}$ . In order to calculate the values of  $X_{\text{Na}^+}$  the value of the molar ratio ( $\text{Na}^+/\text{SO}_4^{2-}$ ) have been divided by  $(1+\text{Na}^+/\text{SO}_4^{2-})$  and thus each dot represents the  $\text{DRH}_{\text{mixture}}$  for a specific molar fraction of  $\text{Na}^+$  in the mixture. For  $X_{\text{Na}^+}=0.28$  the  $\text{DRH}_{\text{mixture}}$  of  $(\text{NH}_4)_2\text{SO}_4/\text{Na}_2\text{SO}_4$  mixture is equal to  $71\pm 1\%$ , for  $X_{\text{Na}^+}=0.4$  the  $\text{DRH}_{\text{mixture}}$  decreases to  $67\pm 1.5\%$ . This value is much lower ( $\approx 15\%$ ) than the  $\text{DRH}$  of

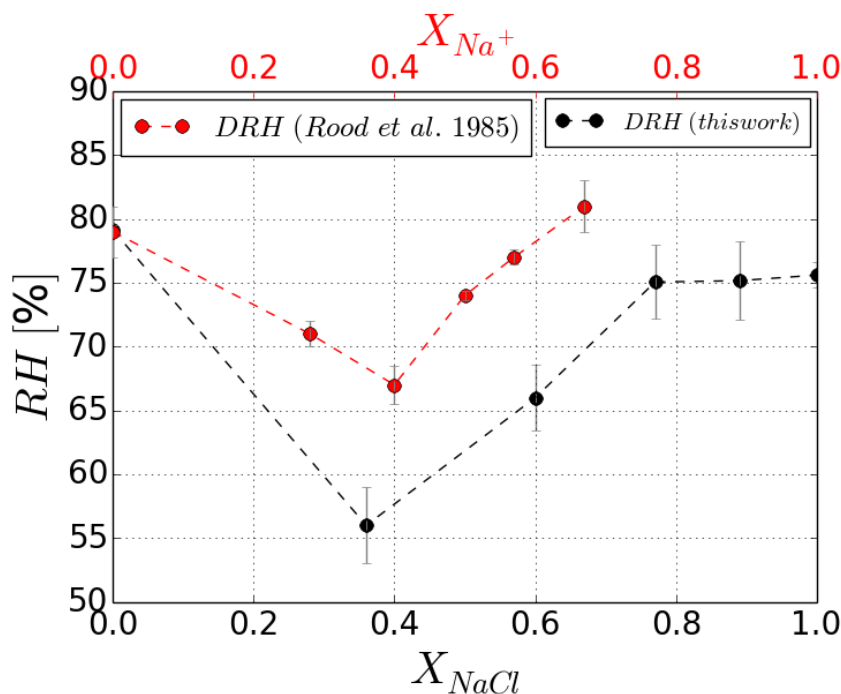


**Figure 4.8:**  $DRH_{mixture}$  variation of  $NaCl/(NH_4)_2SO_4$  with the different molar fractions of  $NaCl$  obtained during this study (black curve) and  $DRH_{mixture}$  variation of  $(NH_4)_2SO_4/Na_2SO_4$  molar fractions of  $Na^+$  obtained by Rood et al. (1985) (red curve).

pure  $Na_2SO_4$  (81%) or  $(NH_4)_2SO_4$  (79%).

Similarly to our results, Figure 4.8 illustrates that the  $DRH_{mixture}$  increases to higher values for  $X_{Na^+} > 0.4$ . Since the mixture of  $(NH_4)_2SO_4/Na_2SO_4$  obtained by Rood et al. (1985) is not the same mixture as the one studied in this thesis, we only compare the general behavior of the curve, without direct comparison of the  $DRH_{mixture}$  values at each molar fraction. Indeed, for these two mixtures  $(NH_4)_2SO_4/Na_2SO_4$  and  $NaCl/(NH_4)_2SO_4$  the DRH values are depending on the fraction of each pure compound.

## 4.2.2 Comparison to the ZSR

Again the ZSR method is used for mixed aerosols and for different molar fractions using the  $g(RH)$  of pure aerosols as inputs. Therefore,  $g(RH)_{ZSR}$  is unique for each molar fraction of aerosol mixing. However,  $g(RH)_{ZSR}$  is then depending slightly on compound fractions and

more largely on pure aerosol properties. Consequently,  $f(\text{RH})$  measurements (Figure 4.7) and, therefore,  $g(\text{RH})$  deduced from the  $f(\text{RH})$  are evolving differently as function of molar fraction. Indeed,  $g(\text{RH})$  values tend to coincide with  $g(\text{RH})$  of pure  $\text{NaCl}$  when the molar fraction of this latter is significantly increased.

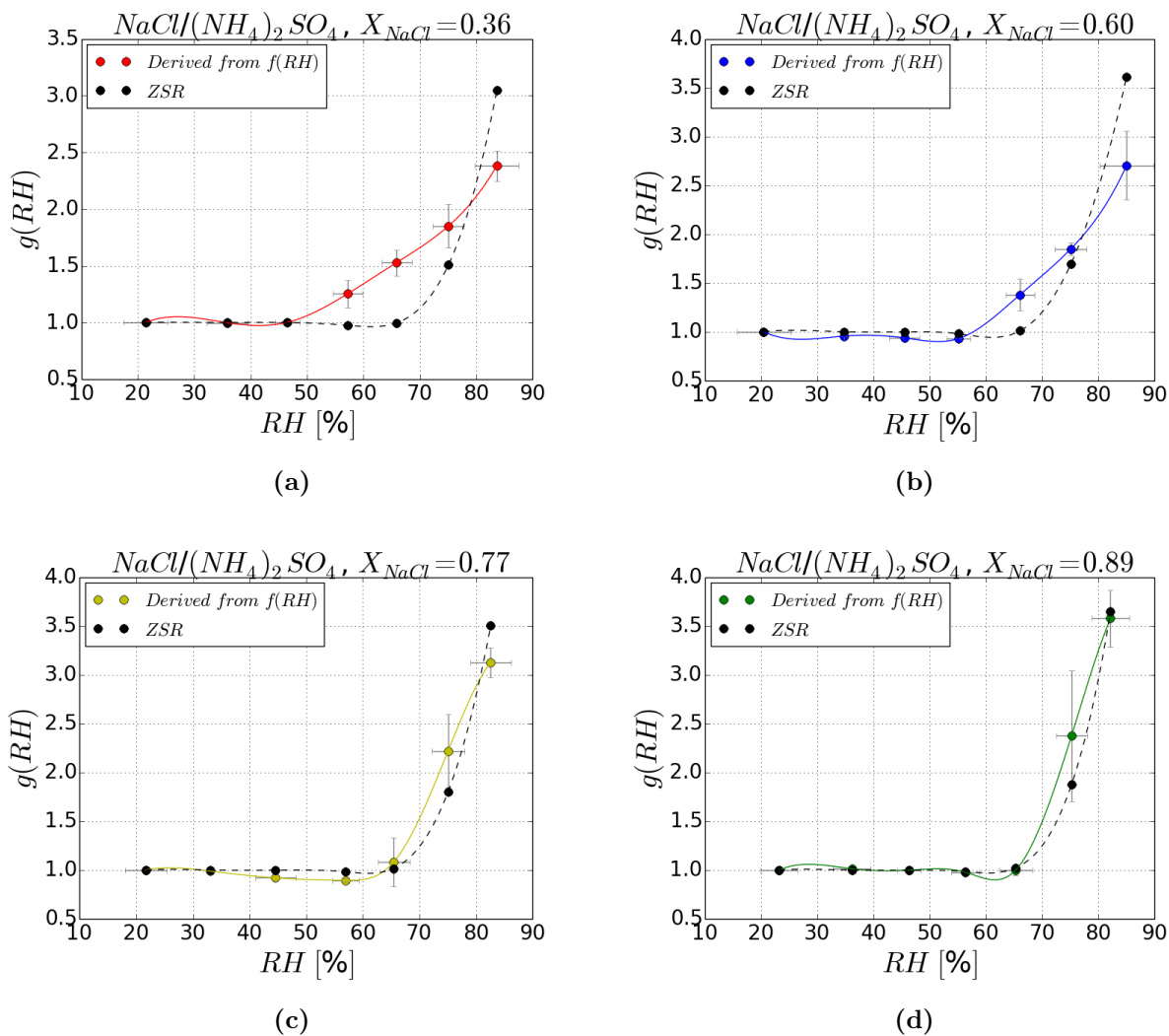


**Figure 4.9:** Comparison of the growth factor retrieved from optical measurements (scattering enhancement factor) (colored curves) and predicted using the ZSR method (black curves) for 36 (a), 60 (b), 77 (c), 89 (d) % of  $\text{NaCl}$  in  $\text{NaCl}/(\text{NH}_4)_2\text{SO}_4$  mixture.

Figure 4.9 presents the comparison of  $g(\text{RH})_{\text{ZSR}}$  (black dashed curve) with  $g(\text{RH})$  deduced from  $f(\text{RH})$  measurements for different molar fractions of  $\text{NaCl}$  in the  $\text{NaCl}/(\text{NH}_4)_2\text{SO}_4$  mixture (colored curves). Again, each dot corresponds to an average value of  $g(\text{RH})$  within a 10% window of RH. The general tendency of the evolution of both measured and ZSR computed  $g(\text{RH})$  with the RH are relatively similar, except for the two lower fractions of  $\text{NaCl}$  ( $X_{\text{NaCl}} < 0.77$ ). In Figure 4.9a,  $g(\text{RH})_{\text{ZSR}}$  for  $X_{\text{NaCl}} = 0.36$  underestimates  $g(\text{RH})$  retrieved from the measurements by 24% at RH=57%, by 41% at RH=66%, and by 9% at RH=75%. At the highest humidity value (RH > 84%), the  $g(\text{RH})_{\text{ZSR}}$  is overestimated by 40% in comparison to the measurement retrievals. Similarly, for  $X_{\text{NaCl}} = 0.6$  (Figure 4.9b),  $g(\text{RH})_{\text{ZSR}}$  underestimates  $g(\text{RH})$  retrievals from measurements before the DRH is reached. It underestimates up to 32% at RH=66% and by only 9% at RH=75%. At RH larger than the DRH (RH=85%), ZSR calculations overestimate by 29%  $g(\text{RH})$  values.

For the two other molar fractions, associated with larger contributions of  $\text{NaCl}$  ( $X_{\text{NaCl}} = 0.77$  and 0.89), the differences between  $g(\text{RH})$  computed from ZSR method and the measurements are lowered (Figure 4.9c and 4.9d), as the quantity of  $\text{NaCl}$  in the mixture dominates  $(\text{NH}_4)_2\text{SO}_4$ . Indeed,  $\text{DRH}_{\text{mixture}}$  for these  $\text{NaCl}$  fractions is observed at 75%, really close to the DRH of pure  $\text{NaCl}$ . This result is consistent previous results shown for the 3 ions mixing cases ( $\text{NaCl}/\text{KCl}$  as well as  $\text{NaCl}/\text{NaNO}_3$ ).

In this section, our results have highlighted that the ZSR theory deviates with aerosol measurements for the hygroscopic growth of  $\text{NaCl}/(\text{NH}_4)_2\text{SO}_4$ , a result which is consistent with those previously reported by Svenningsson et al. (2006). Indeed, these authors have shown that the ZSR overestimates their measurements for the mixture containing  $\text{NaCl}$ ,  $(\text{NH}_4)_2\text{SO}_4$ , succinic acid and fulvic acid, using the HTDMA system, for particles with dry diameter of 86 nm.

### 4.3 Conclusion

In this chapter, the experimental setup based on the measurements of the scattering coefficient by nephelometry was used to study optical properties of aerosol binary mixtures as a function of RH, and to assess their hygroscopic growth. In this study, we have defined the only phase transition we observe as the DRH of the mixture, although it is necessary to improve this method in order to refine the results and identify the second DRH of the mixture.

The overall hygroscopicity of internally-mixed particles initially made up of two compounds is altered by the molar fraction of each compound in the mixture. Previous studies have shown properties of binary mixtures of compounds having a common ion (e.g.  $Na^+$  in  $NaCl/NaNO_3$  mixture,  $Cl^-$  in  $NaCl/KCl$  mixture). In our study, we analyse the case of binary mixtures of compounds with common ion ( $Cl^-$  in  $NaCl/KCl$  mixture,  $Na^+$  in  $NaCl/NaNO_3$  mixture) and with no common ion ( $NaCl$  and  $(NH_4)_2SO_4$ ). For aerosol mixtures of 3 and more than 3 ions, our results highlight that the ZSR method deviates from the experimental observations, especially when  $DRH_{mixture}$  is much lower than both pure aerosol DRH. Thus, it seems that a preliminary good estimate of the  $DRH_{mixture}$  is mandatory in order to properly use the ZSR parameterisation. It would therefore be applied only to cases showing low difference between  $DRH_{mixture}$  and one of the pure aerosol DRH. Many thermodynamic models, such as E-AIM and ISORROPIA-II could be used to determine the MDRH as well as the DRH. However, the question remains whether it is possible to apply these models to real atmospheric aerosols. In order to answer this question, we will study in the next chapter the evolution of a single particle made of  $NaCl$  and  $(NH_4)_2SO_4$  with the relative humidity. This analysis could help to better understand processes occurring during the humidifying process at the particle scale.



---

---

## CHAPTER 5

---

Hygroscopic behavior of internally mixed single  
particles of  $\text{NaCl}/(\text{NH}_4)_2\text{SO}_4$

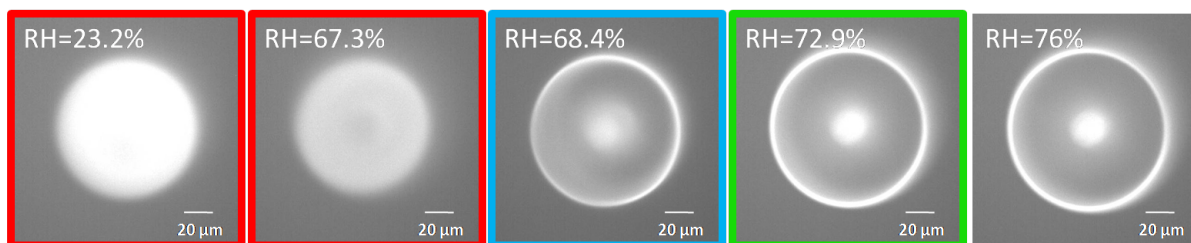
Chapter 4 has highlighted some limitations of the ZSR parameterization, especially when  $DRH_{mixture}$  is much lower than one of the pure compound DRH. This chapter is dedicated to a better understanding of MDRH and DRH evolution during a humidifying process of synthetic multi-component single particles, using levitation technique and optical microscopy. E-AIM model is used in order to calculate MDRH and DRH for  $NaCl/(NH_4)_2SO_4$  mixture that corresponds to the binary complex mixture studied in chapter 4. Raman microspectrometry is used to determine the particle chemical composition as well as the phase of all species at different RH. Previous studies reporting about the deliquescence of particles composed of ammonium sulfate by the coupling of levitation technique and Raman spectroscopy are scarce. They include two studies of ammonium sulfate as a single component (Ishizaka et al., 2013, 2014) and a study of phase transformation in ammonium nitrate/ammonium sulfate mixed particles (Lee et al., 2008), which is a binary inorganic mixture with only one ion in common,  $NH_4^+$ . Additionally, a study of the deliquescence behavior of  $NaNO_3/NaNO_2$  with one ion in common,  $Na^+$ , has been performed recently (Seng et al., 2018a), as well as a study of the deliquescence behaviour of aerosols composed of ammonium sulfate internally mixed with malonic acid, maleic acid, and glutaric acid (Treuel et al., 2009). Other investigations focusing on hygroscopic properties of mixed  $(NH_4)_2SO_4$ /glutaric acid microdroplets (Jordanov and Zellner, 2006) and a study of the phase transition from the liquid to the solid state of ammonium sulfate/glycerol mixture (Trunk et al., 1997) can be mentioned. In addition, Yeung et al. (2009) studied the phase transition and hygroscopicity of particles of a mixture of ammonium sulfate and adipic acid mixture. Zhou et al. (2014) investigated mixed phthalic acid/ammonium sulfate droplets at various relative humidities by confocal Raman spectroscopy. Laskina et al. (2015), studied the hygroscopic growth of multicomponent aerosol particles including ammonium sulfate mixed with adipic and succinic acids. However, these last three studies were conducted on particles deposited on a hydrophobic substrate, not on levitated particles. Furthermore, most of these studies report on the internal mixing of ammonium sulfate with organic species. To our best knowledge, the deliquescence of  $NaCl/(NH_4)_2SO_4$  mixture composed of four different inorganic ions ( $Na^+$ ,  $Cl^-$ ,  $NH_4^+$  and  $SO_4^{2-}$ ) has never been investigated using levitation technique coupled

to Raman microspectrometry.

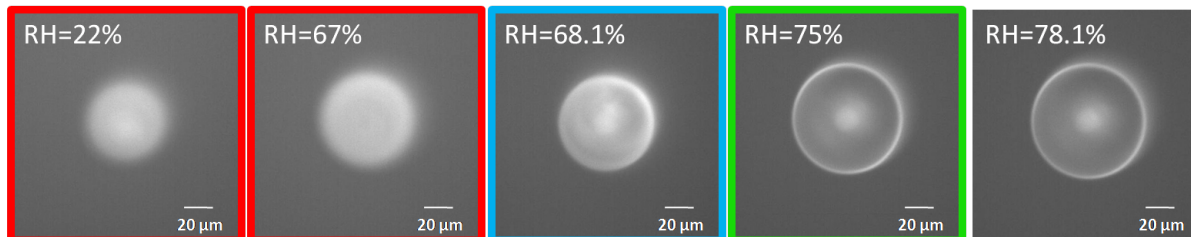
## 5.1 Phase transitions and growth factors analysis

Using a medical nebulizer, internally-mixed particles of  $NaCl/(NH_4)_2SO_4$  were generated. One particle was acoustically trapped in an environmental cell equipped with a RH sensor and observed using an optical microscope. Figures 5.1a, 5.1b, 5.1c, and 5.1d show the effect of the relative humidity on single levitated particles of  $NaCl/(NH_4)_2SO_4$  for different  $NaCl$  molar fractions ( $X_{NaCl} = 0.36, 0.60, 0.77$  and  $0.89$ , similar to those presented in chapter 4) ranging from  $20 \mu\text{m}$  to  $80 \mu\text{m}$  of dry diameter. Optical images with red borders represent dried particles, the ones with light blue borders represent the particle at the MDRH point (first DRH) and the ones with green borders represent the particle at the DRH point (second DRH). A thin film of water, evidenced by a white external layer on optical images of the particles, appears when the RH reaches the MDRH. These images show that the particles with an initial irregular or spheroid morphology below the MDRH point change to spherical shaped particles at MDRH.

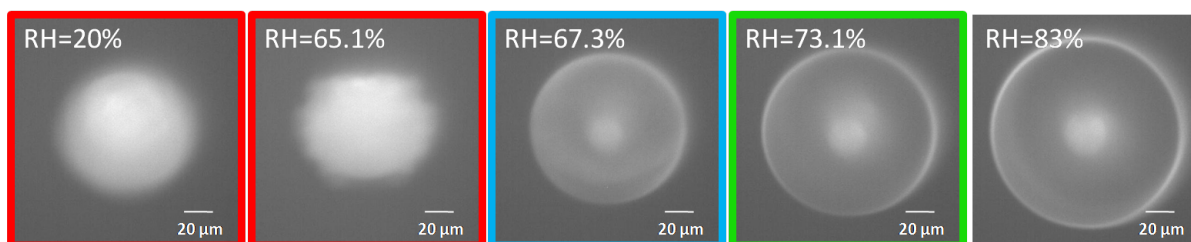
For  $X_{NaCl} = 0.36$  (Figure 5.1a, Table 5.1), the particle diameter remains constant up to a relative humidity of 68.4%. At this value, the size of the particle increases of about 12% in comparison to the size of the dried particle. This value is defined as the MDRH. A 10% size increase is observed at RH of 72.9% in comparison to the particle diameter observed at RH=68.4%. This second RH value is defined as the DRH point. For  $X_{NaCl} = 0.60$  (Figure 5.1b, Table 5.1), the dried particle diameter remains constant until the relative humidity reaches a value of 68.1%. This value corresponds to the MDRH when the particle diameter increases by 15%. The DRH (RH=75%) is associated with a 16% size increase. The MDRH for  $X_{NaCl} = 0.77$  (Figure 5.1c, Table 5.1) is equal to 67.3% and associated to a particle diameter that increases by 32%. Furthermore, the second sudden increase in the particle diameter of about 23%, in comparison with the value at RH=67.3%, is observed at 73.1% RH. For  $X_{NaCl} = 0.89$  (Figure 5.1d, Table 5.1), a decrease of about 14% in size is shown



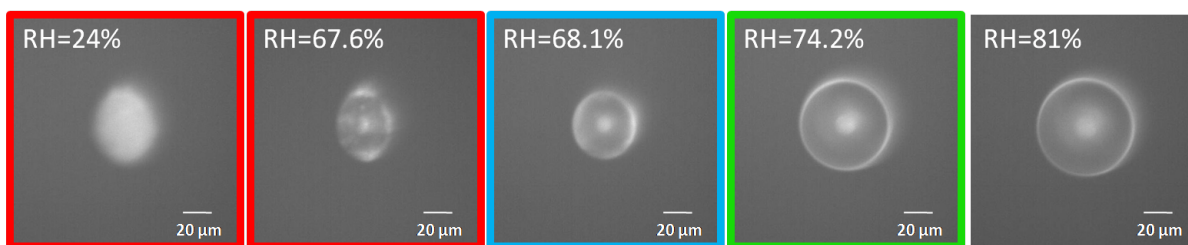
(a)



(b)



(c)



(d)

**Figure 5.1:** *Optical images of  $\text{NaCl}/(\text{NH}_4)_2\text{SO}_4$  particle levitated in air during the humidifying process for  $X_{\text{NaCl}}=0.36$  (a),  $X_{\text{NaCl}}=0.60$  (b),  $X_{\text{NaCl}}=0.77$  (c) and  $X_{\text{NaCl}}=0.89$  (d). The images with red, blue and green borders represent the dried particle, the particle at the MDRH and at the DRH, respectively.*

at RH=67.6%. This decrease is due to water absorption on the lattice defects in the dried crystalline  $NaCl$  that produces a structural rearrangement inside the solid particle (Gupta et al., 2015). At 74.2% RH, the particle diameter drastically increases by 97% in comparison to the size at the MDRH.

To summarize these analysis, the higher molar fractions of  $NaCl$  (higher proportion of hygroscopic  $NaCl$  in the mixture) are associated to the higher relative size increases between the dried particle and the particle size at the MDRH. Similarly, the higher molar fractions of  $NaCl$  correspond to higher relative size increases between the particle size at the MDRH and the one at the DRH. Table 5.1 summarizes the values of the MDRH and the DRH for all studied molar fractions of  $NaCl$ .

**Table 5.1:** *MDRH and DRH values for  $NaCl/(NH_4)_2SO_4$  mixture obtained from the humidograms based on the optical images.*

$X_{NaCl}$	0	0.1	0.2	0.36	0.5	0.6	0.77	0.89	1
MDRH(%)	-	69	68.2	68.4	67.6	67.5	67.3	68.1	-
DRH(%)	79.2	78.5	74	72.9	75.2	75	73.1	74.2	75.7

By plotting the humidogram of the variation of the growth factor ( $g(RH)$ ) as a function of RH, one can clearly observe the two phase transitions that occur for each molar fraction for  $NaCl/(NH_4)_2SO_4$  mixture. Figure 5.2 represents the obtained humidograms relying on size measurements from optical images. The gray and the black curves represent  $g(RH)$  of pure  $NaCl$  and  $(NH_4)_2SO_4$ , respectively. The colored curves represent  $g(RH)$  of the different fractions of NaCl in the aerosol mixture. These results show that MDRH of the mixtures systematically occur at an RH values lower than the DRH of pure  $NaCl$  and  $(NH_4)_2SO_4$ . Moreover, DRH of the mixtures are lower than DRH of pure  $(NH_4)_2SO_4$ . The  $g(RH)$  values we have determined at DRH are equal to 1.24, 1.68, 1.63, and 1.81 for  $X_{NaCl} = 0.36, 0.6, 0.77,$  and  $0.89,$  respectively.

The value of the MDRH for all the molar fractions of  $NaCl$  investigated in this analysis

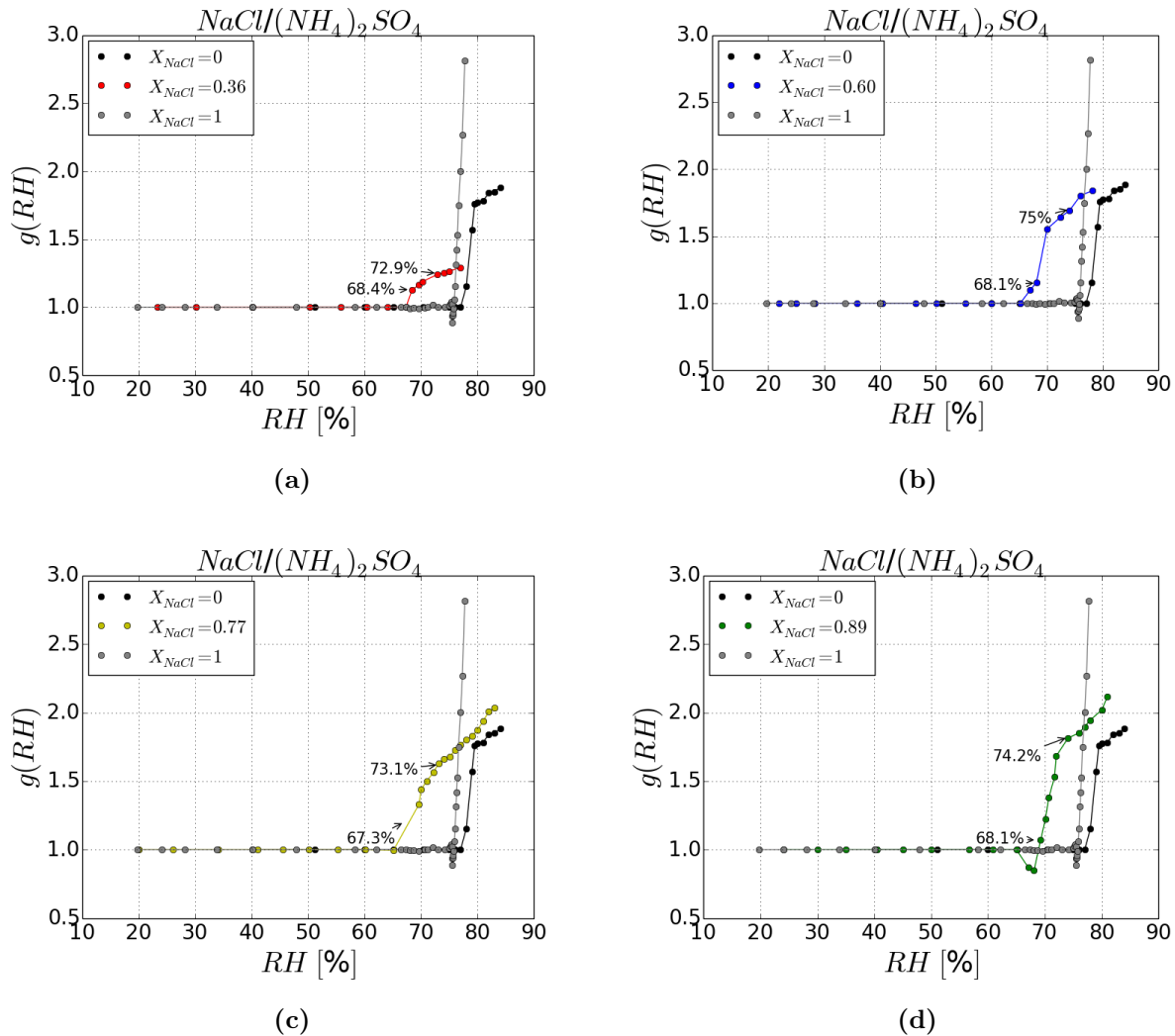


**Figure 5.2:** Variation of the growth factor measured from the images of the optical microscope with the relative humidity for 36 (a), 60 (b), 77 (c), 89 (d) % of NaCl in  $\text{NaCl}/(\text{NH}_4)_2\text{SO}_4$  mixture (colored curves) in comparison to pure aerosols (NaCl: grey,  $(\text{NH}_4)_2\text{SO}_4$ : black).

varies slightly between 67.3% and 69% ( $\pm 0.9\%$ ). Theoretically, for a binary mixture MDRH value is expected to be constant. However, this is true for binary systems with no ion or solely one ion in common (such as  $\text{NaCl}/\text{NaNO}_3$  mixture studied in Seng (2017)). In the present case, the MDRH variation could be due to the complexity of the system containing

4 different inorganic ions ( $Na^+$ ,  $Cl^-$ ,  $NH_4^+$  and  $SO_4^{2-}$ ), that may combine differently as a function of RH, producing an inhomogeneous distribution of chemical species in the volume of the particle. As expected DRH values change as a function of the molar fraction of  $NaCl$  in the aerosol mixture. As an example, the DRH is 78.5% (close to the DRH value for pure  $(NH_4)_2SO_4$ ) for a particle with  $X_{NaCl} = 0.1$ , although it reaches 74.2% for a particle with  $X_{NaCl} = 0.89$  (close to the DRH value for pure  $NaCl$ ). Nevertheless, the DRH variation does not follow the usual trend of the phase diagram of binary systems described in chapter 1, i.e a DRH decrease for molar fractions lower than the eutonic point, and a DRH increase for molar fractions greater than the eutonic point.

## 5.2 Comparison of experimental results with E-AIM model

### Deliquescence phase diagram

The predicted values of the MDRH and the DRH of  $NaCl/(NH_4)_2SO_4$  mixtures with different molar fractions of  $NaCl$  have been calculated using the thermodynamic model E-AIM (Clegg et al., 1998). By forcing the model to prevent the formation of new solids (like  $NH_4Cl$ ,  $Na_2SO_4 \dots$ ) while mixing  $Na^+$ ,  $Cl^-$  and  $NH_4^+$  and  $SO_4^{2-}$ , we obtain the diagram presented Figure 5.3. The red and the black curves in this figure represent DRH and MDRH, respectively, values predicted using E-AIM model calculation. The eutonic point appears when the molar fraction of  $NaCl$  in the aerosol mixture is equal to 0.55; for this molar fraction only one phase transition is observed. The red and the black dots in this figure represent respectively DRH and the MDRH derived from experimental analysis. The comparison of calculated values with the experimental values deduced from the optical images (table 5.1) shows a disagreement with E-AIM calculations for the MDRH values and most of the DRH values. The MDRH calculated using the E-AIM model is 59.55%, whereas it varies between 67.3 and 69% in experimental observations. Moreover, the DRH in the model varies between 59.55% and 80.3% whereas it is always higher than 72% in the experimental

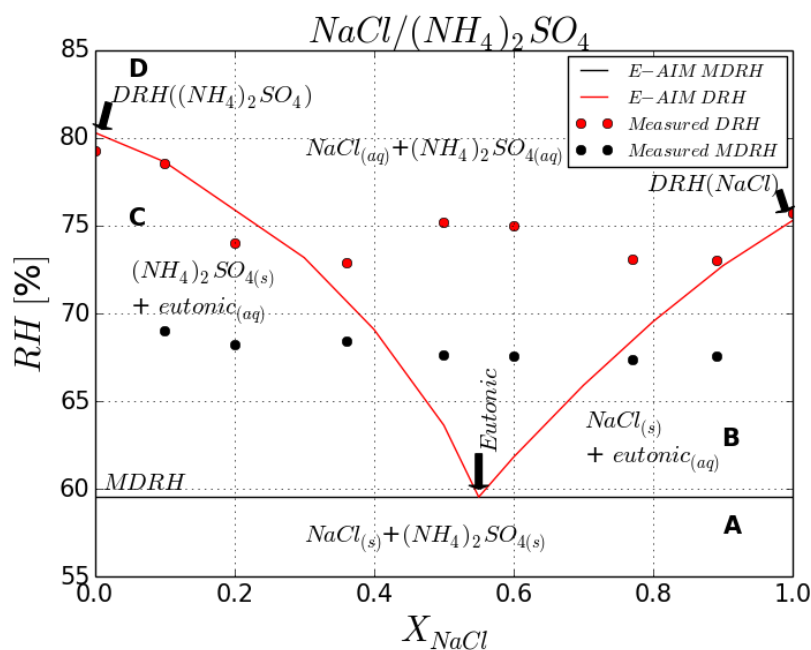


**Figure 5.3:** Evolution of the MDRH (black) and the DRH (red) as a function of the NaCl fraction in the  $\text{NaCl}/(\text{NH}_4)_2\text{SO}_4$  mixture. The lines correspond to simulation results (E-AIM) while forcing it to prevent the formation of new solids. Dots correspond to the experimental results. A, B, C and D correspond to the four main regimes (see text for more details).

observations. The variability is not the same depending on the molar fraction of  $\text{NaCl}$ . The most striking point is the eutonic point. For instance, the eutonic point that is predicted at  $X_{\text{NaCl}} = 0.55$  in E-AIM calculation and corresponding to the minimum of the DRH values was not evidenced in the experimental method using the optical images.

As previously explained in chapter 1 and shown Figure 5.3, four main separate areas associated to the physical state of the mixture can be distinguished:

A-  $\text{NaCl}$  and  $(\text{NH}_4)_2\text{SO}_4$  are both mixed in the solid state for RH values below the MDRH and for all the molar fractions of  $\text{NaCl}$ .

B- Solid  $\text{NaCl}$  is in equilibrium with an aqueous phase having the eutonic composition,

between the MDRH and the 2<sup>nd</sup> DRH, for  $X_{NaCl}$  greater than 0.55.

C- Solid  $(NH_4)_2SO_4$  is in equilibrium with an aqueous phase having the eutonic composition, between the MDRH and the 2<sup>nd</sup> DRH, for  $X_{NaCl}$  less than 0.55.

D-  $NaCl$  and  $(NH_4)_2SO_4$  are both mixed in aqueous phase for RH higher than the 2<sup>nd</sup> DRH and for all the molar fractions of  $NaCl$ .

These results highlight that this solid/aqueous species partitioning as a function of RH and  $X_{NaCl}$  predicted by E-AIM with the prevention of the formation of new species in the model is not in accordance with the aerosol mixture hygroscopic behavior observed experimentally in our analysis.

Further calculations have been performed using the same thermodynamic model (E-AIM) in a second configuration, i.e., without forcing it to prevent the formation of new species. This second simulation allows to obtain the diagram presented in Figure 5.4 is obtained. The formation of new species leads to a more complex system, i.e. evolution from a binary system to a quaternary or an even higher multicomponent system. Similarly to Figure 5.3, the red and the black curves represent the values of DRH and MDRH respectively calculated using E-AIM. Red and black dots are respectively the values of DRH and MDRH measured experimentally from the optical images. The figure shows entirely different features compared to the previous one. A better agreement between the predicted and measured DRH and MDRH is clearly shown in Figure 5.4.

Especially, MDRH computed by the E-AIM model are in much better agreement with those observed from optical images, with a value approximately equal to 68%. Only small discrepancies appear between the observations of the experiment and the model. E-AIM calculation predicts a MDRH shift to lower values, i.e. from 69% RH to 67% RH, in two steps placed between  $X_{NaCl} = 0.55$  and 0.65, which is in agreement with experimental values of MDRH varying between 69% and 67.3%. When the formation of new species is allowed in E-AIM calculations, an eutonic point is no longer predicted for  $NaCl/(NH_4)_2SO_4$  mixture. Furthermore, three minimum values of DRH are shown at  $X_{NaCl} = 0.27$ , 0.70 and 0.85. Our

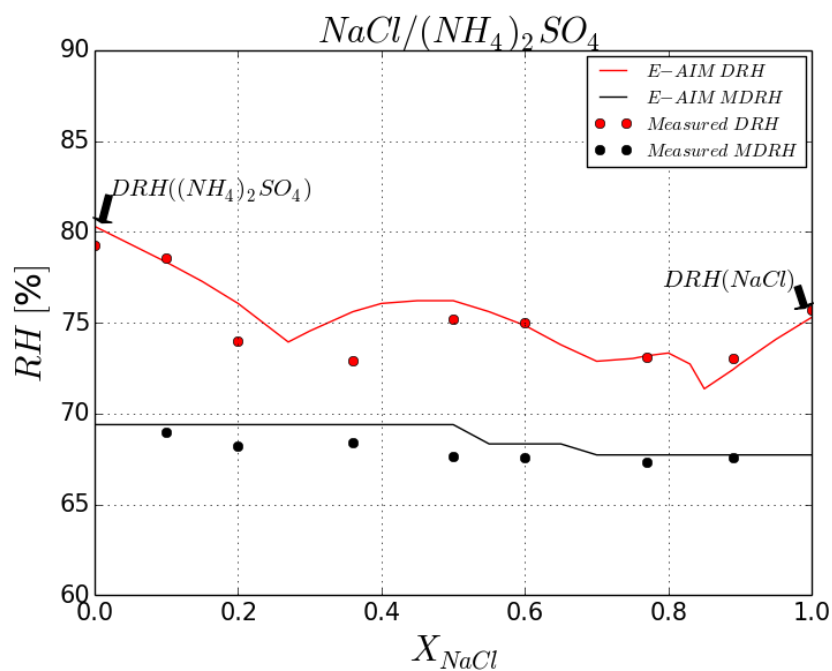


**Figure 5.4:** Evolution of the MDRH (black) and the DRH (red) as a function of the NaCl fraction in the  $NaCl/(NH_4)_2SO_4$  mixture. The lines correspond to simulation results (E-AIM) without forcing it to prevent the formation of new solids. Dots correspond to the experimental results. A, B, C and D correspond to the four main regimes (see text for more details).

experimental analysis shows a variation of DRH, which is compatible with this behavior.

## 5.3 Aerosol composition modifications

### 5.3.1 Analysis with Raman microspectrometry

To better understand MDRH and DRH variations with the molar fraction of  $NaCl$ , Raman microspectrometry has been used to investigate the chemical composition evolution of mixed aerosols during the humidification process. Raman spectra of levitated particles were acquired at different RH and for different molar fractions of  $NaCl$ . Figures 5.5a and 5.5c present the Raman spectra obtained for  $NaCl/(NH_4)_2SO_4$  with  $X_{NaCl} = 0.36$  at two different RH, 20% and 69%. Figure 5.5b and 5.5d represent the spectral range corresponding to the sulfate symmetric stretching mode. For  $X_{NaCl} = 0.36$  and at low RH (at RH=20% the particle is in a solid state), the Raman spectrum shows two main bands at 974 and 994  $cm^{-1}$  (Figure 5.5a). These bands are respectively identified as the symmetric stretching mode of  $SO_4^{2-}$  ion within solid  $(NH_4)_2SO_4$  (Dong et al., 2007) and solid  $Na_2SO_4$  (Nyquist et al., 1997). Another Raman band appears at 3049  $cm^{-1}$  corresponding to the stretching mode of  $NH_4^+$  ion within solid  $NH_4Cl$  compound (see Annex 2). These results give evidence of the formation of new species ( $Na_2SO_4$  and  $NH_4Cl$ , all in solid states) while mixing  $NaCl$  with  $(NH_4)_2SO_4$  in aqueous solution.

Figure 5.5c and Figure 5.5d show the Raman spectrum for the same aerosol mixture and for the same molar fraction but at higher humidity (RH=69%) corresponding to the MDRH point. At the MDRH, the symmetric stretching  $SO_4^{2-}$  band, corresponding to the solid sodium sulfate, disappears. However, the sulfate band at 979  $cm^{-1}$  corresponds to the  $SO_4^{2-}$  in aqueous solution and it combines the sulfates coming from both  $(NH_4)_2SO_4$  and  $Na_2SO_4$  salts in aqueous state. This is in agreement with the literature data that reports that the wavenumber of the symmetric stretching mode of sulfate ion within aqueous  $(NH_4)_2SO_4$  and  $Na_2SO_4$  varies only by 2  $cm^{-1}$  (Ben Mabrouk et al., 2013). The presence of the solid state  $NH_4Cl$  remains unchanged due to a higher deliquescence point (RH=77.3%) according to E-AIM calculations. The presence of water on the particle at the MDRH point is evidenced

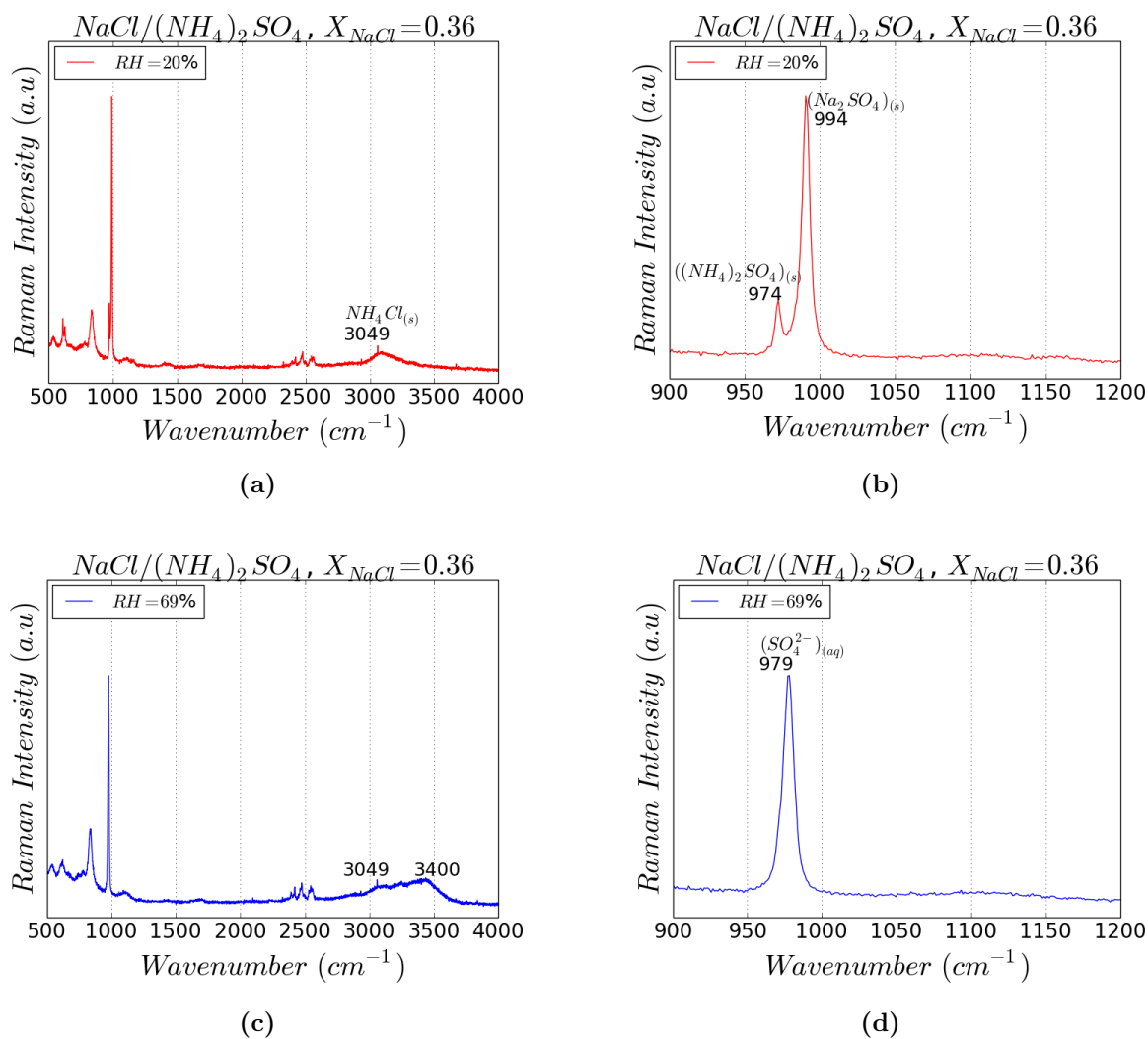


**Figure 5.5:** Raman spectra of a droplet initially containing 36% of  $\text{NaCl}$  and 64% of  $(\text{NH}_4)_2\text{SO}_4$  obtained with HeNe laser light at 633 nm at  $\text{RH}=20\%$  (a), and at  $\text{RH}=69\%$  (c). (b) and (d) represent enlarged views of 900-1200  $\text{cm}^{-1}$  spectral range of (a) and (c), respectively.

by the band of OH stretching mode, that appears at approximately 3400  $\text{cm}^{-1}$ . The same study has been achieved for the  $\text{NaCl}/(\text{NH}_4)_2\text{SO}_4$  at all the  $\text{NaCl}$  molar fractions of interest. As the results were similar for all fractions, we decided to only show one more fraction ( $X_{\text{NaCl}}=0.6$ ) in Figure 5.6. As in the previous case, Raman bands of  $(\text{NH}_4)_2\text{SO}_4$ ,  $\text{Na}_2\text{SO}_4$

and  $NH_4Cl$  in a solid states appear respectively at  $974\text{ cm}^{-1}$ ,  $994\text{ cm}^{-1}$  and  $3049\text{ cm}^{-1}$  at  $RH=20\%$ . While at humidity slightly higher than the MDRH ( $RH=70\%$ , Figure 5.6c), the band at  $979\text{ cm}^{-1}$  shows a transformation of solid  $(NH_4)_2SO_4$  into aqueous  $2NH_4^+ + SO_4^{2-}$ . Depending on the relative humidity, the mixing state of individual particles can get very complex, with chemical species that can coexist in different physical states, i.e. well-mixed liquid state, or liquid and crystalline phase-separated state. Furthermore, the distribution of species was inhomogeneous in the volume of individual multi-component particles (i.e. Raman spectra acquired at different locations on the surface of the particle were characteristic of different species). When cycles of  $RH$  were conducted on the same single particle, the spatial distribution of species within the particle was highly variable.

These results highlight that new species ( $Na_2SO_4$  and  $NH_4Cl$ ) are formed when mixing  $NaCl$  with  $(NH_4)_2SO_4$ , that evolves from a solid state to an aqueous state when the  $RH$  increases and reaches the MDRH. Therefore, to fully understand the behavior of the  $NaCl/(NH_4)_2SO_4$  mixture with humidity (Figure 5.4), one need to understand the evolution of the DRH and MDRH for all the mixing of  $NaCl/Na_2SO_4$ ,  $NaCl/NH_4Cl$ ,  $(NH_4)_2SO_4/Na_2SO_4$  and  $(NH_4)_2SO_4/NH_4Cl$ . Therefore, further calculations have been performed using E-AIM model.

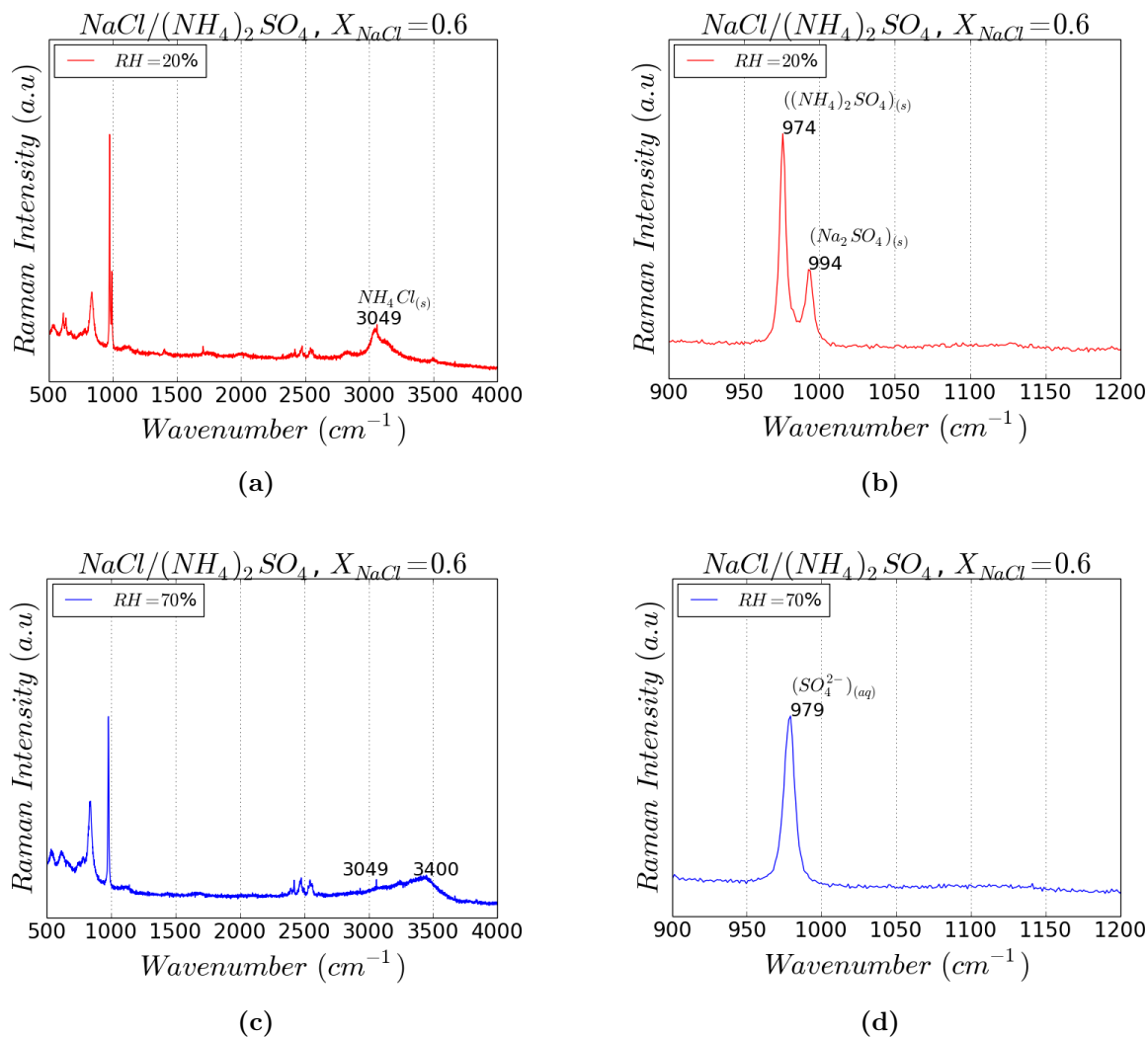


**Figure 5.6:** Raman spectra of a droplet initially containing 60% of NaCl and 40% of  $(\text{NH}_4)_2\text{SO}_4$  obtained with HeNe laser light at 633 nm at  $\text{RH}=20\%$  (a), and at  $\text{RH}=70\%$  (c). (b) and (d) represent enlarged views of 900-1200  $\text{cm}^{-1}$  spectral range of (a) and (c), respectively.

### 5.3.2 E-AIM calculation of MDRH and DRH

MDRH and DRH calculations, as a function of the RH, performed with E-AIM for  $\text{NaCl}/\text{Na}_2\text{SO}_4$ ,  $\text{NaCl}/\text{NH}_4\text{Cl}$ ,  $(\text{NH}_4)_2\text{SO}_4/\text{Na}_2\text{SO}_4$  and  $(\text{NH}_4)_2\text{SO}_4/\text{NH}_4\text{Cl}$  mixtures are shown in Figure 5.7. The general behavior of these different aerosol mixtures corresponds to the diagram ex-

plained in chapter 1 section 1.4.1.2. Especially, Figure 5.7 highlights that MDRH is always lower than DRH of the pure compounds of the aerosol mixture. In a solution of eutonic composition, the particle deliquesces like pure salt at MDRH. For all the inorganic salts mixtures considered here, the DRH of one salt is lowered by the addition of the second salt. When mixing two components having a difference of DRH between each pure component lower or equal to 10%, the MDRH value is always lower of at least 5% of the DRH of the pure component having the lowest DRH (Figure 5.7b, 5.7c, 5.7d). When the DRH difference between pure components is greater than 10%, the MDRH value is close to the DRH of the pure component having the lowest DRH, with a difference lower than 2% (Figure 5.7a). This behavior implies that for aerosol mixtures containing a high hygroscopic component compared to the second component, the MDRH value of the mixture is close to the DRH of the highly hygroscopic aerosol component (i.e.  $NaCl$ , for the  $NaCl/Na_2SO_4$  mixture).

Interestingly, Figure 5.7 shows that there is only a maximum of 5% difference between MDRH values for all the mixtures considered here, regardless of the hygroscopicity of each component included within the mixing. Indeed, MDRH values are predicted equal to 74.55%, 69.55%, 71.82%, and 72.27% for  $NaCl/Na_2SO_4$ ,  $NaCl/NH_4Cl$ ,  $(NH_4)_2SO_4/Na_2SO_4$ , and  $(NH_4)_2SO_4/NH_4Cl$  mixtures, respectively.

However, Figure 5.7 illustrates that each specific mixture shows an eutonic point at very different  $NaCl$  or  $(NH_4)_2SO_4$  molar fractions. For  $NaCl/Na_2SO_4$  mixture, the eutonic point corresponds to a molar fraction of  $NaCl$  equal to 0.9 (Figure 5.7a), whereas for  $NaCl/NH_4Cl$  it corresponds to a 0.5 molar fraction of  $NaCl$  (Figure 5.7b). For  $(NH_4)_2SO_4/Na_2SO_4$  and  $(NH_4)_2SO_4/NH_4Cl$ , the eutonic point appears when the molar fraction of  $(NH_4)_2SO_4$  is respectively equal to 0.7 (Figure 5.7c) and 0.4 (Figure 5.7d).

For the initial mixture considered in this particle analysis,  $NaCl/(NH_4)_2SO_4$ , both DRH minima appear at 0.27 and 0.85 molar fractions of  $NaCl$ , and the MDRH value shifts at 0.55 (Figure 5.4). These DRH minimum values are approximately equal to the eutonic points of some of the mixtures observed in Figure 5.7. For instance, for  $X_{NaCl} = 0.27$ , meaning that  $X_{(NH_4)_2SO_4} = 0.73$ , the DRH minimum of the  $NaCl/(NH_4)_2SO_4$  mixture could be re-

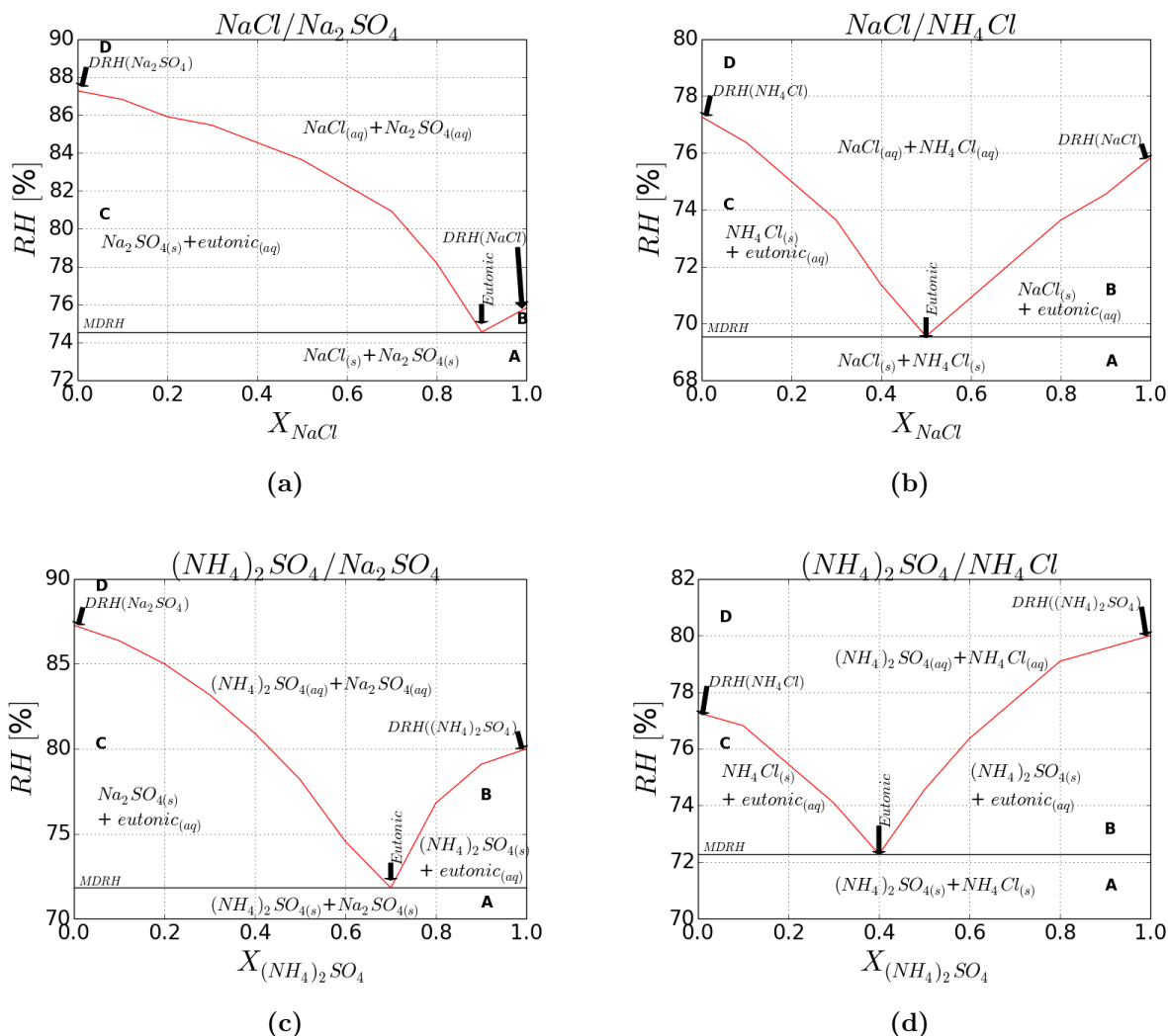


**Figure 5.7:** Evolution of the MDRH (black) and the DRH (red) as a function of the NaCl (a,b) and  $(NH_4)_2SO_4$  (c,d) fraction in  $NaCl/Na_2SO_4$  (a),  $NaCl/NH_4Cl$  (b)  $(NH_4)_2SO_4/Na_2SO_4$  (c) and  $(NH_4)_2SO_4/NH_4Cl$  (d) mixing. The lines correspond to simulation results (E-AIM) while forcing it to prevent the formation of new solids. A, B, C and D correspond to the four main regimes.

lated to the eutonic point that is observed when  $X_{(NH_4)_2SO_4} = 0.7$  in  $(NH_4)_2SO_4/Na_2SO_4$  mixture (Figure 5.7c). In addition, the second DRH minimum, observed for  $X_{NaCl} = 0.85$  in  $NaCl/(NH_4)_2SO_4$  mixture, may be associated to the eutonic point of  $NaCl/Na_2SO_4$

for  $X_{NaCl} = 0.9$  (Figure 5.7a). Finally, the MDRH small shift at  $X_{NaCl} = 0.55$ , for the  $NaCl/(NH_4)_2SO_4$  mixture, seems to coincide with the eutonic point at  $X_{NaCl} = 0.5$  for the  $NaCl/NH_4Cl$  mixture (Figure 5.7b). However, a full agreement between simple binary systems simulated by E-AIM and the experimental results is not possible. This confirms the complexity of the mixture, because it is not possible to know if the recombination reactions for each molar fraction are partial or total in the solid particle obtained by drying a droplet with an initial molar fraction of  $NaCl/(NH_4)_2SO_4$ . Thus, if a total recombination is assumed, at least three species would coexist in the particle, except for the stoichiometric fraction ( $X_{NaCl} = 2/3$ ), for which only two species would exist ( $NH_4Cl/Na_2SO_4$ ) because  $NaCl$  and  $(NH_4)_2SO_4$  would be completely consumed.

A deep study on the dried samples containing different molar fractions could be performed by Raman spectroscopy, to be able to determine the composition of each sample. A calibration curve and an internal standard would permit to determine quantitative composition in the samples, even if  $NaCl$  is not observed in Raman. However, this kind of study is out of the objectives of this work.

Overall, the complex shape of the observed and calculated (E-AIM) DRH and MDRH diagram of  $NaCl/(NH_4)_2SO_4$  mixture, represented in Figure 5.4, obtained during this thesis and the absence of an eutonic point (i.e. only one DRH transition for a specific molar fraction) are due to the presence of new species in the particle in a mixture made of more than 3 ions.

## 5.4 Discussion

During the atmospheric lifetime of aerosols, complex chemical reactions take place and give rise to the chemical and morphological heterogeneity within individual aerosol particles. In this chapter we have investigated the hygroscopic properties of single particles initially composed of two inorganic species with no common ion, i.e.  $NaCl$  and  $(NH_4)_2SO_4$ . We experimentally evidenced the formation of new species upon dehydration/hydration cycles in the binary mixture  $NaCl/(NH_4)_2SO_4$ , which modified the  $DRH_{mixture}$  evolution with

RH and therefore could be an additional reason for the non agreement of the ZSR with the experimental measurements. In addition, while working on a single particle, two phase transitions are shown (MDRH and DRH). Contrariwise, while measuring the optical properties of an aerosol population, only one phase transition has been evidenced (Chapter 4). For one molar fraction to another, the phase transition detected by nephelometry is close to the MDRH value or close to the DRH value obtained by optical microscopy. These results highlight that the ensemble of sub-micrometer sized particles do not take up water and/or do not scatter light in the experimental setup based on aerosol optical properties in the same way than a single super-micrometer sized particle takes up water in the levitation cell. It is unclear whether hygroscopic properties of the binary mixture of interest is size dependent. Indeed, two size ranges of multicomponent particles were measured: 300 nm submicron aerosol particles using nephelometry and 20-80  $\mu\text{m}$  supermicron particles using Raman microspectrometry. Previous studies on ammonium sulfate mixed with organic compounds reported phase separation in large particles upon decreasing the RH while smaller particles remained homogeneous at all RH (Veghte et al., 2013). Such different mixing states for large and small particles can result in different hygroscopic properties. For instance, Laskina et al. (2015) reported morphology-dependent hygroscopicity for organic/inorganic mixed particles. In the present study, we investigated a mixture of inorganic salts. Ge et al. (1998) explored the deliquescence behavior of particles generated from  $\text{NaCl}/\text{KCl}$ ,  $\text{NaCl}/\text{NaNO}_3$ , and  $(\text{NH}_4)_2\text{SO}_4/\text{NH}_4\text{NO}_3$  mixed solutions at different relative humidities using single-particle mass spectrometry and compared experimental observations with thermodynamic predictions of the deliquescence behavior of each mixture. While for  $\text{NaCl}/\text{KCl}$  and  $\text{NaCl}/\text{NaNO}_3$  mixtures, they found hygroscopic properties generally consistent with thermodynamic calculations, they observed a very complicated deliquescence behavior for  $(\text{NH}_4)_2\text{SO}_4/\text{NH}_4\text{NO}_3$  mixtures, that was generally not consistent with thermodynamic predictions.

In our case, the variations of MDRH and DRH of  $\text{NaCl}/(\text{NH}_4)_2\text{SO}_4$  mixtures obtained experimentally are roughly in accordance with E-AIM thermodynamic model. Especially, the general shape of the curve of the DRH variation as a function of  $\text{NaCl}$  molar fraction,

characterized by 3 local minima calculated with E-AIM, is in line with experimental observations. The study of aerosol particles containing the two mixed inorganic salts  $NaCl$  and  $(NH_4)_2SO_4$  shows that the system is already very complex to describe with the formation of new species as well as species present in variable physical states (liquid or solid) as a function of RH. One can assume that for real atmospheric aerosols, containing many different ions, the description of the MDRH and DRH as a function of RH would be also complex or even impossible.

In summary in the present work, we have demonstrated that the Raman microspectrometry technique is a powerful means to study the physical and chemical properties of aerosols, especially for in-situ observation of the deliquescence processes of single aerosol particles acoustically levitated in air. Nonetheless, the deliquescence behavior of  $NaCl/(NH_4)_2SO_4$  mixtures investigated here has been shown to be very complicated and the DRH variation as a function of the molar ratio was only roughly consistent with thermodynamic predictions. Further work is needed in order to better predict the complex mixing state of this aerosol particle type as a function of RH.



---

## Conclusions and perspectives

---

The knowledge about hygroscopic properties of aerosols is of primary importance for many atmospheric processes and environmental impacts, including chemical reactivity, particle wet and dry depositions, cloud droplet formation efficiency, optical properties, and relevant direct and indirect radiative effects. Due to the existence of several sources, either natural or related to human activities, a wide variety of aerosols (e.g. soil dust, black carbon, sea salt, insoluble organics, water soluble nitrates, sulfates) are present in the atmosphere. Aerosols are consistently modified during their residence time within the atmosphere due to coagulation with other particles, condensation of gases, heterogeneous chemical reactions or cloud processing. These modifications can lead to dramatic changes of the aerosol physical, chemical, and optical properties and therefore of their interactions with radiation. Moreover, within the sub-saturation regime of humidity conditions ( $0 < \text{RH} < 100\%$ ), the size of certain aerosol types can double due to the condensation of water vapor (Tang, 1996b). Such a size increase can therefore modify drastically their optical properties. According to Hess et al. (1998), a slight change of the relative humidity (+20%) may enhance the hygroscopic aerosol optical properties by a factor of 55% (OPAC, sea salt particles). Currently, several models are available to estimate the evolution of aerosol properties with RH, such as (i) Zdanovskii-Stokes-Robinson (ZSR, Zdanovskii (1948); Stokes and Robinson (1966)) parameterization, commonly used in aerosol simulations performed with general circulation models (GCM) and (ii) stand alone thermodynamic models, such as E-AIM and ISSOROPIA-II. The ZSR model is designed to estimate the particle growth due to water uptake and is generally used for aerosol radiative forcing studies in GCMs. The thermodynamic models are dedicated to retrieve Deliquescence Relative Humidity (DRH), as well as the quantity of condensed water on aerosol surface. Thus, they are commonly used for laboratory studies investigating the hygroscopic behavior of aerosols, especially phase transitions.

According to previous studies reported in literature, the ZSR mixing rule works fairly well for organic-organic and organic-inorganic aerosol mixtures (Chan and Chan, 2003; Zardini et al., 2008). However, it has been highlighted that there are large deviations of the ZSR compared to measurements for inorganic-inorganic mixtures including sea salt aerosols (Svenningsson et al., 2006). Due to sea salt specific hygroscopic properties and because of their high abun-

dance within the atmosphere, many studies have been devoted to better understand the discrepancies between calculations and observations of the evolution of the chemical, physical, and optical properties of mixtures including sea salt aerosols (Wise et al., 2007, 2009; Prather et al., 2013; Zieger et al., 2017). Despite these efforts, most of the differences that have been identified for these aerosol components between the calculated (ZSR, E-AIM) and the observed  $g(\text{RH})$  and DRH remain not fully understood.

The main goal of this thesis was to focus on aerosol mixtures containing sea salt in order to better understand (i) the evolution of their properties with RH and (ii) the discrepancies of the numerical methods used to estimate DRH and  $g(\text{RH})$  in comparison to experimental results. To do so, the physical and hygroscopic properties of synthetic aerosols have been studied in laboratory with two instrumental setups. The first one, based on the measurements of aerosol physical (optical particle counter) and optical (scattering coefficient) properties, enables to investigate a polydisperse aerosol population behavior as a function of RH. The second experimental setup, relying on measurements of aerosol physical and chemical properties by optical microscopy and Raman microspectrometry (Tobon et al., 2017), enables to characterize aerosol hygroscopic behavior at the particle scale. One of the interests of this approach is that these two methods are complementary. Thus, combining these methods for the analysis of a specific aerosol mixture allows us to provide a more comprehensive view of the properties and processes occurring upon water uptake. In association with these laboratory measurements, the E-AIM thermodynamic model was used to predict the quantity of water uptaken by the aerosol particles and calculate their growth factor as a function of RH. According to our knowledge, this thesis is the first attempt to combine these two laboratory measurement approaches, along with calculations from the E-AIM thermodynamic model. Such a combination of experimental and modeling approaches offers, as main advantages, the possibility to measure scattering properties of a population of aerosols representative of the real atmosphere, as well as to measure morphological and chemical properties of a single particle as a function of RH. Furthermore, both experiments will provide reference data to investigate the agreement or deviations from models as well as from the parameterizations commonly used (ZSR) to reproduce the observed modifications

on aerosol physical properties during humidification.

During this thesis, we studied pure inorganic aerosols ( $NaCl$ ,  $(NH_4)_2SO_4$ ,  $KCl$  and  $NaNO_3$ ) as well as aerosol mixtures such as binary mixtures of compounds with one common ion ( $Cl^-$  in  $NaCl/KCl$  mixture and  $Na^+$  in  $NaCl/NaNO_3$ ) and with no common ion ( $NaCl$  and  $(NH_4)_2SO_4$ ). For both laboratory experimental setups, we first compared  $g(RH)$  as well as DRH with the literature data and modeled (E-AIM and ISORROPIA-II) results and obtained good agreement for pure (single component) aerosols (Chapter 3). Indeed, the DRH from both experimental systems agreed within 0.7% of RH for  $NaCl$  and  $(NH_4)_2SO_4$  and within 1.1% with both thermodynamic models (ISORROPIA-II and E-AIM). These results gave us confidence in our instrumental setup and in our data set to explore more deeply the aerosol properties evolution as a function of relative humidity.

The  $g(RH)$  were also measured with the optical microscope and retrieved from  $f(RH)$  measurements and equation 1.21 (Guo et al., 2015; Bougiatioti et al., 2016). The comparison of results from these two approaches highlighted large differences (up to 62% for  $NaCl$ ) that could come from the particle sizes differences of aerosols investigated in both setups (60  $\mu m$  in the levitation system and 300 nm in the nephelometer measurements). However, the retrieved  $g(RH)$  from Guo et al. (2015) equation are consistent (errors lower than 3%) with previous studies on sub-micron particles for  $NaCl$  (Topping et al., 2005; Hewitt and Jackson, 2009; Hu et al., 2010; Gupta et al., 2015) and  $(NH_4)_2SO_4$  (Wise et al., 2003; Topping et al., 2005; Hewitt and Jackson, 2009; Hu et al., 2010). The  $g(RH)$  retrieved from Guo et al. (2015) equation applied to nephelometer measurements of  $f(RH)$  have then been used to estimate the errors associated with the ZSR method.

For all aerosol mixtures considered in this thesis ( $NaCl/KCl$ ,  $NaCl/NaNO_3$ ,  $NaCl/(NH_4)_2SO_4$ ) our experimental results highlighted that the mutual DRH is always lower than the DRH of both pure aerosols composing the mixture. As the ZSR is a linear relationship, it cannot predict this particular behavior. Therefore, the  $g(RH)_{ZSR}$  were largely underestimated, down to a factor of 2 at the mutual DRH of  $NaCl/KCl$  mixture. Moreover, depending on the molar fraction of  $NaCl$  in the mixture, the  $g(RH)_{ZSR}$ , derived after the DRH, overestimated the measurements in most cases of aerosol mixtures.

To better understand the evolution of a complex aerosol mixture (composed of more than 3 ions) at different RH, multi-component single particles ( $NaCl$  and  $(NH_4)_2SO_4$ ) were generated in the laboratory. The diameter evolution at the particle scale was observed and measured through optical microscopy. Chemical compositions of these particles were determined by Raman microspectrometry at different RH. The evolution of the DRH with the fraction of  $NaCl$  in  $NaCl$  in  $NaCl/(NH_4)_2SO_4$  mixture showed several minima at  $X_{NaCl} = 0.27, 0.70$  and  $0.85$ . These observations were explained with the E-AIM model in which we can allow or not the formation of new species. Indeed, when the model was forced to prevent the formation of new solid species (like  $NH_4Cl, Na_2SO_4 \dots$ ), the DRH evolution with  $NaCl$  fraction shows a classic “V” shape with a specific eutonic point ( $X_{NaCl} = 0.55$ ). When E-AIM was run with the possibility that new species may form, three DRH minima were calculated as a function of  $NaCl$  molar fraction. These results are consistent with Raman spectra, acquired during the humidifying process, that also show formation of new species. This behavior (several minima and the absence of an eutonic point) is thus due to presence of new species in the mixture at different RH. E-AIM model was able to reproduce pretty well the DRH variation observed with the optical microscope setup.

Such a behavior is impossible to reproduce with a linear relationship such as the ZSR. Thus the results of the laboratory experiments performed in this thesis highlight the limitation of this type of parameterization to reproduce the complex hygroscopic behavior of some inorganic aerosol mixtures. Indeed, for the  $NaCl/(NH_4)_2SO_4$  mixture ( $X_{NaCl} = 0.36$ ) at  $RH = 82\%$ ,  $g(RH)$  has been calculated at 3 using the ZSR, while  $g(RH)$  retrieved from the  $f(RH)$  measurements has been calculated at 2.4. These discrepancies between the ZSR and laboratory measurements could lead to large errors on the aerosol radiative forcing estimates for environmental conditions of relative humidity commonly observed within the atmosphere. Therefore, it is deemed essential to better constrain the ZSR within general circulation models, especially for aerosol mixtures including sea-salt. The use of thermodynamic models, such as ISSOROPIA-II or E-AIM, that are able to properly estimate the MDRH of an aerosol mixture could be a valuable solution at the expense of computational costs.

One of the originality of this thesis is that it is based on a multidisciplinary approach, and

multi instrumental laboratory measurements of optical, physical, chemical and hygroscopic properties of both a single particle and an aerosol population for pure and mixed inorganic aerosols containing *NaCl*.

The conclusions obtained after this research allows to refine the knowledge of the complex hygroscopic behavior of aerosol particles especially for mixed aerosols. Using a large instrumental and calculations tools, there are many perspectives for this work and many issues that remain unresolved. One important aspect of the results of this thesis is that working on a single particle, two phase transitions are shown. Contrariwise, while measuring the optical properties of an aerosol population only one phase transition is shown. An hypothesis that could explain this difference is that all aerosols within the nephelometer are not entirely dry even if the measurements were all performed with particles dried below the ERH. Therefore the same setup, including a longer nafion or a second nafion, could be built in order to decrease the RH below 10% and make sure all aerosols are dry. Moreover, the use of a DMA down stream this highly efficient system would enable the study of a single size class and bridge the gap between the single particle study and the aerosol population study. This addition could help to understand the DRH as well as the  $g(\text{RH})$  differences between both methods and experimental setups used in this thesis.

Overall, our approach and results have highlighted the importance of performing measurements at the particle scale, in particular with regard to the particle internal mixing state. For multicomponent aerosols, our Raman spectroscopic analysis evidenced the formation of new species, as well as the evolution of the physical state (liquid or solid) of these species as a function of RH. These findings highlight the complexity to describe precisely the internal structure and chemical heterogeneity at the particle scale: before reaching a well-mixed liquid state at the DRH, the different species constituting the multicomponent particle may co-exist in different physical states, i.e. liquid and crystalline phase-separated state. Ideally, the new species formed during the humidifying process should be quantified. The fraction of all species as well as their  $g(\text{RH})$  could therefore be added into the ZSR relationship. By including the new species in the ZSR relationship, one could check if the  $g(\text{RH})$  calculations would be improved in comparison to the observations. However, even if the molar concen-

trations of species would be known, we can hypothesize that due to the complex internal structure (inhomogeneous spatial distribution of species in the volume particle) observed at the particle scale from our Raman experiments, there would still be discrepancies between ZSR and experimental measurements.

As short-term perspective,  $g(\text{RH})$  values should be calculated using thermodynamic models (E-AIM, ISORROPIA-II) and compared to experimental measurements. Additionally, once the  $g(\text{RH})$  for synthetic particles are known, the evolution of the complex refractive index of aerosols with RH should be quantified using the method developed during this thesis and described in the Annex 5 (Comparison of two methods based on in-situ and laboratory measurements to derive aerosol refractive index). Indeed, the method has been validated for dry aerosols but still need to be tested for wet aerosols.

Moreover, the instrumentations and methods developed during this thesis could be deployed to measure and characterize real atmospheric aerosols. Such an approach could lead to the calculation of the complex refractive indices, which should be compared to those calculated by [Dubovik et al. \(2002\)](#). Such results combined with computations based on a radiative transfer code, would allow to quantify more precisely the impact of hygroscopicity on aerosol radiative forcing.



---

# Annex

---

## Annex 1: Acoustic levitation

We briefly recall the operating principle of acoustic levitation:

- The acoustic pressure wave distorts the medium in which it propagates in the same direction as its propagation, like any longitudinal wave.
- The sound wave is reflected by a reflector at an angle equal to its incident angle.
- When the sound wave is reflected by the reflector, the interaction between its compressions (high pressure areas) and rarefactions (low pressure areas) generates interference. The combination of this interference and the reflected wave creates a standing wave.

An acoustic levitation device consists of a vibrating surface (transducer) allowing the generation of a wave in the ultrasonic field and a reflector as shown in Figure 5.8.

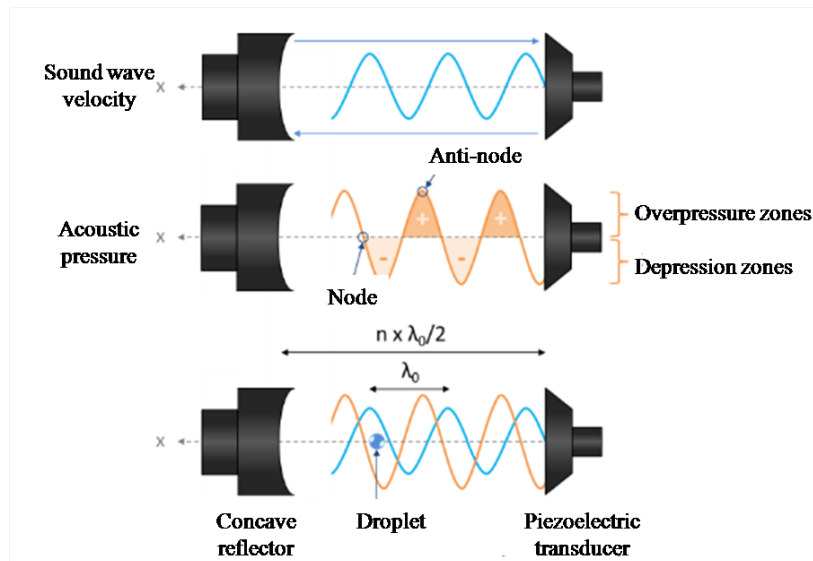


**Figure 5.8:** *Acoustic pressure role in the levitation phenomenon of particles.*

This standing wave is defined by nodes, positions where the pressure is minimal, and antinodes, positions where the pressure is maximum. Particles are trapped near pressure nodes

where acoustic pressure, which is the main source of levitation forces (Brandt, 2001), compensates the gravitational force by a depression in a terrestrial environment. On the other hand, a repulsive action on the particles is created where the pressure is higher (Gor'Kov, 1962). The standing wave is generated when the refractor is placed at  $(n \times \lambda_0/2)$  distance from the transducer. Where  $n$  is any integer and  $\lambda_0$  is the distance that separates two points with the same phase (wavelength). The distance between the transducer and the reflector influences the size of the levitated particle. Indeed particles having a diameter greater than  $2\lambda_0/3$  are not sufficiently stable to stay in suspension. The optimal particle diameter is equal to  $\lambda_0/3$ .

## **Annex 2: Raman spectrum of solid ammonium chloride** ***(NH<sub>4</sub>Cl)***

To confirm the presence of *NH<sub>4</sub>Cl* in *NaCl/(NH<sub>4</sub>)<sub>2</sub>SO<sub>4</sub>* mixtures, we acquired the Raman spectrum of pure solid *NH<sub>4</sub>Cl*. Figure 5.9 represents the Raman spectrum of solid *NH<sub>4</sub>Cl* measured during this work.

The bands centered at  $3049 \text{ cm}^{-1}$  and  $1705 \text{ cm}^{-1}$  confirm the formation of *NH<sub>4</sub>Cl* in the levitated particle.

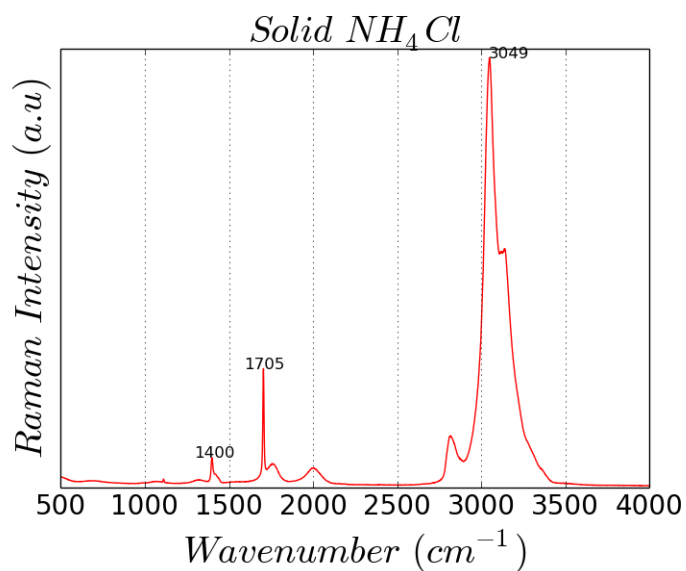


**Figure 5.9:** Raman spectra of solid  $\text{NH}_4\text{Cl}$  obtained with HeNe laser light at 633 nm

### Annex 3: E-AIM calculations for $\text{NaCl}/\text{NaNO}_3$ mixture

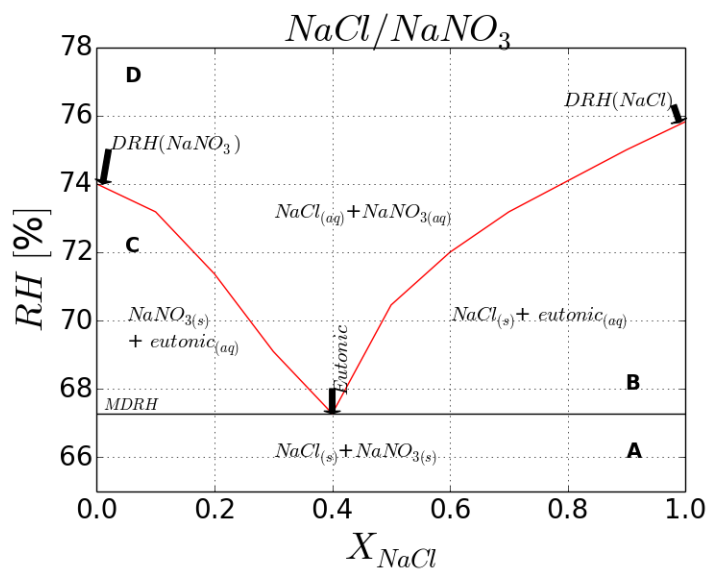


**Figure 5.10:** Deliquescence diagram of  $\text{NaCl}/\text{NaNO}_3$  built using E-AIM. Black and red lines indicate theoretical MDRH (67.9%) and DRH, respectively.

Description of separate areas:

- A-  $NaCl$  and  $NaNO_3$  are both mixed in the solid state for a RH below the MDRH and for all the molar fractions.
- B- Solid  $NaCl$  is in equilibrium with an aqueous phase in the eutonic composition, between the MDRH and the 2<sup>nd</sup> DRH, for  $X_{NaCl}$  greater than 0.38.
- C- Solid  $NaNO_3$  is in equilibrium with an aqueous phase in the eutonic composition, between the MDRH and the 2<sup>nd</sup> DRH, for  $X_{NaCl}$  less than 0.38.
- D-  $NaCl$  and  $NaNO_3$  both are mixed in aqueous form for a higher RH than the 2<sup>nd</sup> DRH and for all the molar fractions.

## Annex 4: ISORROPIA-II

**ISORROPIA II** (Fountoukis and Nenes, 2007), based on ISORROPIA (Nenes et al., 1998) calculates the equilibrium concentrations of the  $NH_4^+$  -  $SO_4^{2-}$  -  $NO_3^-$  -  $Na^+$  -  $Cl^-$  -  $K^+$  -  $Mg^{2+}$  -  $Ca^{2+}$  -  $H_2O$  system. ISORROPIA-II solve two classes of problems the forward one and the reverse one. In our study we used the forward problem in which the temperature, the relative humidity and the total concentrations of  $NH_3$ ,  $HNO_3$ ,  $H_2SO_4$ ,  $HCl$ ,  $Na$ ,  $Ca$ ,  $K$  and  $Mg$  are the known quantities, and equilibrium equations are calculated. Solid, aqueous and gas phase of the potential species for each aerosol type are defined. The final concentrations of each species at thermodynamic equilibrium is given. Unlike E-AIM, ISORROPIA makes use of several assumptions in order to increase the computational speed. For each salt, above its DRH a phase transition from solid to saturated aqueous solution occurs. By plotting the ALWC in  $g/cm^3$  as a function of RH calculated using ISORROPIA-II, the DRH is defined for each salt and compared to the experimental results.

## Calculation of the aerosol liquid water content (ALWC)

The interest of measuring the  $f(RH)$  is that the Aerosol Liquid Water content (ALWC, in  $g.m^{-3}$  of air) can be deduced mathematically from the  $f(RH)$ . The ALWC mostly depends on aerosol hygroscopicity and the ambient RH, and can be calculated with detailed aerosol chemical composition. As this parameter affects the particle size, its lifetime and its scattering efficiency, it constitutes a contributor to aerosol direct radiative cooling (Pilinis et al., 1995). Indeed, the ALWC describes the increasing of an aerosol particle due to the water uptake. It is defined as the difference between the volume of a particle in the ambient conditions and its volume in dry condition.

$$ALWC = \left(\frac{\pi}{6}\overline{D_p(RH)}^3 N_t - \frac{\pi}{6}\overline{D_p(dry)}^3 N_t\right)\rho_w \quad (5.1)$$

Where  $\rho_w$  is defined as the water density ( $1g.cm^{-3}$ ).  $\overline{D_p(dry)}^3$  is represented as a function of the mass concentration of aerosol particles  $m_p$  and the density of a dry aerosol  $\rho_p$ .

$$\overline{D_p(dry)}^3 = \frac{m_p}{\frac{\pi}{6}\rho_p N_t} \quad (5.2)$$

Hence the ALWC is obtained by combining equations 1.21, 5.1 and 5.2 and finally the LWC is defined by equation 5.3.

$$ALWC = [f(RH)^{1.5} - 1] \frac{m_p \rho_w}{\rho_p} \quad (5.3)$$

Hence, from the  $f(RH)$  of each component and by applying the mathematical relation, humidograms showing the variation of the ALWC, deduced from the measurements, as a function of RH are represented in the blue curves in Figure 5.11. In addition, using the thermodynamic model ISORROPIA-II (described in Annex) (Nenes et al., 1998), we calculate

the ALWC of each component at variable relative humidity as represented by the red curves on the same figure.

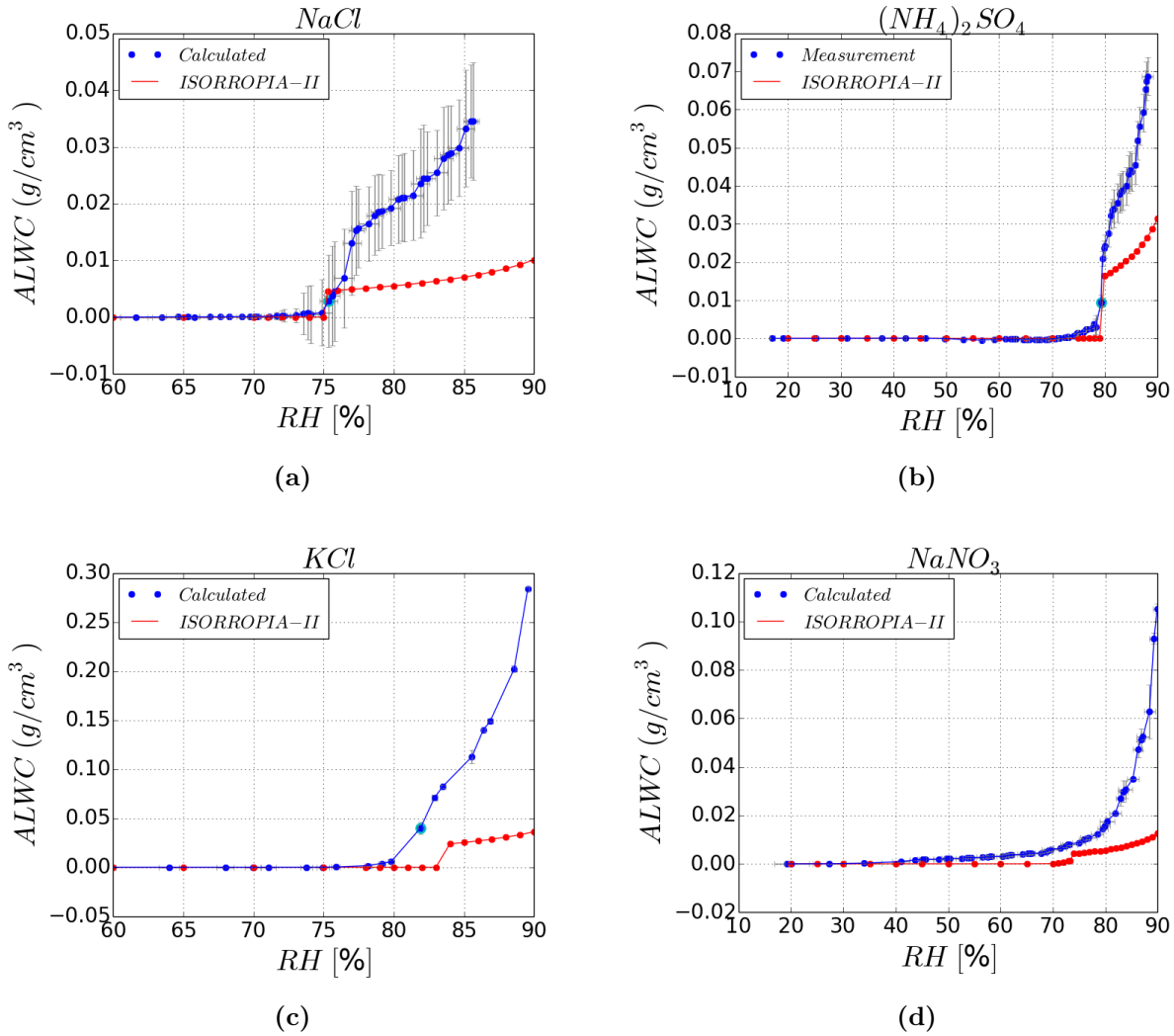


**Figure 5.11:** Variation of particle liquid water content with the relative humidity for sodium chloride (a), ammonium sulfate (b), potassium chloride (c) and sodium nitrate (d).

The blue curves represent results based on the nephelometer measurements and the red curves the calculation made using ISORROPIA-II.

The differences between the two ALWC, i.e. the one calculated based on the nephelometer

measurements and those calculated using ISORROPIA-II appear at RH higher than the DRH for  $NaCl$  and  $(NH_4)_2SO_4$ . These differences which vary between 10% at  $\approx 80\%$  RH and 20% at RH  $> 84\%$  are explained by the mathematical relation linking the ALWC to  $f(RH)$ . Hence, [Guo et al. \(2015\)](#) explain that this relation induces uncertainties on the calculated ALWC estimated to be of the order of 10% at RH=76.4% and that may reach 21% for RH=90%. These uncertainties are caused by the assumption that the scattering efficiencies at ambient and dry conditions are equal. However, for KCl particles (Figure 5.11c), a small difference of about 2% is shown at the DRH and at RH higher than the DRH the same explanation of the difference is shown. Thus, the DRH measured by the nephelometer and calculated using ISORROPIA-II is approximately the same for the three components, but this is not true for  $NaNO_3$  particles that did not show a DRH during the measurements, but a sudden increase of the ALWC at 74% RH using the thermodynamic model. In the following study we choose to work on  $NaCl$  and  $(NH_4)_2SO_4$  aerosol particles.

## Annex 5: Draft article



**Complex refractive index retrievals using high spectral resolution extinction spectrometers and conventional optical in-situ measurements**

Journal:	<i>Aerosol Science &amp; Technology</i>
Manuscript ID	Draft
Manuscript Type:	Original Manuscript
Date Submitted by the Author:	n/a
Complete List of Authors:	Crumeyrolle, Suzanne; Laboratoire d'Optique Atmospherique, El Hajj, Danielle; Laboratoire d'Optique Atmospherique Hubert, Patrice; PhysicoChemistry of Combustion and Atmospheric Processes Petitprez, Denis; PhysicoChemistry of Combustion and Atmospheric Processes Chiapello, Isabelle; Laboratoire d'Optique Atmospherique Choël, Marie; LASIR Herbin, Hervé; Laboratoire d'Optique Atmospherique
Keywords:	Aerosol refractive indexes, retrieving methods, High resolution spectrometers, in-situ measurements

SCHOLARONE™  
Manuscripts

1  
2  
3 **Complex refractive index retrievals using high spectral resolution**  
4 **extinction spectrometers and conventional optical in-situ**  
5 **measurements**  
6  
7  
8  
9

10  
11  
12 S. Crumeyrolle<sup>(a\*)</sup>, D. El Hajj <sup>(a,c)</sup>, P. Hubert <sup>(a,b)</sup>, D. Petitprez <sup>(b)</sup>, I.  
13  
14 Chiapello <sup>(a)</sup>, M. Choël <sup>(c)</sup> and H. Herbin <sup>(a)</sup>  
15  
16  
17  
18  
19  
20  
21

22 <sup>a</sup> Univ. Lille, CNRS, UMR 8518 - LOA - Laboratoire d'Optique Atmosphérique, F-  
23 59000 Lille, France  
24  
25

26 <sup>b</sup> Univ. Lille, CNRS, UMR 8522 - PC2A -Physico-Chimie des Processus de  
27 Combustion et de l'Atmosphère, F-59000, Lille, France.  
28  
29

30 <sup>c</sup> Univ. Lille, CNRS, UMR 8516 - LASIR - Laboratoire de Spectrochimie Infrarouge et  
31 Raman, F-59000 Lille, France  
32  
33  
34  
35  
36  
37  
38  
39  
40  
41  
42

43 Corresponding author: Suzanne Crumeyrolle ([Suzanne.crumeyrolle@univ-lille.fr](mailto:Suzanne.crumeyrolle@univ-lille.fr))  
44  
45  
46  
47  
48  
49  
50  
51  
52  
53  
54  
55  
56  
57  
58  
59  
60

1  
2  
3 **Complex refractive index retrievals using high spectral resolution**  
4 **extinction spectrometers and conventional optical in-situ**  
5 **measurements**  
6  
7  
8  
9  
10  
11  
12

13 An accurate assessment of aerosol radiative effects on climate change requires a better  
14 knowledge of complex refractive indices (CRIs) of atmospheric aerosols. Indeed,  
15 aerosol CRI is a key parameter used to (i) quantify their concentration within the  
16 atmosphere based on remote sensing techniques, (ii) establish the link between their  
17 chemical composition and optical properties (iii) estimate their radiative forcing. As no  
18 instrument directly provides CRI measurements, its determination represents one of the  
19 major sources of uncertainty in current aerosol climate models. Although it is possible  
20 to estimate CRI from different approaches, current CRI retrievals are generally highly  
21 depending on the measurements and numerical methods used. Recent studies attempting  
22 to compare the CRI retrievals from different methods highlighted that most significant  
23 differences are associated to the size distribution, the chemical composition as well as  
24 the mixing state of the measured aerosols (McConnell et al., 2010). In this work, the  
25 CRI retrieving method based on conventional in-situ measurements is compared to a  
26 new method based on laboratory extinction spectra measurements (Herbin et al., 2017).  
27 To avoid differences related to the particle size, morphology, chemical composition and  
28 mixing state, pure, spherical and calibrated silica (amorphous SiO<sub>2</sub>) particles have been  
29 aerosolized. These particles were simultaneously measured by high spectral resolution  
30 (HR method) spectrometer and by conventional optical (CV method) in-situ instrument  
31 working within the visible range.  
32  
33  
34  
35  
36  
37  
38  
39  
40  
41  
42  
43  
44  
45  
46  
47  
48  
49  
50  
51  
52  
53  
54  
55  
56  
57  
58  
59  
60

1  
2  
3           Keywords: aerosol ; complex refractive index ; conventional in-situ method; high  
4           spectral resolution extinction spectrometers  
5  
6  
7  
8  
9  
10

## 11           **Introduction**

12  
13  
14           Aerosols present in the atmosphere are a complex mixture of different particles emitted  
15  
16           from natural sources (sea salt, volcanic eruptions, forest fires, wind erosion, etc.), and  
17  
18           human activities (transport, heating, industry, agriculture, etc.). They affect the radiative  
19  
20           balance of our planet by absorbing and scattering incoming radiation (Moise et al.,  
21  
22           2015; Ramanathan et al., 2001), and indirectly through their role as cloud condensation  
23  
24           nuclei (Bréon et al., 2002; Charlson et al., 1992; Rosenfeld et al., 2008). These effects  
25  
26           are highly depending on aerosol chemical and physical properties that determine their  
27  
28           optical properties. The understanding of the atmospheric aerosol radiative forcing is  
29  
30           currently low in comparison to other radiative effects such as of greenhouse gases (see  
31  
32           e.g. (Fuzzi et al., 2006; Myhre et al., 2013; Stocker et al., 2013). For instance, the mass  
33  
34           and radiative forcing of black carbon, one of the most important global warming driving  
35  
36           factor (Bond et al., 2013), are estimated by models with large uncertainties, over 200%,  
37  
38           (Koch et al., 2009; Schuster et al., 2015). Complex refractive indices (CRIs) of the  
39  
40           different types of atmospheric aerosols are the fundamental parameter required to  
41  
42           estimate properly their climate effects (Boucher et al., 2013). Moreover, the CRI along  
43  
44           with size distribution or optical properties such as single scattering albedo are also used  
45  
46           to retrieve part of the aerosol chemical composition : Black Carbon (BC) and Brown  
47  
48           Carbon (BrC) concentrations, water uptaken by aerosols (Schuster, 2005; Schuster et  
49  
50           al., 2009; Wang et al., 2016). Therefore, an effort for reducing current uncertainties on  
51  
52           aerosol CRI is deem essential.  
53  
54  
55  
56  
57  
58  
59  
60

1  
2  
3 Real time retrievals of aerosol refractive index can be achieved using in-situ  
4  
5 measurements of aerosol optical properties (scattering and absorption coefficients) and  
6  
7 size distributions (e.g., (Kostenidou et al., 2007; Malloy et al., 2009; McMurry et al.,  
8  
9 2002). In-situ measurements of aerosol scattering, extinction and absorption coefficients  
10  
11 are performed at few fixed wavelengths within the visible range using nephelometers,  
12  
13 cavity attenuated phase shift (CAPS) monitor (Aerodyne Research, Inc.), aethalometer  
14  
15 (AE, Magee Scientific), Multi-Angle Absorption Photometer (MAAP, Thermo  
16  
17 scientific), or Particle Soot Absorption Photometers (PSAP, Radiance Research). The  
18  
19 most recent in-situ instrumentation used to retrieve aerosol CRI are nephelometers  
20  
21 (TSI or Ecotech at three wavelengths: 450nm, 525nm, and 635nm) and aethalometers  
22  
23 (MAGEE Scientific AE-33 at 7 wavelengths: 370, 470, 520, 590, 660, 880 and 950  
24  
25 nm). Due to the limited number of wavelengths in the nephelometer, aerosol optical  
26  
27 information is very restricted and may lead to high errors on the refractive index  
28  
29 retrievals.  
30  
31  
32  
33  
34  
35

36 For example, McConnell et al. (2010) compared imaginary part of Dust, collected  
37  
38 during the DODO (Dust Outflow and Deposition to the Ocean) campaign over West-  
39  
40 Africa, refractive index resulting from in-situ and AERONET measurements. They  
41  
42 showed that most of the discrepancies are related to the difference in particle chemical  
43  
44 composition as well as their mixing state. However, these methods have not been yet  
45  
46 compared using the same aerosol population and under similar environmental  
47  
48 conditions (RH, temperature and pressure).  
49  
50  
51

52 To carry out these ideal measurements, our study consists in performing laboratory  
53  
54 measurements, using both conventional in-situ optical and high spectral resolution  
55  
56 extinction laboratory instruments, on calibrated silica (amorphous silicon dioxide)  
57  
58 spherical particles. Indeed, laboratory studies have been recently developed in order to  
59  
60

1  
2  
3 estimate the CRI of aerosols (Biagio et al., 2017; Herbin et al., 2017; Reed et al., 2018)  
4  
5 using high spectral resolution extinction measurements over a wide spectral range.  
6  
7 Especially, Herbin et al. (2017) method, called herein High spectral resolution (HR)  
8  
9 method, has shown no significant error and less than 1% uncertainty in the UV–visible  
10  
11 spectral range while, in the infrared region, the total error reaches 2% around the  
12  
13 vibrational bands. Even if the HR method has provided promising results, laboratory  
14  
15 instruments, measuring extinction spectra with a high spectral resolution on a wide  
16  
17 spectral range, including infrared ( $650 - 2500 \text{ cm}^{-1}$ ) and UV-visible ( $9000 - 32500$   
18  
19  $\text{cm}^{-1}$ ), are not devoted to field measurements and therefore can not be used to monitor  
20  
21 the ambient aerosols. The comparison of both methods is therefore highly needed to  
22  
23 find out the limits and the best measurement conditions, especially for conventional  
24  
25 optical in-situ instruments that equipped most of the current surface aerosol networks,  
26  
27 as for example ACTRIS (Pandolfi et al., 2018).  
28  
29  
30  
31  
32  
33

34 The aim of this study is to compare CRI retrievals from in-situ optical and high spectral  
35  
36 resolution extinction methods using both numerically generated and laboratory  
37  
38 measured extinction, scattering and absorption spectra. In order to validate both  
39  
40 methods for different particle types, CRI of low and high–absorbing particles were used  
41  
42 to numerically generate optical spectra. The authors refer here to low and high–  
43  
44 absorbing particle only within the visible range. Silica (amorphous silicon dioxide) was  
45  
46 selected as a proxy for mineral atmospheric particles (dust-like particles). The  
47  
48 instrumental set up as well as the instrumental methodology are described in section 1  
49  
50 and section 2. Then, the aerosol refractive index values retrieved from both methods  
51  
52 are compared, based on the numerical approach (section 3) and on the experimental  
53  
54 laboratory tests (section 4). Finally, the main conclusions are given in section 5.  
55  
56  
57  
58  
59  
60

## **Instrumental set-up**

Laboratory experiments performed in this study aim to perform a robust comparison between refractive index retrieval methods, i.e, the one based on in-situ conventional optical measurements and the high spectral resolution extinction approach. All experiments consisted of introducing a constant flow of well-known aerosols into laboratory instruments (HR method) and then into Conventional Optical in-situ instruments (CV method). The experimental set-up is divided in 3 blocks (Fig. 1) detailed hereafter: aerosol generation (Part A), HR (Part B) and CV (Part C) measurements. All experiments are carried out at room temperature ( $T = 293$  K) and at atmospheric pressure ( $p = 1013$  hPa).

### ***Aerosol generation (Part A)***

Calibrated silica (amorphous silicon dioxide) spherical particles (with a diameter of 0.5  $\mu\text{m}$  and 1.0  $\mu\text{m}$  and density of 1.8  $\text{g}\cdot\text{cm}^{-3}$ , Fiber Optic Center) were aerosolized. Their specific morphological and physical properties offer an ideal study case for our experiment. The sample is dried for several hours prior to the experiment to remove residual water. The powder is introduced within a glass container, it is then aerosolized by a continuous agitation using a magnetic stirrer and a flow of pure nitrogen gas (99.996% purity). The  $\text{N}_2$  flow (optically transparent within the infra-red range; 5  $\text{L}\cdot\text{min}^{-1}$ ) containing suspended silica particles was monitored by a mass flow controller. A buffer volume was placed at the exit of the glass container in order to obtain homogeneous well-mixed aerosol flow and to ensure the production of a steady/continuous stream of silica particles whose stability was checked by continuous monitoring of the particle number concentration. Finally, the position of the instruments and the length of the pipes were optimized in order to minimise particle losses. Thus,

1  
2  
3 size distributions and number concentrations were compared upstream and downstream  
4  
5 of the spectrometers, showing no change in the size distributions and negligible particle  
6  
7 losses in this setup (Hubert et al., 2017).  
8  
9

10  
11 Prior to laboratory experiments, submicronic and micronic silica particles were  
12  
13 generated and their size distributions were measured with a Scanning Mobility Particle  
14  
15 Sizer (TSI SMPS model 3936L75) and with an Aerodynamic Particle Sizer (TSI APS  
16  
17 model 3321), respectively. These measurements showed particle diameters centered on  
18  
19 500nm and 1 $\mu$ m as expected but also that the concentration varied with time. Therefore,  
20  
21 aerosol total concentrations need to be recorded during the whole experiment while the  
22  
23 size distribution is constant. It is important to note that particles size distribution  
24  
25 measured by the APS should be adjusted according to the density and shape factor.  
26  
27 However, in this study, the density was given by the manufacturer and the sample was  
28  
29 only composed of calibrated spherical particles confirmed by scanning electron  
30  
31 microscopy (SEM) so the geometrical diameter is equivalent to the aerodynamic  
32  
33 diameter measured by the APS.  
34  
35  
36  
37  
38

39  
40 After introducing the silica powder into the container, the whole experimental set-up  
41  
42 was purged by flowing nitrogen gas for one hour in order to evacuate possible residual  
43  
44 CO<sub>2</sub> and water (RH < 1%). Then, a background reference spectrum (nitrogen stream  
45  
46 without particles) was measured with both FTIR and UV-visible spectrometers. The  
47  
48 magnetic stirrer was afterward activated in order to resuspend silica particles that were  
49  
50 entrained within the nitrogen flow. Aerosol concentration was measured using the  
51  
52 Condensation Particle Counter (CPC -TSI model 3775). The extinction spectra were  
53  
54 recorded when the aerosol total concentration was stable.  
55  
56  
57  
58  
59  
60

### ***High spectral resolution extinction measurements (Part B)***

A UV-Visible-NIR (UV-visible) spectrometer (MAYA 2000 PRO, Ocean Optics), equipped with a 2068x70-pixel CCD (Charge-Coupled Device) device, was used to measure the extinction in the spectral range from 300 nm to 1  $\mu\text{m}$ . The beam, generated by halogen and deuterium sources, was directed through quartz windows to a 1 m single-pass cell using optical fibers with matched collimated lenses (Deguine et al., 2019). The UV-visible spectrometer was enclosed in a black box in order to remove parasite visible background light from the laboratory. A Fourier Transform InfraRed (FTIR) spectrometer (Antaris IGS Analyser, ThermoScientific), equipped with a DTGS (Deuterated TriGlycine Sulfate) detector measured the IR extinction spectra in the spectral range from 650 to 3500 $\text{cm}^{-1}$ . The IR beam, from a Globar source, was directed through ZnSe windows in a 10m multi-pass cell that is small enough (10cm) and is placed horizontally in order to minimize the particle losses by sedimentation as well as impaction on the windows.

Extinction spectra were measured simultaneously in both the IR and UV-visible spectral regions. Both spectrometers were set to collect data over the same 180 s time period. This respectively corresponded to an average of 180 scans at 1  $\text{cm}^{-1}$  spectral resolution for the FTIR spectrometer and an average of 1800 scans at 1 nm spectral resolution for the UV-visible spectrometer. Such acquisition parameters allowed measuring experimental extinction spectra with a good compromise between signal-to-noise ratio, estimated to be better than 100, and concentration stability. The signal-to-noise ratio was taken into account as measurement uncertainties (see section 2.1) in the retrieving process (Herbin et al., 2017).

### *In-situ conventional optical measurements (Part C)*

Absorption coefficient measurements were performed every minute by an AE16 aethalometer (Magee Scientific, 1 wavelength: 880 nm). Aethalometer signal have a known scattering interference from particles deposited on the collection filter, and the measurements were post-corrected following Collaud Coen et al. (2010). Dry scattering coefficient measurements were also made every minute using a three-wavelength nephelometer (Aurora 3000, ECOTECH) operating at 450, 525, and 635 nm. The nephelometer was calibrated using filtered air and CO<sub>2</sub> prior to, during, and after the laboratory measurements. The scattering coefficients were corrected from angular truncation errors and illumination intensity non-idealities based on (Müller et al., 2011). Both instruments relative uncertainties given by the manufacturer are about 10%. Scattering and absorption coefficients were averaged over a 180s time to ease the comparison with spectrometer measurements.

In order to calculate the dry extinction coefficient ( $\sigma_{\text{scat},\lambda} = \sigma_{\text{scat},\lambda} + \sigma_{\text{abs},\lambda}$ ), the scattering coefficient was extrapolated to 880 nm using the measured scattering Ångström exponent between 450 and 635 nm (Equation 1). The scattering coefficient extrapolation is possible only when the scattering coefficient is linear as a function of the wavelength. Simulations using a Mie code for absorbing (BC like) and low-absorbing (dust like) particles were performed to better understand the validity of the extrapolation method. **Error! Reference source not found.** shows the normalized extinction for both types of particles (a) dust-like (Du) and b) black carbon like (BC), with different diameters as a function of the wavelength. At 525nm, the refractive indexes are mBC = 1.8939 +

1  
2  
3 i 0.6043 (Chang and Charalampopoulos, 1990) and  $m_{Du} = 1.3470 + i 0.0476$  (Hubert et  
4  
5 al., 2017).  
6  
7

$$\frac{\sigma_{scat, \lambda_1}}{\sigma_{scat, \lambda_2}} = \left( \frac{\lambda_1}{\lambda_2} \right)^{-\alpha} \quad (\text{Equation 1})$$

8  
9  
10  
11  
12  
13  
14  
15  
16  
17 The comparison of the normalized extinction of each type of particles, with different  
18 diameters, highlights that the normalized extinction maximum is shifted toward larger  
19 wavelengths along with larger diameters. Indeed, the maximum extinction for dust  
20 particles occurs around 570 nm for dust particles with a diameter of 600 nm, while it  
21 occurs at 960nm for dust particles with a diameter of 1000nm. The same tendency is  
22 observed for BC-like particles with maxima observed at 280, 640 and 820 nm for  
23 particles with diameter of 200, 400 and 600 nm, respectively. Moreover, the normalized  
24 extinction maximum of different types of particles (BC-like versus dust-like particles),  
25 thus having different real part of the refractive index, with the same diameter is not  
26 observed at the same wavelength (See Figure 2). As an example, the normalized  
27 extinction maximum of particles with diameter of 600nm is observed at 570nm for dust-  
28 like particles while it is observed at 820nm for BC-like particles. Indeed, the extinction  
29 maximum is shifted toward larger wavelengths for particles with larger RRI.  
30  
31  
32  
33  
34  
35  
36  
37  
38  
39  
40  
41  
42  
43  
44  
45  
46  
47

48 As extinction coefficient variations as a function of wavelength are not linear in the  
49 visible range (450 – 880nm), extinction or scattering extrapolation method within the  
50 visible range should be used carefully. For atmospheric aerosols, the extrapolation  
51 method cannot be used due to the lack of chemically resolved size distribution for high-  
52 absorbing and low-absorbing aerosols.  
53  
54  
55  
56  
57  
58  
59  
60

## Methods

### *High spectral resolution (HR) method*

The real  $n$  and imaginary  $\kappa$  parts of CRI are determined from an algorithm described in detail in Herbin et al. (2017), which is briefly summarized hereafter. The latter uses measured extinction spectra (IR and UV.-visible) and particle size distribution measurements, as well as an association of Mie theory, Single Subtractive Kramers-Kronig (SSKK) relation, and Optimal Estimation Method (OEM) in an iterative process.

The OEM procedure (equation n of Herbin et al., 2017) requires a priori values  $n_a$  and  $\kappa_a$  of the state vector  $x$ . The first guess for the imaginary part,  $\kappa_a$ , is obtained from the Rayleigh theory over the whole spectral range. Then, the SSKK relation is performed to estimate the real component,  $n_a$ . The OEM also requires constraints specified by covariance matrices. The latter are assumed to be diagonal and correspond to the measurement noise variance matrix  $S\varepsilon$ , the uncertainties on the aerosol concentration and size distribution  $Sb$ , and the *a priori* variance matrix  $Sa$  corresponding to the variability of  $n_a$  and  $\kappa_a$ . Here,  $S\varepsilon$  is built from the signal-to-noise ratio of the spectra which are estimated to be 100 and 50 in the Infrared and UV-visible regions respectively.  $Sb$  is evaluated from the size distribution uncertainties which have been determined previously by Hubert et al., 2017 and set to 8% for size distribution and 19% for number particle concentration. Finally, in order to minimize the impact of the *a priori* on the retrieval results the  $Sa$  matrix is estimated in considering a 100 % variability on the  $n_a$  and  $\kappa_a$  estimations.

At each iteration, an extinction spectrum is calculated ( $E_{calc.}$ ) using Mie theory from particle size distribution and the new values of  $n_i$  and  $\kappa_i$ , and it is compared to the

1  
2  
3 measured extinction spectrum ( $E_{obs.}$ ). The retrieved CRI at each measured wavenumber  
4  
5 is obtained after convergence, when the absolute difference ( $E_{calc.} - E_{obs.}$ ) between two  
6  
7 successive iteration steps, is less than a fraction (typically) 2% of the instrumental noise.  
8  
9

10  
11 The uncertainty on the final retrieved CRI, as characterized by the OEM (see equation  
12  
13 N+1 of Herbin et al., 2017), is typically around 2% for both real and imaginary parts,  
14  
15 and are mainly driven by concentration and size distribution uncertainties.  
16  
17

### 18 19 ***Conventional (CV) in-situ method***

20  
21  
22 Extinction, scattering and absorption coefficients can be directly calculated using Mie  
23  
24 theory (Bohren and Huffman, 1981) knowing particle size distribution and their CRI.  
25  
26 Mie theory is only designed for spherical particles. Conversely, with knowledge of  
27  
28 optical behavior and morphology as measured by laboratory equipment, one can  
29  
30 determine the CRI by solving this inverse problem.  
31  
32

33  
34  
35 For in-situ measurements with fixed wavelength measurements, the refractive index is  
36  
37 retrieved with an iterative code based on Mie theory (Bond et al., 2006). The inputs are  
38  
39 the size distribution and an a-priori refractive index (1.55+0.001i). First, the scattering  
40  
41 and absorption coefficients are calculated using the a priori CRI for all wavelengths.  
42  
43 Then, scattering and absorption relative errors between measurements and Mie  
44  
45 calculations are calculated and used to adjust the a priori RRI and IRI, respectively.  
46  
47 This RRI and IRI adjustment is proportional to the relative errors that allow a fine-  
48  
49 tuning of aerosol CRI. The refractive index is considered as the best match since the  
50  
51 relative errors between calculated and measured scattering and absorption coefficients  
52  
53 are lower than 3%.  
54  
55  
56  
57  
58  
59  
60

1  
2  
3  
4  
5  
6  
7  
8  
9  
10  
11  
12  
13  
14  
15  
16  
17  
18  
19  
20  
21  
22  
23  
24  
25  
26  
27  
28  
29  
30  
31  
32  
33  
34  
35  
36  
37  
38  
39  
40  
41  
42  
43  
44  
45  
46  
47  
48  
49  
50  
51  
52  
53  
54  
55  
56  
57  
58  
59  
60

### *Numerical comparison*

As a first step, a numerical comparison is performed in order to estimate the drifts inherent to both methods used in this study. This numerical comparison is based on optical coefficients (extinction, scattering and absorption) computed using a Mie code for aerosols with known size distribution and refractive index. Then, these optical properties along with the size distribution are used as inputs in HR and CV methods. The refractive indices are then calculated and compared to the initial refractive indexes. Results are presented in

1  
2  
3 Table 1 for dust-like and BC-like particles at three wavelengths (450, 525 and 635nm).  
4  
5

6 For dust-like particles (low-absorbing), the real part of reference refractive index varies  
7  
8 from 1.444 to 1.4455 and the imaginary part is between  $7.8 \cdot 10^{-5}$  and  $21.9 \cdot 10^{-5}$  within the  
9  
10 visible range. Using the HR method, the refractive index is retrieved at  $1.441 + i7.8e^{-5}$  at  
11  
12 450 nm, and  $1.444 + i 21.9 \cdot 10^{-5}$  at 635 nm. Whereas, the CV retrievals are of  $1.460 + i 10$   
13  
14  $10^{-5}$  and  $1.449 + i 20 \cdot 10^{-5}$  at 450 and 635 nm respectively. Both methods give good  
15  
16 results for the real part of the refractive index in comparison to the reference one with  
17  
18 relative errors lower than 2%. Furthermore, the HR method is able to accurately  
19  
20 estimate the imaginary part of the refractive index (0% errors) for all wavelengths.  
21  
22 Contrariwise, the discrepancies between the imaginary part calculated by the CV  
23  
24 method and the reference are large (>5%) for all wavelengths and reach 28% at 450 nm.  
25  
26 However, the imaginary parts of the RI retrieved by both methods are on the same order  
27  
28 of magnitude (between  $10 \cdot 10^{-5}$  to  $22 \cdot 10^{-5}$ ) and are extremely low. Interestingly, the  
29  
30 largest errors for both real and imaginary parts calculated from both methods are found  
31  
32 at 450 nm.  
33  
34  
35  
36  
37

38 The refractive index of BC-like particles (high-absorbing particles) is given by Chang  
39  
40 and Charalampopoulos et al. (1990). The real part within the visible range is between  
41  
42 1.706 - 1.759 while the imaginary part is in the range 0.575 - 0.639. Refractive indexes  
43  
44 retrieved from both methods are similar and comparable to the reference with errors  
45  
46 lower than 2% and 7% for the real and the imaginary part respectively. At 525 nm, the  
47  
48 imaginary part of the reference refractive index is equal to 0.604, and retrieved at 0.585  
49  
50 and 0.576 using HR and CV methods respectively. Once more, the CV method  
51  
52 retrievals show the largest discrepancies in comparison to the reference, especially for  
53  
54 the shortest wavelength (i.e. 450nm). The largest discrepancies on the imaginary part of  
55  
56 the HR retrievals are observed at 635nm.  
57  
58  
59  
60

1  
2  
3 Overall, this numerical comparison shows that both methods are rather accurate to  
4 retrieve the real part of the refractive index with relative errors lower than 2%.  
5  
6 However, retrieving the imaginary part of the refractive index using the CV method  
7  
8 seems to be more challenging, especially when the imaginary part is low (error up to  
9  
10 28%). The HR method allows retrieving the imaginary part properly for both high-  
11  
12 absorbing and low-absorbing particles and will therefore be used as a reference during  
13  
14 the comparison of experimental results.  
15  
16  
17  
18  
19  
20  
21  
22

### 23 **Experimental comparison**

24  
25 During our experimental laboratory measurements, only low-absorbing (dust-like)  
26  
27 particles were generated. Indeed, there are some theoretical and experimental issues  
28  
29 about using high-absorbing particles within our laboratory experimental setup. High-  
30  
31 absorbing particles, within the visible range, are mostly considered as non-spherical  
32  
33 particles. However, both methods, due to Mie assumptions, are exclusively devoted to  
34  
35 retrieve CRI of spherical particles. The best solution found by both methods would then  
36  
37 not represent the CRI of the generated aerosol.  
38  
39  
40  
41  
42

43 Figure 3a shows the scattering coefficients from in-situ instruments (Nephelometer) as a  
44  
45 function of extinction coefficients measured from UV-Vis spectrometer at 450, 525, and  
46  
47 635nm for spherical SiO<sub>2</sub> particles with a diameter of 500nm and 1 $\mu$ m. Extinction and  
48  
49 scattering coefficients are observed from 300Mm<sup>-1</sup> to 8000Mm<sup>-1</sup>. The comparison  
50  
51 shows a good agreement with significant correlation (slope =1, R<sup>2</sup> = 0.98, N=249).  
52  
53 This result highlights that the instrumental set-up was working properly and that particle  
54  
55 losses within both spectrometers and in-situ measurements were negligible. Scattering  
56  
57 coefficients are then extrapolated to the wavelength of the absorption coefficient  
58  
59  
60

1  
2  
3 measurements (880nm). The extinction coefficients are compared to extinction  
4  
5 coefficients measured by UV-Visible spectrometer at 880nm for spherical SiO<sub>2</sub>  
6  
7 particles with diameter of 500nm (squares) and 1 μm (dots, Figure 3b). Due to  
8  
9 scattering coefficient non-linearities (see section 1.3) within the visible range, the  
10  
11 extrapolated extinction coefficients for 1μm particles were overestimated by a factor of  
12  
13 1.77 in average. In the following sections, we will only use measurements performed on  
14  
15 500nm diameter particles to test CRI retrieving methods.  
16  
17

18  
19  
20 The results reported Table 2 show that the RRI are retrieved at 1.443 and 1.448 by the  
21  
22 HR and CO method respectively. These values are similar and fall into the large range  
23  
24 values given by the supplier (1.38-1.46). Both HR and CV retrieved IRI values are quite  
25  
26 low ( $< 5 \cdot 10^{-3}$ ) but significantly different (factor of 4). Indeed, the IRI is retrieved at  $5.8$   
27  
28  $10^{-4}$  and at  $26 \cdot 10^{-4}$  for HR and CV method, respectively.  
29  
30

31  
32 These experimental comparison results are consistent with those of the numerical  
33  
34 comparison: 1) RRI are retrieved within the percent between both methods; 2) the IRI  
35  
36 retrieved by the in-situ CV method is larger than the IRI of the HR method but within  
37  
38 the same order of magnitude. To further explore the consequences of using different  
39  
40 methods to retrieve CRI, we used Mie code to estimate the radiative forcing efficiency.  
41  
42 Using both CRI (HR and CV) as well as the observed size distribution as inputs in Mie  
43  
44 code, we found radiative forcing efficiency at -332 and -299 W/cm<sup>3</sup> of aerosol,  
45  
46 respectively for HR and CV retrievals. A large difference (factor of 4) on small IRI  
47  
48 values could lead to a 10% difference in the radiative forcing efficiency. This result  
49  
50 highlights that the aerosol radiative forcing estimation is then highly depending on the  
51  
52 method used to retrieve the aerosol refractive index.  
53  
54  
55  
56  
57  
58  
59  
60

## Conclusion and perspectives

This study aims to compare two methods to retrieve complex refractive index of aerosol particles. The first method is based on high spectral resolution over a wide spectral range (from UV to IR) spectrometer measurements of aerosol extinction usually performed during laboratory experiments. The second method is based on in-situ instruments working within the visible range and measuring aerosol scattering and absorption coefficients. These instruments (nephelometer and aethalometer) are generally deployed in air quality stations and aerosol surface networks (ACTRIS). This study is trying to validate the so-called 'in-situ' conventional optical (CV) method.

First of all, the conventional in-situ instrument used in this study has one major drawback. The scattering and absorption coefficients could not be measured at the same wavelengths. Therefore, an interpolation or extrapolation is needed to retrieve the extinction coefficient. However, the interpolation or extrapolation is only possible if the optical coefficients evolve linearly with wavelengths. We performed Mie calculations for high-absorbing and low-absorbing particles with different diameters to estimate the evolution of their extinction coefficients. The results highlight that the evolution of high-absorbing particle extinction coefficients with diameter larger than 200 nm is not linear in the visible range. Moreover, extinction coefficients of low-absorbing particles evolve linearly only when diameters are lower than 600 nm or larger than 1000nm. The type (high-absorbing or low-absorbing in the visible range) and the size of particles are therefore essential to be known. For real atmosphere measurements, interpolation or extrapolation are then risky to perform due to aerosol mixing state and unknown particle types. New developed instruments, such as the aethalometer (AE33), provide absorption measurements at multiple wavelengths. However, none of these wavelengths correspond to nephelometer wavelengths and therefore interpolation will be needed to

1  
2  
3 extract the aerosol extinction coefficients. The linearity of the spectral tendency for all  
4  
5 wavelengths needs to be studied prior to perform the interpolation.  
6  
7

8  
9 Secondly, the RI retrievals from conventional in-situ (CO) and high spectral resolution  
10 (HR) methods are compared numerically and experimentally. Both methods are  
11 numerically compared based on known aerosol refractive index, size distribution, and  
12 optical (extinction, scattering and absorption coefficients) properties. Both methods  
13 retrieved accurately the real part of the refractive index (RRI) with an error lower than  
14 2%. For low-absorbing (in the visible range) aerosols, the errors associated with the  
15 retrievals of the imaginary part of the refractive index (IRI) from the CO method are  
16 large, up to 28%. On the contrary, the HR method is retrieving the imaginary part well  
17 (error lower than 3%) for both high-absorbing and low-absorbing particles. These  
18 results show the robustness of HR method that has therefore been used as a reference  
19 during the experimental comparison.  
20  
21  
22  
23  
24  
25  
26  
27  
28  
29  
30  
31  
32

33  
34  
35 Calibrated spherical SiO<sub>2</sub> particles were generated to compare results from both  
36 methods for model particles. The experimental comparison highlights good results for  
37 both method. The RRI retrievals from the CO method are within the percent in  
38 comparison to the reference method (HR method). Moreover, as previously shown with  
39 the numerical comparison, the IRI retrieved by the in-situ method are larger than the IRI  
40 of the HR method but still within the same order of magnitude.  
41  
42  
43  
44  
45  
46  
47  
48

49  
50 To complete this study and analyze the limitations of the CO method more  
51 experimental work needs to be done with different types of ideal absorbing particles and  
52 with internally/externally mix of aerosols. Despite the critical need of wet aerosol CRI  
53 retrievals, measurements at high humidity could not be performed in the present work  
54 due to the presence of soluble material within the spectrometers. Providing technical  
55  
56  
57  
58  
59  
60

1  
2  
3 improvements (non-soluble elements within laboratory instruments, aerosol inlets), the  
4  
5 same work could be done at variable humidities and with real aerosol. The CRI  
6  
7 retrievals for real aerosols could then be compared to those calculated from AERONET  
8  
9  
10 measurements.

11  
12  
13  
14  
15 Acknowledgements: DEH's PhD grant and part of the instrumental system have been  
16  
17 financially supported by the CaPPA project (Chemical and Physical Properties of the  
18  
19 Atmosphere), which is funded by the French National Research Agency (ANR) through the PIA  
20  
21 (*Programme d'Investissement d'Avenir*) under contract "ANR-11-LABX-0005-01", by the  
22  
23 Regional Council "*Hauts-de-France*" and the European Regional Development Fund (ERDF).  
24  
25  
26  
27  
28  
29  
30  
31  
32  
33  
34  
35  
36  
37  
38  
39  
40  
41  
42  
43  
44  
45  
46  
47  
48  
49  
50  
51  
52  
53  
54  
55  
56  
57  
58  
59  
60

- 1  
2  
3  
4 Biagio, C.D., Formenti, P., Balkanski, Y., Caponi, L., Cazaunau, M., Pangu, E.,  
5 Journet, E., Nowak, S., Caquineau, S., Andreae, M.O., Kandler, K., Saeed, T.,  
6 Piketh, S., Seibert, D., Williams, E., Doussin, J.-F., 2017. Global scale  
7 variability of the mineral dust long-wave refractive index: a new dataset of in  
8 situ measurements for climate modeling and remote sensing. *Atmospheric*  
9 *Chem. Phys.* 17, 1901–1929. <https://doi.org/10.5194/acp-17-1901-2017>  
10  
11  
12  
13  
14 Bond, T.C., Doherty, S.J., Fahey, D.W., Forster, P.M., Berntsen, T., DeAngelo, B.J.,  
15 Flanner, M.G., Ghan, S., Kärcher, B., Koch, D., Kinne, S., Kondo, Y., Quinn,  
16 P.K., Sarofim, M.C., Schultz, M.G., Schulz, M., Venkataraman, C., Zhang, H.,  
17 Zhang, S., Bellouin, N., Guttikunda, S.K., Hopke, P.K., Jacobson, M.Z., Kaiser,  
18 J.W., Klimont, Z., Lohmann, U., Schwarz, J.P., Shindell, D., Storelvmo, T.,  
19 Warren, S.G., Zender, C.S., 2013. Bounding the role of black carbon in the  
20 climate system: A scientific assessment: BLACK CARBON IN THE CLIMATE  
21 SYSTEM. *J. Geophys. Res. Atmospheres* 118, 5380–5552.  
22 <https://doi.org/10.1002/jgrd.50171>  
23  
24  
25  
26  
27  
28  
29 Bond, T.C., Habib, G., Bergstrom, R.W., 2006. Limitations in the enhancement of  
30 visible light absorption due to mixing state. *J. Geophys. Res. Atmospheres* 111,  
31 D20211. <https://doi.org/10.1029/2006JD007315>  
32  
33  
34  
35 Boucher, O., Randall, D., Artaxo, P., Bretherton, C., Feingold, G., Forster, P.M.,  
36 Kerminen, V.-M., Kondo, Y., Liao, H., Lohmann, U., Rasch, P., Satheesh, S.K.,  
37 Sherwood, S., Stevens, B., Zhang, X.Y., 2013. Clouds and Aerosols, in: *Climate*  
38 *Change 2013: The Physical Science Basis.*, in: *Contribution of Working Group I*  
39 *to the Fifth Assessment Report of the Intergovernmental Panel on Climate*  
40 *Change.* Cambridge University Press.  
41  
42  
43  
44  
45 Bréon, F.-M., Tanré, D., Generoso, S., 2002. Aerosol Effect on Cloud Droplet Size  
46 Monitored from Satellite. *Science* 295, 834–838.  
47 <https://doi.org/10.1126/science.1066434>  
48  
49  
50 Chang, H., Charalampopoulos, T.T., 1990. Determination of the wavelength  
51 dependence of refractive indices of flame soot. *Proc R Soc Lond A* 430, 577–  
52 591. <https://doi.org/10.1098/rspa.1990.0107>  
53  
54  
55  
56 Charlson, R.J., Schwartz, S.E., Hales, J.M., Cess, R.D., Coakley, J.A., Hansen, J.E.,  
57 Hofmann, D.J., 1992. Climate Forcing by Anthropogenic Aerosols. *Science* 255,  
58 423–430. <https://doi.org/10.1126/science.255.5043.423>  
59  
60

- 1  
2  
3 Collaud Coen, M., Weingartner, E., Apituley, A., Ceburnis, D., Fierz-Schmidhauser, R.,  
4 Flentje, H., Henzing, J.S., Jennings, S.G., Moerman, M., Petzold, A., others,  
5 2010. Minimizing light absorption measurement artifacts of the Aethalometer:  
6 evaluation of five correction algorithms. *Atmospheric Meas. Tech.* 3, 457–474.  
7  
8 Fuzzi, S., Andreae, M.O., Huebert, B.J., Kulmala, M., Bond, T.C., Boy, M., Doherty,  
9 S.J., Guenther, A., Kanakidou, M., Kawamura, K., 2006. Critical assessment of  
10 the current state of scientific knowledge, terminology, and research needs  
11 concerning the role of organic aerosols in the atmosphere, climate, and global  
12 change. *Atmospheric Chem. Phys.* 6, 2017–2038.  
13  
14 Herbin, H., Pujol, O., Hubert, P., Petitprez, D., 2017. New approach for the  
15 determination of aerosol refractive indices – Part I: Theoretical bases and  
16 numerical methodology. *J. Quant. Spectrosc. Radiat. Transf.* 200, 311–319.  
17 <https://doi.org/10.1016/j.jqsrt.2017.03.005>  
18  
19 Hubert, P., Herbin, H., Visez, N., Pujol, O., Petitprez, D., 2017. New approach for the  
20 determination of aerosol refractive indices – Part II: Experimental set-up and  
21 application to amorphous silica particles. *J. Quant. Spectrosc. Radiat. Transf.*  
22 200, 320–327. <https://doi.org/10.1016/j.jqsrt.2017.03.037>  
23  
24 Koch, D., Schulz, M., Kinne, S., McNaughton, C., Spackman, J.R., Balkanski, Y.,  
25 Bauer, S., Berntsen, T., Bond, T.C., Boucher, O., 2009. Evaluation of black  
26 carbon estimations in global aerosol models. *Atmospheric Chem. Phys.* 9, 9001–  
27 9026.  
28  
29 Kostenidou, E., Pathak, R.K., Pandis, S.N., 2007. An Algorithm for the Calculation of  
30 Secondary Organic Aerosol Density Combining AMS and SMPS Data. *Aerosol*  
31 *Sci. Technol.* 41, 1002–1010. <https://doi.org/10.1080/02786820701666270>  
32  
33 Malloy, Q.G.J., Nakao, S., Qi, L., Austin, R., Stothers, C., Hagino, H., Cocker, D.R.,  
34 2009. Real-Time Aerosol Density Determination Utilizing a Modified Scanning  
35 Mobility Particle Sizer—Aerosol Particle Mass Analyzer System. *Aerosol Sci.*  
36 *Technol.* 43, 673–678. <https://doi.org/10.1080/02786820902832960>  
37  
38 McConnell, C.L., Formenti, P., Highwood, E.J., Harrison, M.A.J., 2010. Using aircraft  
39 measurements to determine the refractive index of Saharan dust during the  
40 DODO Experiments. *Atmospheric Chem. Phys.* 10, 3081–3098.  
41  
42 McMurry, P.H., Wang, X., Park, K., Ehara, K., 2002. The Relationship between Mass  
43 and Mobility for Atmospheric Particles: A New Technique for Measuring  
44  
45  
46  
47  
48  
49  
50  
51  
52  
53  
54  
55  
56  
57  
58  
59  
60

- 1  
2  
3 Particle Density. *Aerosol Sci. Technol.* 36, 227–238.  
4 <https://doi.org/10.1080/027868202753504083>  
5  
6  
7 Moise, T., Flores, J.M., Rudich, Y., 2015. Optical Properties of Secondary Organic  
8 Aerosols and Their Changes by Chemical Processes. *Chem. Rev.* 115, 4400–  
9 4439. <https://doi.org/10.1021/cr5005259>  
10  
11  
12 Müller, T., Laborde, M., Kassell, G., Wiedensohler, A., 2011. Design and performance  
13 of a three-wavelength LED-based total scatter and backscatter integrating  
14 nephelometer. *Atmos Meas Tech* 4, 1291–1303. [https://doi.org/10.5194/amt-4-](https://doi.org/10.5194/amt-4-1291-2011)  
15 [1291-2011](https://doi.org/10.5194/amt-4-1291-2011)  
16  
17  
18 Myhre, G., Samset, B.H., Schulz, M., Balkanski, Y., Bauer, S., Berntsen, T.K., Bian,  
19 H., Bellouin, N., Chin, M., Diehl, T., Easter, R.C., Feichter, J., Ghan, S.J.,  
20 Hauglustaine, D., Iversen, T., Kinne, S., Kirkevåg, A., Lamarque, J.-F., Lin, G.,  
21 Liu, X., Lund, M.T., Luo, G., Ma, X., Noije, T.V., Penner, J.E., Rasch, P.J.,  
22 Ruiz, A., Seland, Ø., Skeie, R.B., Stier, P., Takemura, T., Tsigaridis, K., Wang,  
23 P., Wang, Z., Xu, L., Yu, H., Yu, F., Yoon, J.-H., Zhang, K., Zhang, H., Zhou,  
24 C., 2013. Radiative Forcing of the Direct Aerosol Effect from AeroCom Phase II  
25 Simulations. *Atmospheric Chem. Phys.* 1853–1877. [https://doi.org/10.5194/acp-](https://doi.org/10.5194/acp-13-1853-2013)  
26 [13-1853-2013](https://doi.org/10.5194/acp-13-1853-2013)  
27  
28  
29  
30  
31  
32  
33  
34 Ramanathan, V., Crutzen, P.J., Kiehl, J.T., Rosenfeld, D., 2001. Aerosols, Climate, and  
35 the Hydrological Cycle. *Science* 294, 2119–2124.  
36 <https://doi.org/10.1126/science.1064034>  
37  
38  
39  
40 Reed, B.E., Peters, D.M., McPheat, R., Grainger, R.G., 2018. The Complex Refractive  
41 Index of Volcanic Ash Aerosol Retrieved From Spectral Mass Extinction. *J.*  
42 *Geophys. Res. Atmospheres* 123, 1339–1350.  
43 <https://doi.org/10.1002/2017JD027362>  
44  
45  
46  
47 Rosenfeld, D., Lohmann, U., Raga, G.B., O'Dowd, C.D., Kulmala, M., Fuzzi, S.,  
48 Reissell, A., Andreae, M.O., 2008. Flood or Drought: How Do Aerosols Affect  
49 Precipitation? *Science* 321, 1309–1313. <https://doi.org/10.1126/science.1160606>  
50  
51  
52 Schuster, G.L., 2005. Inferring black carbon content and specific absorption from  
53 Aerosol Robotic Network (AERONET) aerosol retrievals. *J. Geophys. Res.* 110.  
54 <https://doi.org/10.1029/2004JD004548>  
55  
56  
57 Schuster, G.L., Dubovik, O., Arola, A., 2015. Remote sensing of soot carbon—Part 1:  
58 Distinguishing different absorbing aerosol species. *Atmospheric Chem. Phys.*  
59 *Discuss.* 15.  
60

1  
2  
3  
4  
5  
6  
7  
8  
9  
10  
11  
12  
13  
14  
15  
16  
17  
18  
19  
20  
21  
22  
23  
24  
25  
26  
27  
28  
29  
30  
31  
32  
33  
34  
35  
36  
37  
38  
39  
40  
41  
42  
43  
44  
45  
46  
47  
48  
49  
50  
51  
52  
53  
54  
55  
56  
57  
58  
59  
60

Schuster, G.L., Lin, B., Dubovik, O., 2009. Remote sensing of aerosol water uptake. *Geophys. Res. Lett.* 36, L03814. <https://doi.org/10.1029/2008GL036576>

Stocker, T.F., Qin, D., Plattner, G.K., M. Tignor, S. K. Allen, J. Boschung, A. Nauels, Y. Xia, V. Bex, and P. M. Midgley, 2013. The Physical Science Basis. Contribution of Working Group I to the Fifth Assessment Report of the Intergovernmental Panel on Climate Change.

Wang, X., Heald, C.L., Sedlacek, A.J., de Sá, S.S., Martin, S.T., Alexander, M.L., Watson, T.B., Aiken, A.C., Springston, S.R., Artaxo, P., 2016. Deriving brown carbon from multiwavelength absorption measurements: method and application to AERONET and Aethalometer observations. *Atmos Chem Phys* 16, 12733–12752. <https://doi.org/10.5194/acp-16-12733-2016>

Table 1 : Refractive indexes retrieved, at three wavelengths (450, 525 and 635nm), by both High spectral resolution (HR) extinction and conventional optical (CO) in-situ methods based on known size distribution and Mie generated optical (extinction, absorption and scattering) coefficients. The reference corresponds to the CRI used to calculate optical coefficients.

Aerosol type	Method	Real Part			Imaginary Part		
		450 nm	525 nm	635nm	450 nm	525 nm	635nm
Dust like	Reference	1.444	1.4455	1.4450	$7.8e^{-5}$	$12.4e^{-5}$	$21.9e^{-5}$
	HR	1.441	1.446	1.444	$7.8e^{-5}$	$12.4e^{-5}$	$21.9e^{-5}$
	$\Delta_{\text{ref-HR}}$	0.2%	0.03%	0.07%	0%	0%	0%
	RO	1.460	1.453	1.449	$10.0e^{-5}$	$10.0e^{-5}$	$20.0e^{-5}$
	$\Delta_{\text{ref-CV}}$	1.1%	0.5%	0.3%	28%	19%	8%
BC like	Reference	1.706	1.730	1.759	0.639	0.604	0.575
	HR	1.731	1.755	1.778	0.626	0.585	0.553
	$\Delta_{\text{ref-HR}}$	1.4%	1.4%	1.0%	2.0%	3.1%	3.8%
	RO	1.699	1.725	1.756	0.594	0.576	0.560
	$\Delta_{\text{ref-CV}}$	0.4%	0.3%	0.1%	7.0%	4.6%	2.5%

Table 2 : Refractive indexes retrieved by the High spectral resolution (HR) extinction method and conventional optical (CO) in-situ method with the associated errors for spherical SiO<sub>2</sub> particles (500nm).

	<b>n</b>	<b>k</b>
SiO <sub>2</sub> (data from dealer)	1.38 - 1.46	Not given
HR method	1.443 ± 0.019	5.8 e-4 ± 6 e-6
CO method	1.448 ± 0.008	26 e-4 ± 1 e-4

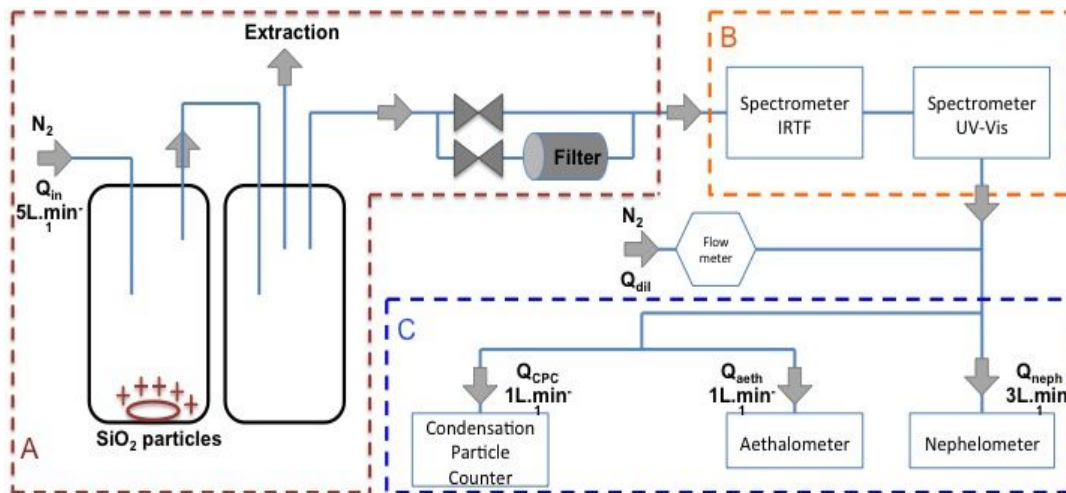


Figure 1: Experimental set up composed of (A) an aerosol generation system, (B) high spectral resolution spectrometers measuring within a broadband range of wavelength (from UV to IR) and (C) conventional optical in-situ measurements measuring within the visible range.

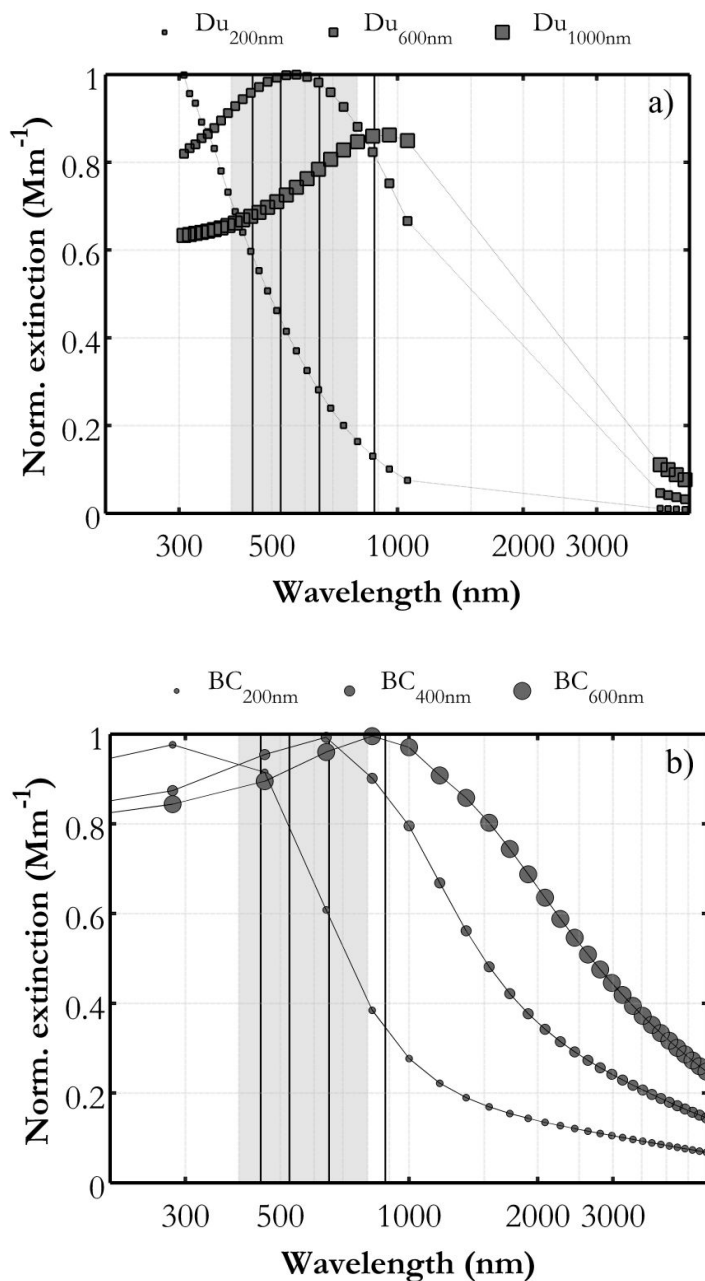


Figure 2: Mie calculated and normalized extinction for (a) dust like particles at three diameters (200nm, 600nm, 1000nm) and (b) BC like particles at three diameters (200nm, 400nm, 600nm) as a function of wavelengths. Grey area represents the 400nm to 800nm corresponding to the visible range. Black lines represent the nephelometer wavelengths (450, 525, 650 nm) and the aethalometer wavelength (880nm). The Dust-like particle CRI is not given within the literature from 1057nm to 4255nm. Therefore, the extinction was not calculated.

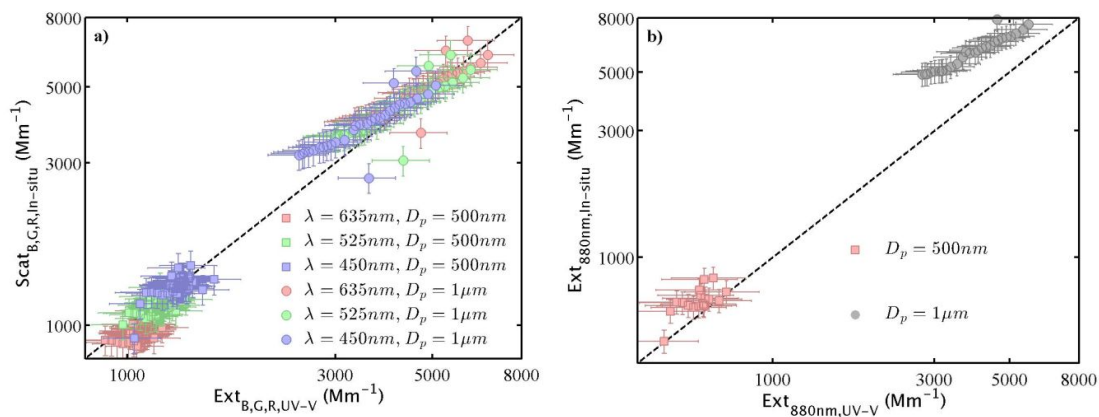


Figure 3: a) Scattering coefficients measured using the nephelometer as a function of the extinction coefficients measured using UV-Visible spectrometer at 450, 525, and 635 nm for spherical SiO<sub>2</sub> particles with diameter of 500 nm (squares) and 1  $\mu$ m (dots). b) Extinction coefficients calculated from extrapolated to 880nm scattering and absorption coefficients and as a function of the extinction coefficients measured by UV-Visible spectrometer at 880nm for spherical SiO<sub>2</sub> particles with diameter of 500 nm (squares) and 1  $\mu$ m (dots).



---

# List of Figures

---

1	Annual mean top of the atmospheric radiative forcing of aerosol-radiation interactions due to different anthropogenic aerosol types, for the 1750-2010 period. Hatched whisker boxes show median (line), 5th to 95th percentiles (box) and min/max values (whiskers) from AeroCom II models Myhre et al. (2013a). Solid colour boxes show the AR5 (Fifth Assessment Report) best estimates and 90% uncertainty ranges. BC FF represents black carbon from fossil fuel and biofuel; POA FF, primary organic aerosol from fossil fuel and biofuel; BB, aerosols from biomass burning; SOA, secondary organic aerosols from Boucher et al. (2013). . . . .	16
2	Diurnal variation of the relative humidity measured by the DAVIS meteo station and inside the nephelometer at the roof top of LOA for 2015-2016. . . . .	19
1.1	Description and process of formation of multimodal particle size distribution with typical transformations. From Finlayson-Pitts and Hemminger (2000). . . . .	31
1.2	Particle size distribution in number, in surface area, and in volume of the same aerosol population (Seinfeld and Pandis, 1998), $n_N^{\circ}$ , $n_S^{\circ}$ , $n_V^{\circ}$ represent respectively, $n_N(\log D_p)$ , $n_S(\log D_p)$ , and $n_V(\log D_p)$ . . . . .	33
1.3	Pie charts of the average mass concentration and chemical composition of NR-PM1 (non refractive particulate matter of diameter less than 1 micron) derived from AMS (Aerosol Mass Spectrometer) datasets: organics (green), sulfate (red), nitrate (blue), ammonium (orange), and chloride (purple). From Zhang et al. (2007). . . . .	34
1.4	Mechanisms of interaction between incident electromagnetic radiation and aerosol population. . . . .	37

1.5	Köhler curve for $NaCl$ (solid lines) and $(NH_4)_2SO_4$ (dashed lines) with dry diameters of 0.05, 0.1, et 0.5 $\mu m$ at 293 K. Source: Seinfeld and Pandis (1998).	41
1.6	Schematic of particle diameter or scattering evolution as a function of RH. The deliquescence branch show the phenomenon that occurs by humidifying particles. . . . .	43
1.7	Schematic of particle diameter or scattering evolution as a function of RH. The deliquescence (blue curve) and efflorescence (red curve) branches show the hysteresis phenomenon that occurs by humidifying and drying particles.	44
1.8	Deliquescence diagram of $NH_4NO_3/NH_4Cl$ mixture. A, B, C and D correspond to the four main regimes (see text for more details). The water activity at saturation is represented as a function of $NH_4NO_3$ fraction in the mixing. Red lines (black) correspond to the MDRH (DRH). Source: Seinfeld and Pandis (2006) with some extra notions. . . . .	46
1.9	Optical images of a single levitated $NaN_3$ particle undergoing humidifying process (Seng et al., 2018a). . . . .	48
1.10	Variation of the scattering coefficient at $\lambda=525nm$ as a function of the relative humidity for sea salt aerosols (blue curve) and insoluble aerosols (black curve) using the software package OPAC (Optical Properties of Aerosols and Clouds).	50
1.11	Variation of number of moles of $H_2O$ with the relative humidity for $NaCl/(NH_4)_2SO_4$ mixture containing 20% of NaCl calculated using E-AIM. The MDRH and the DRH are represented by the light blue dots. . . . .	52
2.1	Experimental setup used to measure aerosol optical and physical properties at variable relative humidity. . . . .	61
2.2	WELAS operating diagram (Palas 2300) (Source:Wikipedia). . . . .	64
2.3	Variation of the diameter and the number concentration of sodium chloride in the WELAS. . . . .	64
2.4	Operating diagram of the nephelometer (Aurora 3000).(Adapted from: Müller et al. (2011)) . . . . .	66

2.5	Scattering coefficient measured at 525 nm by the nephelometer as a function of the PM <sub>10</sub> of aerosol particles with a diameter <10 μm measured by the OPC (GRIMM Mini-WRAS) for three different aerosol types. . . . .	67
2.6	Humidogram representing the variation of the scattering coefficient as a function of the relative humidity for sodium chloride particles generated by atomization. The blue, green and red curves correspond to 450, 525 and 630 nm wavelengths respectively. . . . .	68
2.7	Photo of the experimental levitation device coupled to the Raman microscope.	70
2.8	Optical image of sodium chloride particle levitated in air at different relative humidities. . . . .	71
2.9	Principle of Raman scattering (Source: Barbillat et al. (1999)). . . . .	72
2.10	Raman scattering spectrum Stokes and anti-Stokes of calcite, λ <sub>ex</sub> = 632 nm.	73
2.11	Raman spectra of CaF <sub>2</sub> substrate obtained with HeNe laser light at 633 nm.	74
3.1	Variation of the scattering enhancement factor as a function of relative humidity for sodium chloride (a), ammonium sulfate (b), potassium chloride (c) and sodium nitrate (d). The light blue dots represent the deliquescence relative humidity for each component. Sodium nitrate shows no DRH (see text for more details). . . . .	80
3.2	Optical images of an ammonium sulfate ((NH <sub>4</sub> ) <sub>2</sub> SO <sub>4</sub> ) particle levitated in air during humidifying process. The images with red and green borders represent the dried particle and the particle at the DRH respectively. . . . .	82
3.3	Variation of the diameter (y axis) and the number concentration (colorbar) of aerosol particles as a function of relative humidity for sodium chloride (a), ammonium sulfate (b), potassium chloride (c) and sodium nitrate (d). . . . .	85
3.4	Averaged size distributions of NaCl aerosol particles measured for dry (<60%) and wet (>75%) conditions. . . . .	86

3.5	Hygroscopic growth factors retrieved from the scattering enhancement factor for an aerosol population (red) and measured from the optical images provided by the optical microscope of the levitation setup for a single particle (black) for sodium chloride (a) and ammonium sulfate (b) aerosols. . . . .	88
4.1	Variation of the scattering enhancement factor with the relative humidity for NaCl/KCl mixture containing 56% of NaCl and 44% of KCl (blue curve) and for pure components (NaCl: grey, KCl: black) that compose this mixture obtained directly from measurements (a) and averaged over a window of 10% RH (b). The DRH is represented by the light blue dots in figure a. . . . .	95
4.2	DRH variation of NaCl/KCl with the different molar fractions of NaCl obtained during this study (red dot) and based on literature data (black dots). Sources: Tang (2000); Li et al. (2014); Tang and Munkelwitz (1993) . . . . .	96
4.3	Comparison of the growth factor retrieved from optical measurements (scattering enhancement factor) and predicted using the ZSR method for the NaCl/KCl mixture ( $X_{NaCl} = 0.56$ ). . . . .	97
4.4	Variation of the scattering enhancement factor as a function of the relative humidity for <i>NaCl/NaNO<sub>3</sub></i> mixture containing 0 (black), 26 (red), 49 (blue), 68 (yellow), 85 (green), 100% (grey) of NaCl. . . . .	98
4.5	DRH variation of <i>NaCl/NaNO<sub>3</sub></i> as a function of NaCl molar fractions obtained during this study (black dots, dashed line) and DRH and MDRH values calculated using E-AIM (red and black lines) . . . . .	99
4.6	Comparison of the growth factor retrieved from optical measurements (scattering enhancement factor) (colored curves) and predicted using the ZSR method (black curves) for 26 (a), 49 (b), 68 (c), 85 (d) % of NaCl in <i>NaCl/NaNO<sub>3</sub></i> mixture. . . . .	101
4.7	Variation of the measured scattering enhancement factor as a function of the relative humidity for NaCl/( <i>NH<sub>4</sub></i> ) <sub>2</sub> <i>SO<sub>4</sub></i> mixture containing 0 (black), 36 (red), 60 (blue), 77 (yellow), 89 (green), 100% (grey) of NaCl. . . . .	104

4.8	DRH <sub>mixture</sub> variation of $NaCl/(NH_4)_2SO_4$ with the different molar fractions of NaCl obtained during this study (black curve) and DRH <sub>mixture</sub> variation of $(NH_4)_2SO_4/Na_2SO_4$ molar fractions of $Na^+$ obtained by Rood et al. (1985) (red curve). . . . .	105
4.9	Comparison of the growth factor retrieved from optical measurements (scattering enhancement factor) (colored curves) and predicted using the ZSR method (black curves) for 36 (a), 60 (b), 77 (c), 89 (d) % of NaCl in $NaCl/(NH_4)_2SO_4$ mixture. . . . .	106
5.1	Optical images of $NaCl/(NH_4)_2SO_4$ particle levitated in air during the humidifying process for $X_{NaCl}=0.36$ (a), $X_{NaCl}=0.60$ (b), $X_{NaCl}=0.77$ (c) and $X_{NaCl}=0.89$ (d). The images with red, blue and green borders represent the dried particle, the particle at the MDRH and at the DRH, respectively. . . .	113
5.2	Variation of the growth factor measured from the images of the optical microscope with the relative humidity for 36 (a), 60 (b), 77 (c), 89 (d) % of NaCl in $NaCl/(NH_4)_2SO_4$ mixture (colored curves) in comparison to pure aerosols (NaCl: grey, $(NH_4)_2SO_4$ : black). . . . .	115
5.3	Evolution of the MDRH (black) and the DRH (red) as a function of the NaCl fraction in the $NaCl/(NH_4)_2SO_4$ mixture. The lines correspond to simulation results (E-AIM) while forcing it to prevent the formation of new solids. Dots correspond to the experimental results. A, B, C and D correspond to the four main regimes (see text for more details). . . . .	117
5.4	Evolution of the MDRH (black) and the DRH (red) as a function of the NaCl fraction in the $NaCl/(NH_4)_2SO_4$ mixture. The lines correspond to simulation results (E-AIM) without forcing it to prevent the formation of new solids. Dots correspond to the experimental results. A, B, C and D correspond to the four main regimes (see text for more details). . . . .	119

5.5	Raman spectra of a droplet initially containing 36% of $NaCl$ and 64% of $(NH_4)_2SO_4$ obtained with HeNe laser light at 633 nm at RH=20% (a), and at RH=69% (c). (b) and (d) represent enlarged views of 900-1200 $cm^{-1}$ spectral range of (a) and (c), respectively. . . . .	121
5.6	Raman spectra of a droplet initially containing 60% of $NaCl$ and 40% of $(NH_4)_2SO_4$ obtained with HeNe laser light at 633 nm at RH=20% (a), and at RH=70% (c). (b) and (d) represent enlarged views of 900-1200 $cm^{-1}$ spectral range of (a) and (c), respectively. . . . .	123
5.7	Evolution of the MDRH (black) and the DRH (red) as a function of the NaCl (a,b) and $(NH_4)_2SO_4$ (c,d) fraction in $NaCl/Na_2SO_4$ (a), $NaCl/NH_4Cl$ (b) $(NH_4)_2SO_4/Na_2SO_4$ (c) and $(NH_4)_2SO_4/NH_4Cl$ (d) mixing. The lines correspond to simulation results (E-AIM) while forcing it to prevent the formation of new solids. A, B, C and D correspond to the four main regimes. . .	125
5.8	Acoustic pressure role in the levitation phenomenon of particles. . . . .	139
5.9	Raman spectra of solid $NH_4Cl$ obtained with HeNe laser light at 633 nm . .	141
5.10	Deliquescence diagram of $NaCl/NaNO_3$ built using E-AIM. Black and red lines indicate theoretical MDRH (67.9%) and DRH, respectively. . . . .	141
5.11	Variation of particle liquid water content with the relative humidity for sodium chloride (a), ammonium sulfate (b), potassium chloride (c) and sodium nitrate (d). The blue curves represent results based on the nephelometer measurements and the red curves the calculation made using ISORROPIA-II. . . . .	144

---

# List of Tables

---

1	<i>Hygroscopic growth factors from the literature measured for different aerosol types. The values of <math>f(RH)</math> correspond to the ratio of the aerosol light-scattering coefficient (near 550 nm wavelength) at high RH and at dry conditions (<math>RH &lt; 40\%</math>). From Titos et al. (2014).</i> . . . . .	21
1.1	<i>Approximate emission of aerosol particles flux in Tg/year. <math>T_g = 10^{12}g</math>, C=Carbon, S=Sulfur, N=Nitrogen (Boucher, 2015).</i> . . . . .	30
1.2	<i>Deliquescence and efflorescence relative humidities of electrolyte solutions at 298 K. Sources: Tang (1996b); Tang and Munkelwitz (1993, 1994a); Martin (2000)</i> . . . . .	44
1.3	<i>Growth factors measured using a HTDMA or calculated using thermodynamic models for some main aerosol species or types of 100 nm diameter.</i> . . . . .	48
3.1	<i>Parameters of synthetic aerosol particles used in the laboratory experiments.</i>	79
3.2	<i>Results of the deliquescence relative humidities of synthetic aerosol particles measured and calculated in comparison with literature data. The method used in the literature are based on HTDMA for NaCl, <math>(NH_4)_2SO_4</math> and KCl and on optical microscopy for <math>NaNO_3</math>.</i> . . . . .	82
3.3	<i>Hygroscopic growth factor retrieved and measured at the deliquescence relative humidity of each component and comparison to literature data.</i> . . . . .	89
5.1	<i>MDRH and DRH values for NaCl/<math>(NH_4)_2SO_4</math> mixture obtained from the humidograms based on the optical images.</i> . . . . .	114

---

## List of abbreviations

---

- **LOA:** Laboratoire d'Optique Atmosphérique
- **LASIR:** Laboratoire de Spectrochimie Infrarouge et Raman
- **PC2A:** PhysicoChimie des Processus de Combustion et de l'Atmosphère
- **OPC:** Optical Particle Counter
- **PM:** Particle Matter
- **RH:** Relative Humidity
- **DRH:** Deliquescence Relative Humidity
- **ERH:** Efflorescence Relative Humidity
- **MDRH:** Mutual Deliquescence Relative Humidity
- **ALWC:** Aerosol Liquid Water Content
- **IS:** In Situ
- **HR:** High Resolution
- **UV:** UltraViolet
- **MSE:** Mass Scattering Efficiency

---

## Bibliography

---

- Adam, M., Putaud, J., Martins dos Santos, S., Dell'Acqua, A., and Gruening, C. (2012). Aerosol hygroscopicity at a regional background site (Ispra) in Northern Italy. *Atmospheric Chemistry and Physics*, 12(13):5703–5717.
- Adler, G., Koop, T., Haspel, C., Taraniuk, I., Moise, T., Koren, I., Heiblum, R. H., and Rudich, Y. (2013). Formation of highly porous aerosol particles by atmospheric freeze-drying in ice clouds. *Proceedings of the National Academy of Sciences*, 110(51):20414–20419.
- Ahn, K.-H., Kim, S.-M., Jung, H.-J., Lee, M.-J., Eom, H.-J., Maskey, S., and Ro, C.-U. (2010). Combined use of optical and electron microscopic techniques for the measurement of hygroscopic property, chemical composition, and morphology of individual aerosol particles. *Analytical chemistry*, 82(19):7999–8009.
- Albrecht, B. A. (1989). Aerosols, cloud microphysics, and fractional cloudiness. *Science*, 245(4923):1227–1230.
- Alshawa, A., Dopfer, O., Harmon, C. W., Nizkorodov, S. A., and Underwood, J. S. (2009). Hygroscopic growth and deliquescence of nacl nanoparticles coated with surfactant aot. *The Journal of Physical Chemistry A*, 113(26):7678–7686.
- Barbillat, J., Bougeard, D., Buntinx, G., Delhaye, M., and Fillaux, F. (1999). Spectrométrie Raman, techniques de l'ingénieur-traité analyse et caractérisation.
- Ben Mabrouk, K., Kauffmann, T. H., Aroui, H., and Fontana, M. D. (2013). Raman study of cation effect on sulfate vibration modes in solid state and in aqueous solutions. *Journal of Raman Spectroscopy*, 44(11):1603–1608.

- Bergstrom, R. W. and Russell, P. (1999). Estimation of aerosol direct radiative effects over the mid-latitude North Atlantic from satellite and in situ measurements. *Geophysical research letters*, 26(12):1731–1734.
- Beuttell, R. G. and Brewer, A. W. (1949). Instruments for the Measurement of the Visual Range. *Journal of Scientific Instruments*, 26:357–359.
- Bohren, C. F. and Huffman, D. R. (2008). *Absorption and scattering of light by small particles*. John Wiley & Sons.
- Bond, T. C., Habib, G., and Bergstrom, R. W. (2006). Limitations in the enhancement of visible light absorption due to mixing state. *Journal of Geophysical Research: Atmospheres*, 111(D20).
- Boucher, O. (2015). *Atmospheric aerosols: Properties and climate impacts*. Springer.
- Boucher, O., Randall, D., Artaxo, P., Bretherton, C., Feingold, G., Forster, P., Kerminen, V.-M., Kondo, Y., Liao, H., Lohmann, U., et al. (2013). Clouds and aerosols. In *Climate change 2013: the physical science basis. Contribution of Working Group I to the Fifth Assessment Report of the Intergovernmental Panel on Climate Change*, pages 571–657. Cambridge University Press.
- Bougiatioti, A., Nikolaou, P., Stavroulas, I., Kouvarakis, G., Weber, R., Nenes, A., Kanakidou, M., and Mihalopoulos, N. (2016). Particle water and pH in the eastern Mediterranean: source variability and implications for nutrient availability. *Atmospheric Chemistry and Physics*, 16(7):4579–4591.
- Brandt, E. (2001). Acoustic physics: suspended by sound. *Nature*, 413(6855):474.
- Cabada, J. C., Pandis, S. N., Subramanian, R., Robinson, A. L., Polidori, A., and Turpin, B. (2004). Estimating the secondary organic aerosol contribution to PM<sub>2.5</sub> using the EC tracer method special issue of aerosol science and technology on findings from the fine particulate matter supersites program. *Aerosol Science and Technology*, 38(S1):140–155.

- Carrico, C., Petters, M., Kreidenweis, S., Sullivan, A., McMeecking, G., Levin, E., Engling, G., Malm, W., and Collett Jr, J. (2010). Water uptake and chemical composition of fresh aerosols generated in open burning of biomass. *Atmospheric Chemistry and Physics*, 10(11):5165–5178.
- Carrico, C. M., Rood, M. J., and Ogren, J. A. (1998). Aerosol light scattering properties at Cape Grim, Tasmania, during the first aerosol characterization experiment (ACE 1). *Journal of Geophysical Research: Atmospheres*, 103(D13):16565–16574.
- Chan, M. N. and Chan, C. K. (2003). Hygroscopic properties of two model Humic-like substances and their mixtures with inorganics of atmospheric importance. *Environmental science & technology*, 37(22):5109–5115.
- Chang, S.-Y. and Lee, C.-T. (2002). Applying GC-TCD to investigate the hygroscopic characteristics of mixed aerosols. *Atmospheric Environment*, 36(9):1521–1530.
- Chen, J., Zhao, C., Ma, N., and Yan, P. (2014). Aerosol hygroscopicity parameter derived from the light scattering enhancement factor measurements in the North China Plain. *Atmospheric Chemistry and Physics*, 14(15):8105–8118.
- Cheng, Y., Wiedensohler, A., Eichler, H., Heintzenberg, J., Tesche, M., Ansmann, A., Wendisch, M., Su, H., Althausen, D., Herrmann, H., et al. (2008). Relative humidity dependence of aerosol optical properties and direct radiative forcing in the surface boundary layer at Xinken in Pearl River Delta of China: An observation based numerical study. *Atmospheric Environment*, 42(25):6373–6397.
- Chi, J., Li, W., Zhang, D., Zhang, J., Lin, Y., Shen, X., Sun, J., Chen, J., Zhang, X., Zhang, Y., et al. (2015). Sea salt aerosols as a reactive surface for inorganic and organic acidic gases in the arctic troposphere. *Atmospheric Chemistry and Physics*, 15(19):11341.
- Choi, M. Y. and Chan, C. K. (2002). The effects of organic species on the hygroscopic behaviors of inorganic aerosols. *Environmental science & technology*, 36(11):2422–2428.

- Clegg, S. L., Brimblecombe, P., and Wexler, A. S. (1998). Thermodynamic model of the system  $\text{H}^+ - \text{NH}_4^+ - \text{SO}_4^{2-} - \text{NO}_3^- - \text{H}_2\text{O}$  at tropospheric temperatures. *The Journal of Physical Chemistry A*, 102(12):2137–2154.
- Clegg, S. L. and Seinfeld, J. H. (2004). Improvement of the Zdanovskii- Stokes- Robinson model for mixtures containing solutes of different charge types. *The Journal of Physical Chemistry A*, 108(6):1008–1017.
- Cohen, M. D., Flagan, R. C., and Seinfeld, J. H. (1987). Studies of concentrated electrolyte solutions using the electrodynamic balance. 2. water activities for mixed-electrolyte solutions. *Journal of Physical Chemistry*, 91(17):4575–4582.
- Collaud Coen, M., Andrews, E., Asmi, A., Baltensperger, U., Bukowiecki, N., Day, D., Fiebig, M., Fjæraa, A. M., Flentje, H., Hyvärinen, A., et al. (2013). Aerosol decadal trends—part 1: In-situ optical measurements at GAW and IMPROVE stations. *Atmospheric Chemistry and Physics*, 13(2):869–894.
- Cotterell, M. I., Mason, B. J., Preston, T. C., Orr-Ewing, A. J., and Reid, J. P. (2015). Optical extinction efficiency measurements on fine and accumulation mode aerosol using single particle cavity ring-down spectroscopy. *Physical Chemistry Chemical Physics*, 17(24):15843–15856.
- Covert, D. S., Charlson, R., and Ahlquist, N. (1972). A study of the relationship of chemical composition and humidity to light scattering by aerosols. *Journal of Applied Meteorology*, 11(6):968–976.
- Crumeyrolle, S., Chen, G., Ziemba, L., Beyersdorf, A., Thornhill, L., Winstead, E., Moore, R., Shook, M., Hudgins, C., and Anderson, B. (2014). Factors that influence surface PM<sub>2.5</sub> values inferred from satellite observations: Perspective gained for the US Baltimore–Washington metropolitan area during DISCOVER-AQ. *Atmospheric Chemistry and Physics*, 14(4):2139–2153.

- Cruz, C. N. and Pandis, S. N. (2000). Deliquescence and hygroscopic growth of mixed inorganic-organic atmospheric aerosol. *Environmental Science & Technology*, 34(20):4313–4319.
- Delmas, R., Megie, G., and Peuch, V. (2005). Atmosphere physics and chemistry.
- Denjean, C., Formenti, P., Picquet-Varrault, B., Katrib, Y., Pangui, E., Zapf, P., and Doussin, J. (2014). A new experimental approach to study the hygroscopic and optical properties of aerosols: application to ammonium sulfate particles. *Atmospheric Measurement Techniques*, 7(1):183–197.
- Dong, J.-L., Li, X.-H., Zhao, L.-J., Xiao, H.-S., Wang, F., Guo, X., and Zhang, Y.-H. (2007). Raman observation of the interactions between  $\text{NH}_4^+$ ,  $\text{SO}_4^{2-}$ , and  $\text{H}_2\text{O}$  in supersaturated  $(\text{NH}_4)_2\text{SO}_4$  droplets. *The Journal of Physical Chemistry B*, 111(42):12170–12176.
- Dubovik, O., Holben, B., Eck, T. F., Smirnov, A., Kaufman, Y. J., King, M. D., Tanré, D., and Slutsker, I. (2002). Variability of absorption and optical properties of key aerosol types observed in worldwide locations. *Journal of the atmospheric sciences*, 59(3):590–608.
- Erdakos, G. B., Chang, E. I., Pankow, J. F., and Seinfeld, J. H. (2006). Prediction of activity coefficients in liquid aerosol particles containing organic compounds, dissolved inorganic salts, and water—part 3: Organic compounds, water, and ionic constituents by consideration of short-, mid-, and long-range effects using X-UNIFAC.3. *Atmospheric Environment*, 40(33):6437 – 6452.
- Fierz-Schmidhauser, R., Zieger, P., Vaishya, A., Monahan, C., Bialek, J., O’Dowd, C., Jennings, S., Baltensperger, U., and Weingartner, E. (2010a). Light scattering enhancement factors in the marine boundary layer (Mace Head, Ireland). *Journal of Geophysical Research: Atmospheres*, 115(D20).
- Fierz-Schmidhauser, R., Zieger, P., Wehrle, G., Jefferson, A., Ogren, J., Baltensperger,

- U., and Weingartner, E. (2010b). Measurement of relative humidity dependent light scattering of aerosols. *Atmos. Meas. Tech*, 3(1):39–50.
- Finlayson-Pitts, B. J. and Hemminger, J. C. (2000). Physical chemistry of airborne sea salt particles and their components. *The Journal of Physical Chemistry A*, 104(49):11463–11477.
- Fountoukis, C. and Nenes, A. (2007). ISORROPIA II: a computationally efficient thermodynamic equilibrium model for  $K^+$ – $Ca^{2+}$ – $Mg^{2+}$ – $NH_4^+$ – $Na^+$ – $SO_4^{2-}$ – $NO_3^-$ – $Cl^-$ – $H_2O$  aerosols. *Atmospheric Chemistry and Physics*, 7(17):4639–4659.
- Freney, E. J., Martin, S. T., and Buseck, P. R. (2009). Deliquescence and efflorescence of potassium salts relevant to biomass-burning aerosol particles. *Aerosol Science and Technology*, 43(8):799–807.
- Ge, Z., Wexler, A. S., and Johnston, M. V. (1998). Deliquescence behavior of multicomponent aerosols. *The Journal of Physical Chemistry A*, 102(1):173–180.
- Gor’Kov, L. (1962). On the forces acting on a small particle in an acoustical field in an ideal fluid. In *Sov. Phys. Dokl.*, volume 6, pages 773–775.
- Grant, K. E., Chuang, C. C., Grossman, A. S., and Penner, J. E. (1999). Modeling the spectral optical properties of ammonium sulfate and biomass burning aerosols: Parameterization of relative humidity effects and model results. *Atmospheric Environment*, 33(17):2603–2620.
- Guo, H., Xu, L., Bougiatioti, A., Cerully, K. M., Capps, S. L., Hite Jr, J., Carlton, A., Lee, S.-H., Bergin, M., Ng, N., et al. (2015). Fine-particle water and ph in the southeastern United States. *Atmospheric Chemistry & Physics*, 15(9).
- Gupta, D., Kim, H., Park, G., Li, X., Eom, H.-J., and Ro, C.-U. (2015). Hygroscopic properties of NaCl and NaNO<sub>3</sub> mixture particles as reacted inorganic sea-salt aerosol surrogates. *Atmospheric Chemistry and Physics*, 15(6):3379–3393.

- Gysel, M., Weingartner, E., Nyeki, S., Paulsen, D., Baltensperger, U., Galambos, I., and Kiss, G. (2004). Hygroscopic properties of water-soluble matter and humic-like organics in atmospheric fine aerosol. *Atmospheric Chemistry and Physics*, 4(1):35–50.
- Hämeri, K., Laaksonen, A., Väkevä, M., and Suni, T. (2001). Hygroscopic growth of ultrafine sodium chloride particles. *Journal of Geophysical Research: Atmospheres*, 106(D18):20749–20757.
- Hanel, G. and Zankl, B. (1979). Aerosol size and relative humidity: Water uptake by mixtures of salts. *Tellus*, 31(6):478–486.
- Harned, H. and Owen, B. (1958). The physical chemistry of electrolyte solutions, 3rd. *Reinhold, New York*, page 391.
- Haslett, S. L., Taylor, J. W., Deetz, K., Vogel, B., Babić, K., Kalthoff, N., Wieser, A., Dione, C., Lohou, F., Brito, J., et al. (2019). The radiative impact of out-of-cloud aerosol hygroscopic growth during the summer monsoon in southern West Africa. *Atmospheric Chemistry and Physics*, 19(3):1505–1520.
- Hess, M., Koepke, P., and Schult, I. (1998). Optical properties of aerosols and clouds: The software package OPAC. *Bulletin of the American meteorological society*, 79(5):831–844.
- Hewitt, C. N. and Jackson, A. V. (2009). *Atmospheric science for environmental scientists*. John Wiley & Sons.
- Hodzic, A., Jimenez, J. L., Madronich, S., Canagaratna, M., DeCarlo, P. F., Kleinman, L., and Fast, J. (2010). Modeling organic aerosols in a megacity: potential contribution of semi-volatile and intermediate volatility primary organic compounds to secondary organic aerosol formation. *Atmospheric Chemistry & Physics*, 10(12).
- Hoff, R. M. and Christopher, S. A. (2009). Remote sensing of particulate pollution from space: have we reached the promised land? *Journal of the Air & Waste Management Association*, 59(6):645–675.

- Holmgren, H., Sellegri, K., Hervo, M., Rose, C., Freney, E., Villani, P., and Laj, P. (2014). Hygroscopic properties and mixing state of aerosol measured at the high-altitude site Puy de Dôme (1465 m asl), France. *Atmospheric Chemistry and Physics*, 14(18):9537–9554.
- Hu, D., Qiao, L., Chen, J., Ye, X., Yang, X., Cheng, T., and Fang, W. (2010). Hygroscopicity of inorganic aerosols: size and relative humidity effects on the growth factor. *Aerosol Air Qual. Res*, 10:255–264.
- IPCC (2018). IPCC, summary for policymakers. in: Global warming of 1.5°C. an IPCC special report on the impacts of global warming of 1.5°C above pre-industrial levels and related global greenhouse gas emission pathways, in the context of strengthening the global response to the threat of climate change, sustainable development, and efforts to eradicate poverty V. Masson-Delmotte, et al., (eds.). Technical report, World Meteorological Organization, Geneva, Switzerland, 32 pp.
- Ishizaka, S., Yamauchi, K., and Kitamura, N. (2013). In situ quantification of ammonium sulfate in single aerosol droplets by means of laser trapping and raman spectroscopy. *Analytical sciences: the international journal of the Japan Society for Analytical Chemistry*, 29(12):1223.
- Ishizaka, S., Yamauchi, K., and Kitamura, N. (2014). Reversible control of the equilibrium size of a single aerosol droplet by change in relative humidity. *Analytical Sciences*, 30(11):1075–1079.
- Jacobson, M. Z. (2001). Strong radiative heating due to the mixing state of black carbon in atmospheric aerosols. *Nature*, 409(6821):695–697.
- Jaenicke, R. (1993). Chapter 1 tropospheric aerosols. In Hobbs, P. V., editor, *Aerosol–Cloud–Climate Interactions*, volume 54 of *International Geophysics*, pages 1 – 31. Academic Press.

- Jeong, G. Y., Kim, J. Y., Seo, J., Kim, G., Jin, H., and Chun, Y. (2014). Long-range transport of giant particles in Asian dust identified by physical, mineralogical, and meteorological analysis. *Atmospheric Chemistry and Physics*, 14(1):505.
- Jing, B., Peng, C., Wang, Y., Liu, Q., Tong, S., Zhang, Y., and Ge, M. (2017). Hygroscopic properties of potassium chloride and its internal mixtures with organic compounds relevant to biomass burning aerosol particles. *Scientific Reports*, 7.
- Jing, B., Tong, S., Liu, Q., Li, K., Wang, W., Zhang, Y., and Ge, M. (2016). Hygroscopic behavior of multicomponent organic aerosols and their internal mixtures with ammonium sulfate. *Atmospheric Chemistry and Physics*, 16(6):4101–4118.
- Jing, B., Wang, Z., Tan, F., Guo, Y., Tong, S., Wang, W., Zhang, Y., and Ge, M. (2018). Hygroscopic behavior of atmospheric aerosols containing nitrate salts and water-soluble organic acids. *Atmospheric Chemistry and Physics*, 18(7):5115–5127.
- Jordanov, N. and Zellner, R. (2006). Investigations of the hygroscopic properties of ammonium sulfate and mixed ammonium sulfate and glutaric acid micro droplets by means of optical levitation and Raman spectroscopy. *Physical Chemistry Chemical Physics*, 8(23):2759–2764.
- Junge, C. (1963). Sulfur in the atmosphere. *Journal of Geophysical Research*, 68(13):3975–3976.
- Kacenenbogen, M., Léon, J.-F., Chiapello, I., and Tanré, D. (2006). Characterization of aerosol pollution events in France using ground-based and POLDER-2 satellite data. *Atmospheric Chemistry and Physics*, 6(12):4843–4849.
- Kanakidou, M., Seinfeld, J., Pandis, S., Barnes, I., Dentener, F., Facchini, M., Dingenen, R. V., Ervens, B., Nenes, A., Nielsen, C., et al. (2005). Organic aerosol and global climate modelling: a review. *Atmospheric Chemistry and Physics*, 5(4):1053–1123.

- Kim, H., Lee, M.-J., Jung, H.-J., Eom, H.-J., Maskey, S., Ahn, K.-H., and Ro, C.-U. (2012). Hygroscopic behavior of wet dispersed and dry deposited nano<sub>3</sub> particles. *Atmospheric environment*, 60:68–75.
- Kotchenruther, R. A. and Hobbs, P. V. (1998). Humidification factors of aerosols from biomass burning in Brazil. *Journal of Geophysical Research: Atmospheres*, 103(D24):32081–32089.
- Kotchenruther, R. A., Hobbs, P. V., and Hegg, D. A. (1999). Humidification factors for atmospheric aerosols off the mid-Atlantic coast of the United States. *Journal of Geophysical Research: Atmospheres*, 104(D2):2239–2251.
- Krieger, U. K., Marcolli, C., and Reid, J. P. (2012). Exploring the complexity of aerosol particle properties and processes using single particle techniques. *Chemical Society Reviews*, 41(19):6631–6662.
- Laskina, O., Morris, H. S., Grandquist, J. R., Qin, Z., Stone, E. A., Tivanski, A. V., and Grassian, V. H. (2015). Size matters in the water uptake and hygroscopic growth of atmospherically relevant multicomponent aerosol particles. *The Journal of Physical Chemistry A*, 119(19):4489–4497.
- Lee, A. K. and Chan, C. K. (2007). Single particle Raman spectroscopy for investigating atmospheric heterogeneous reactions of organic aerosols. *Atmospheric Environment*, 41(22):4611–4621.
- Lee, A. K., Ling, T., and Chan, C. K. (2008). Understanding hygroscopic growth and phase transformation of aerosols using single particle Raman spectroscopy in an electrodynamic balance. *Faraday discussions*, 137:245–263.
- Lee, C.-T. and Hsu, W.-C. (2000). The measurement of liquid water mass associated with collected hygroscopic particles. *Journal of Aerosol Science*, 31(2):189–197.

- Lesins, G., Chylek, P., and Lohmann, U. (2002). A study of internal and external mixing scenarios and its effect on aerosol optical properties and direct radiative forcing. *Journal of Geophysical Research: Atmospheres*, 107(D10).
- Li, X., Gupta, D., Eom, H.-J., Kim, H., and Ro, C.-U. (2014). Deliquescence and efflorescence behavior of individual NaCl and KCl mixture aerosol particles. *Atmospheric environment*, 82:36–43.
- Ling, T. Y. and Chan, C. K. (2008). Partial crystallization and deliquescence of particles containing ammonium sulfate and dicarboxylic acids. *Journal of Geophysical Research: Atmospheres*, 113(D14).
- Liu, B., Pui, D., Whitby, K., Kittelson, D., Kousaka, Y., and McKenzie, R. (1978). Aerosol mobility chromatograph-New detector for sulfuric-acid aerosols. *Atmospheric Environment (1967)*, 12:99–104.
- Liu, Q., Jing, B., Peng, C., Tong, S., Wang, W., and Ge, M. (2016). Hygroscopicity of internally mixed multi-component aerosol particles of atmospheric relevance. *Atmospheric Environment*, 125:69–77.
- Liu, X., Zhang, Y., Jung, J., Gu, J., Li, Y., Guo, S., Chang, S.-Y., Yue, D., Lin, P., Kim, Y. J., et al. (2009). Research on the hygroscopic properties of aerosols by measurement and modeling during CAREBeijing-2006. *Journal of Geophysical Research: Atmospheres*, 114(D2).
- Liu, X., Zhang, Y., Wen, M., Wang, J., Jung, J., Chang, S.-y., Hu, M., Zeng, L., and Kim, Y. J. (2010). A closure study of aerosol hygroscopic growth factor during the 2006 Pearl River Delta Campaign. *Advances in Atmospheric Sciences*, 27(4):947–956.
- Ma, Q., Ma, J., Liu, C., Lai, C., and He, H. (2013). Laboratory study on the hygroscopic behavior of external and internal C2-C4 dicarboxylic acid-NaCl mixtures. *Environmental science & technology*, 47(18):10381–10388.

- Malm, W. C. and Day, D. E. (2001). Estimates of aerosol species scattering characteristics as a function of relative humidity. *Atmospheric Environment*, 35(16):2845–2860.
- Martin, S. T. (2000). Phase transitions of aqueous atmospheric particles. *Chemical Reviews*, 100(9):3403–3454.
- Massling, A., Leinert, S., Wiedensohler, A., and Covert, D. (2007). Hygroscopic growth of sub-micrometer and one-micrometer aerosol particles measured during ACE-Asia. *Atmospheric Chemistry and Physics*, 7(12):3249–3259.
- Massoli, P., Bates, T., Quinn, P., Lack, D., Baynard, T., Lerner, B., Tucker, S., Brioude, J., Stohl, A., and Williams, E. (2009). Aerosol optical and hygroscopic properties during TexAQS-GoMACCS 2006 and their impact on aerosol direct radiative forcing. *Journal of Geophysical Research: Atmospheres*, 114(D7).
- Matsuki, A., Iwasaka, Y., Shi, G., Zhang, D., Trochkin, D., Yamada, M., Kim, Y.-S., Chen, B., Nagatani, T., Miyazawa, T., et al. (2005). Morphological and chemical modification of mineral dust: Observational insight into the heterogeneous uptake of acidic gases. *Geophysical research letters*, 32(22).
- Meier, J., Wehner, B., Massling, A., Birmili, W., Nowak, A., Gnauk, T., Brüggemann, E., Herrmann, H., Min, H., and Wiedensohler, A. (2009). Hygroscopic growth of urban aerosol particles in Beijing (China) during wintertime: a comparison of three experimental methods. *Atmospheric Chemistry and Physics*, 9(18):6865–6880.
- Meskhidze, N., Petters, M. D., Tsigaridis, K., Bates, T., O’Dowd, C., Reid, J., Lewis, E. R., Gantt, B., Anguelova, M. D., Bhave, P. V., et al. (2013). Production mechanisms, number concentration, size distribution, chemical composition, and optical properties of sea spray aerosols. *Atmospheric Science Letters*, 14(4):207–213.
- Meyer, N. K., Duplissy, J., Gysel, M., Metzger, A., Dommen, J., Weingartner, E., Alfarra, M. R., Prevot, A. S. H., Fletcher, C., Good, N., McFiggans, G., Jonsson, Å. M., Hallquist, M., Baltensperger, U., and Ristovski, Z. D. (2009). Analysis of the hygroscopic

- and volatile properties of ammonium sulphate seeded and unseeded SOA particles. *Atmospheric Chemistry and Physics*, 9(2):721–732.
- Michaud, V. (2009). *Etude des propriétés hygroscopiques des aérosols atmosphériques*. PhD thesis, Université Blaise Pascal-Clermont-Ferrand II.
- Michaud, V., Haddad, I. E., Liu, Y., Sellegri, K., Laj, P., Villani, P., Picard, D., Marchand, N., and Monod, A. (2009). In-cloud processes of methacrolein under simulated conditions—part 3: Hygroscopic and volatility properties of the formed secondary organic aerosol. *Atmospheric Chemistry and Physics*, 9(14):5119–5130.
- Mie, G. (1908). Beiträge zur optik trüber medien, speziell kolloidaler Metallösungen. *Annalen der physik*, 330(3):377–445.
- Moore, R. and Raymond, T. (2008). HTDMA analysis of multicomponent dicarboxylic acid aerosols with comparison to UNIFAC and ZSR. *Journal of Geophysical Research: Atmospheres*, 113(D4).
- Müller, T., Laborde, M., Kassell, G., and Wiedensohler, A. (2011). Design and performance of a three-wavelength LED-based total scatter and backscatter integrating nephelometer. *Atmospheric Measurement Techniques*, 4(6):1291–1303.
- Myhre, G., Samset, B. H., Schulz, M., Balkanski, Y., Bauer, S., Berntsen, T. K., Bian, H., Bellouin, N., Chin, M., Diehl, T., et al. (2013a). Radiative forcing of the direct aerosol effect from AeroCom Phase II simulations. *Atmospheric Chemistry and Physics*, 13(4):1853.
- Myhre, G., Shindell, D., Bréon, F., Collins, W., Fuglestedt, J., Huang, J., Koch, D., Lamarque, J., Lee, D., Mendoza, B., et al. (2013b). Climate change 2013: the physical science basis. contribution of working group I to the fifth assessment report of the intergovernmental panel on climate change. *K., Tignor, M., Allen, SK, Boschung, J., Nauels, A., Xia, Y., Bex, V., and Midgley, PM, Cambridge University Press Cambridge, United Kingdom and New York, NY, USA.*

- Nenes, A., Pandis, S. N., and Pilinis, C. (1998). ISORROPIA: A new thermodynamic equilibrium model for multiphase multicomponent inorganic aerosols. *Aquatic geochemistry*, 4(1):123–152.
- Nyquist, R. A., Putzig, C. L., and Leung, M. A. (1997). *The handbook of infrared and Raman spectra of inorganic compounds and organic salts. 2. Infrared and Raman spectral atlas of inorganic compounds and organic salts, Raman spectra*. Academic press, San Diego.
- Pandolfi, M., Alados-Arboledas, L., Alastuey, A., Andrade, M., Angelov, C., Artiñano, B., Backman, J., Baltensperger, U., Bonasoni, P., Bukowiecki, N., et al. (2018). A european aerosol phenomenology-6: scattering properties of atmospheric aerosol particles from 28 ACTRIS sites. *Atmospheric Chemistry and Physics*, 18(11):7877–7911.
- Peng, C., Jing, B., Guo, Y.-C., Zhang, Y.-H., and Ge, M.-F. (2016). Hygroscopic behavior of multicomponent aerosols involving NaCl and dicarboxylic acids. *The Journal of Physical Chemistry A*, 120(7):1029–1038.
- Pere, J.-C., Mallet, M., Bessagnet, B., and Pont, V. (2009). Evidence of the aerosol core-shell mixing state over europe during the heat wave of summer 2003 by using CHIMERE simulations and AERONET inversions. *Geophysical Research Letters*, 36(9).
- Petters, M. and Kreidenweis, S. (2007). A single parameter representation of hygroscopic growth and cloud condensation nucleus activity. *Atmospheric Chemistry and Physics*, 7(8):1961–1971.
- Pilinis, C., Pandis, S. N., and Seinfeld, J. H. (1995). Sensitivity of direct climate forcing by atmospheric aerosols to aerosol size and composition. *Journal of Geophysical Research: Atmospheres*, 100(D9):18739–18754.
- Pilinis, C. and Seinfeld, J. H. (1987). Continued development of a general equilibrium model for inorganic multicomponent atmospheric aerosols. *Atmospheric Environment (1967)*, 21(11):2453–2466.

- Pilinis, C., Seinfeld, J. H., and Grosjean, D. (1989). Water content of atmospheric aerosols. *Atmospheric Environment (1967)*, 23(7):1601–1606.
- Pöschl, U. (2005). Atmospheric aerosols: composition, transformation, climate and health effects. *Angewandte Chemie International Edition*, 44(46):7520–7540.
- Potukuchi, S. and Wexler, A. S. (1995). Identifying solid-aqueous phase transitions in atmospheric aerosols-I. Neutral-acidity solutions. *Atmospheric Environment*, 29(14):1663–1676.
- Prather, K. A., Bertram, T. H., Grassian, V. H., Deane, G. B., Stokes, M. D., DeMott, P. J., Aluwihare, L. I., Palenik, B. P., Azam, F., Seinfeld, J. H., et al. (2013). Bringing the ocean into the laboratory to probe the chemical complexity of sea spray aerosol. *Proceedings of the National Academy of Sciences*, 110(19):7550–7555.
- Prenni, A. J., DeMott, P. J., and Kreidenweis, S. M. (2003). Water uptake of internally mixed particles containing ammonium sulfate and dicarboxylic acids. *Atmospheric Environment*, 37(30):4243–4251.
- Ramabhadran, T., Peterson, T., and Seinfeld, J. (1976). Dynamics of aerosol coagulation and condensation. *AIChE Journal*, 22(5):840–851.
- Ramachandran, S. and Srivastava, R. (2013). Influences of external vs. core-shell mixing on aerosol optical properties at various relative humidities. *Environmental Science: Processes & Impacts*, 15(5):1070–1077.
- Ramanathan, V., Crutzen, P., Kiehl, J., and Rosenfeld, D. (2001). Aerosols, climate, and the hydrological cycle. *science*, 294(5549):2119–2124.
- Randriamiarisoa, H., Chazette, P., Couvert, P., Sanak, J., and Mégie, G. (2006). Relative humidity impact on aerosol parameters in a Paris suburban area. *Atmospheric Chemistry and Physics*, 6(5):1389–1407.

- Richardson, C. and Spann, J. (1984). Measurement of the water cycle in a levitated ammonium sulfate particle. *Journal of aerosol science*, 15(5):563–571.
- Rood, M., Larson, T., Covert, D., and Ahlquist, N. (1985). Measurement of laboratory and ambient aerosols with temperature and humidity controlled nephelometry. *Atmospheric Environment (1967)*, 19(7):1181–1190.
- Schaap, M., Apituley, A., Timmermans, R., Koelemeijer, R., and Leeuw, G. d. (2009). Exploring the relation between aerosol optical depth and PM<sub>2.5</sub> at Cabauw, the Netherlands. *Atmospheric Chemistry and Physics*, 9(3):909–925.
- Schuster, G. L., Lin, B., and Dubovik, O. (2009). Remote sensing of aerosol water uptake. *Geophysical Research Letters*, 36(L03814, doi:10.1029/2008GL036576).
- Schwartz, S. E. (1996). The whitehouse effect-Shortwave radiative forcing of climate by anthropogenic aerosols: An overview. *Journal of Aerosol Science*, 27(3):359–382.
- Seinfeld, J. and Pandis, S. (2006). *Atmospheric Chemistry and Physics: From Air Pollution to Climate Change*. Wiley.
- Seinfeld, J. H. and Pandis, S. N. (1998). Atmospheric chemistry and physics: from air pollution to climate change. In *Atmospheric chemistry and physics: from air pollution to climate change*. Publisher: New York, NY: Wiley, 1998 Physical description: xxvii, 1326 p. A Wiley-Interscience Publication. ISBN: 0471178152.
- Seng, S. (2017). *Phototransformation de composés d'intérêt atmosphérique: études spectroscopiques en phase gaz, en matrice cryogénique et à l'échelle des particules individuelles*. PhD thesis, Lille 1.
- Seng, S., Guo, F., Tobon, Y. A., Ishikawa, T., Moreau, M., Ishizaka, S., and Sobanska, S. (2018a). Deliquescence behavior of photo-irradiated single NaNO<sub>3</sub> droplets. *Atmospheric Environment*, 183:33–39.

- Seng, S., Iorena Picone, A., Bava, Y. B., Moreau, M., Ciuraru, R., George, C., Romano, R. M., Sobanska, S., Tobon, Y. A., et al. (2018b). Photodegradation of methyl thioglycolate particles as a proxy for organosulphur containing droplets. *Physical Chemistry Chemical Physics*.
- Signorell, R. and Reid, J. P. (2010). *Fundamentals and applications in aerosol spectroscopy*. CRC Press.
- Solomon, S., Qin, D., Manning, M., Chen, Z., Marquis, M., Averyt, K. B., Tignor, M., Miller, H. L., et al. (2007). Contribution of working group I to the fourth assessment report of the intergovernmental panel on climate change, 2007.
- Spann, J. and Richardson, C. (1985). Measurement of the water cycle in mixed ammonium acid sulfate particles. *Atmospheric Environment (1967)*, 19(5):819–825.
- Stokes, R. and Robinson, R. (1966). Interactions in aqueous nonelectrolyte solutions. I. solute-solvent equilibria. *The Journal of Physical Chemistry*, 70(7):2126–2131.
- Sullivan, R., Moore, M., Petters, M., Kreidenweis, S., Roberts, G., and Prather, K. (2009). Effect of chemical mixing state on the hygroscopicity and cloud nucleation properties of calcium mineral dust particles. *Atmospheric Chemistry and Physics*, 9(10):3303–3316.
- Svenningsson, B., Rissler, J., Swietlicki, E., Mircea, M., Bilde, M., Facchini, M., Decesari, S., Fuzzi, S., Zhou, J., Mønster, J., et al. (2006). Hygroscopic growth and critical supersaturations for mixed aerosol particles of inorganic and organic compounds of atmospheric relevance. *Atmospheric Chemistry and Physics*, 6(7):1937–1952.
- Tang, I. (2000). Phase transformation and growth of hygroscopic aerosols. *Aerosol chemical processes in the environment*. CRC Press, Boca Raton, pages 61–79.
- Tang, I. and Munkelwitz, H. (1994a). Aerosol phase transformation and growth in the atmosphere. *Journal of Applied Meteorology*, 33(7):791–796.

- Tang, I. and Munkelwitz, H. (1994b). Water activities, densities, and refractive indices of aqueous sulfates and sodium nitrate droplets of atmospheric importance. *Journal of Geophysical Research: Atmospheres*, 99(D9):18801–18808.
- Tang, I., Munkelwitz, H., and Davis, J. (1978). Aerosol growth studies—IV. phase transformation of mixed salt aerosols in a moist atmosphere. *Journal of Aerosol Science*, 9(6):505–511.
- Tang, I. N. (1996a). Chemical and size effects of hygroscopic aerosols on light scattering coefficients. *Journal of Geophysical Research: Atmospheres*, 101(D14):19245–19250.
- Tang, I. N. (1996b). Chemical and size effects of hygroscopic aerosols on light scattering coefficients. *JOURNAL OF GEOPHYSICAL RESEARCH*,.
- Tang, I. N. and Munkelwitz, H. R. (1993). Composition and temperature dependence of the deliquescence properties of hygroscopic aerosols. *Atmospheric Environment. Part A. General Topics*, 27(4):467–473.
- Tang, I. N., Tridico, A., and Fung, K. (1997). Thermodynamic and optical properties of sea salt aerosols. *Journal of Geophysical Research: Atmospheres*, 102(D19):23269–23275.
- Tang, M., Cziczo, D. J., and Grassian, V. H. (2016). Interactions of water with mineral dust aerosol: water adsorption, hygroscopicity, cloud condensation, and ice nucleation. *Chemical reviews*, 116(7):4205–4259.
- Textor, C., Schulz, M., Guibert, S., Kinne, S., Balkanski, Y., Bauer, S., Berntsen, T., Berglen, T., Boucher, O., Chin, M., et al. (2006). Analysis and quantification of the diversities of aerosol life cycles within AeroCom. *Atmospheric Chemistry and Physics*, 6(7):1777–1813.
- Titos, G., Cazorla, A., Zieger, P., Andrews, E., Lyamani, H., Granados-Muñoz, M., Olmo, F., and Alados-Arboledas, L. (2016). Effect of hygroscopic growth on the aerosol light-scattering coefficient: A review of measurements, techniques and error sources. *Atmospheric Environment*, 141:494 – 507.

- Titos, G., Jefferson, A., Sheridan, P., Andrews, E., Lyamani, H., Alados-Arboledas, L., and Ogren, J. (2014). Aerosol light-scattering enhancement due to water uptake during the TCAP campaign. *Atmospheric Chemistry and Physics*, 14(13):7031–7043.
- Tobon, Y. A., Seng, S., Picone, L. A., Bava, Y. B., Juncal, L. C., Moreau, M., Romano, R. M., Barbillat, J., and Sobanska, S. (2017). Photochemistry of single particles using acoustic levitation coupled with Raman microspectrometry. *Journal of Raman Spectroscopy*, 48(8):1135–1137.
- Tong, C., Clegg, S. L., and Seinfeld, J. H. (2008). Comparison of activity coefficient models for atmospheric aerosols containing mixtures of electrolytes, organics, and water. *Atmospheric Environment*, 42(21):5459–5482.
- Topping, D., Coe, H., McFiggans, G., Burgess, R., Allan, J., Alfarra, M., Bower, K., Choulaton, T., Decesari, S., and Facchini, M. C. (2004). Aerosol chemical characteristics from sampling conducted on the island of jeju, korea during ACE Asia. *Atmospheric Environment*, 38(14):2111–2123.
- Topping, D., McFiggans, G., and Coe, H. (2005). A curved multi-component aerosol hygroscopicity model framework: Part 1–Inorganic compounds. *Atmospheric Chemistry and Physics*, 5(5):1205–1222.
- Treuel, L., Pederzani, S., and Zellner, R. (2009). Deliquescence behaviour and crystallisation of ternary ammonium sulfate/dicarboxylic acid/water aerosols. *Physical Chemistry Chemical Physics*, 11(36):7976–7984.
- Trunk, M., Lübben, J., Popp, J., Schrader, B., and Kiefer, W. (1997). Investigation of a phase transition in a single optically levitated microdroplet by Raman-Mie scattering. *Applied optics*, 36(15):3305–3309.
- Turrell, G. (1972). Infrared and Raman spectra of crystals.
- Twomey, S. (1977). The influence of pollution on the shortwave albedo of clouds. *Journal of the atmospheric sciences*, 34(7):1149–1152.

- Uchiyama, A. (2014). Method to retrieve single scattering properties of aerosols using multi-wavelength scattering and absorption coefficient data measured by integrating nephelometer and absorption photometer. *Journal of the Meteorological Society of Japan. Ser. II*, 92:71–91.
- Veghte, D. P., Altaf, M. B., and Freedman, M. A. (2013). Size dependence of the structure of organic aerosol. *Journal of the American Chemical Society*, 135(43):16046–16049.
- Vlasenko, A., Sjögren, S., Weingartner, E., Gäggeler, H., and Ammann, M. (2005). Generation of submicron Arizona test dust aerosol: Chemical and hygroscopic properties. *Aerosol science and technology*, 39(5):452–460.
- Wang, L., Khalizov, A. F., Zheng, J., Xu, W., Ma, Y., Lal, V., and Zhang, R. (2010). Atmospheric nanoparticles formed from heterogeneous reactions of organics. *Nature Geoscience*, 3(4):238.
- Weingartner, E., Keller, C., Stahel, W., Burtscher, H., and Baltensperger, U. (1997). Aerosol emission in a road tunnel. *Atmospheric Environment*, 31(3):451–462.
- Wexler, A. S. and Clegg, S. L. (2002). Atmospheric aerosol models for systems including the ions H<sup>+</sup>, NH<sub>4</sub><sup>+</sup>, Na<sup>+</sup>, SO<sub>4</sub><sup>2-</sup>, NO<sub>3</sub><sup>-</sup>, Cl<sup>-</sup>, Br<sup>-</sup>, and H<sub>2</sub>O. *Journal of Geophysical Research: Atmospheres*, 107(D14):ACH-14.
- Wexler, A. S. and Seinfeld, J. H. (1991). Second-generation inorganic aerosol model. *Atmospheric Environment. Part A. General Topics*, 25(12):2731–2748.
- Whitby, K. T. (1978). The physical characteristics of sulfur aerosols. *Atmospheric Environment*, 12:135 – 159.
- Wilson, E. B., Decius, J. C., and Cross, P. C. (1955). *Molecular vibrations: the theory of infrared and Raman vibrational spectra*. Courier Corporation.
- Winkler, P. (1973). The growth of atmospheric aerosol particles as a function of the relative

- humidity-II. an improved concept of mixed nuclei. *Journal of Aerosol Science*, 4(5):373–387.
- Wise, M. E., Freney, E. J., Tyree, C. A., Allen, J. O., Martin, S. T., Russell, L. M., and Buseck, P. R. (2009). Hygroscopic behavior and liquid-layer composition of aerosol particles generated from natural and artificial seawater. *Journal of Geophysical Research: Atmospheres*, 114(D3).
- Wise, M. E., Semeniuk, T. A., Bruintjes, R., Martin, S. T., Russell, L. M., and Buseck, P. R. (2007). Hygroscopic behavior of NaCl-bearing natural aerosol particles using environmental transmission electron microscopy. *Journal of Geophysical Research: Atmospheres*, 112(D10).
- Wise, M. E., Surratt, J. D., Curtis, D. B., Shilling, J. E., and Tolbert, M. A. (2003). Hygroscopic growth of ammonium sulfate/dicarboxylic acids. *Journal of Geophysical Research: Atmospheres*, 108(D20).
- Wu, Z., Birmili, W., Poulain, L., Wang, Z., Merkel, M., Fahlbusch, B., Pinxteren, D. v., Herrmann, H., and Wiedensohler, A. (2013). Particle hygroscopicity during atmospheric new particle formation events: implications for the chemical species contributing to particle growth. *Atmospheric Chemistry and Physics*, 13(13):6637–6646.
- Yeung, M. C., Lee, A. K., and Chan, C. K. (2009). Phase transition and hygroscopic properties of internally mixed ammonium sulfate and adipic acid (AS-AA) particles by optical microscopic imaging and raman spectroscopy. *Aerosol science and technology*, 43(5):387–399.
- Yoon, S.-C. and Kim, J. (2006). Influences of relative humidity on aerosol optical properties and aerosol radiative forcing during ACE-Asia. *Atmospheric Environment*, 40(23):4328–4338.
- Zappoli, S., Andracchio, A., Fuzzi, S., Facchini, M., Gelencser, A., Kiss, G., Krivacsy, Z., Molnar, A., Meszaros, E., Hansson, H.-C., et al. (1999). Inorganic, organic and

- macromolecular components of fine aerosol in different areas of Europe in relation to their water solubility. *Atmospheric Environment*, 33(17):2733–2743.
- Zardini, A., Sjogren, S., Marcolli, C., Krieger, U., Gysel, M., Weingartner, E., Baltensperger, U., and Peter, T. (2008). A combined particle trap/HTDMA hygroscopicity study of mixed inorganic/organic aerosol particles. *Atmospheric Chemistry and Physics*, 8(18):5589–5601.
- Zdanovskii, A. (1948). New methods for calculating solubilities of electrolytes in multicomponent systems. *Zh. Fiz. Khim*, 22(1475):1475–85.
- Zhang, D., Shi, G.-Y., Iwasaka, Y., and Hu, M. (2000a). Mixture of sulfate and nitrate in coastal atmospheric aerosols: individual particle studies in Qingdao (36°04' N, 120°21' E), China. *Atmospheric Environment*, 34(17):2669–2679.
- Zhang, D., Shi, G.-Y., Iwasaka, Y., and Hu, M. (2000b). Mixture of sulfate and nitrate in coastal atmospheric aerosols: individual particle studies in Qingdao (36°04'N, 120°21'E), china. *Atmospheric Environment*, 34(17):2669 – 2679.
- Zhang, Q., Jimenez, J. L., Canagaratna, M., Allan, J., Coe, H., Ulbrich, I., Alfarra, M., Takami, A., Middlebrook, A., Sun, Y., et al. (2007). Ubiquity and dominance of oxygenated species in organic aerosols in anthropogenically-influenced Northern Hemisphere midlatitudes. *Geophysical Research Letters*, 34(13).
- Zhou, Q., Pang, S.-F., Wang, Y., Ma, J.-B., and Zhang, Y.-H. (2014). Confocal raman studies of the evolution of the physical state of mixed phthalic acid/ammonium sulfate aerosol droplets and the effect of substrates. *The Journal of Physical Chemistry B*, 118(23):6198–6205.
- Zieger, P., Fierz-Schmidhauser, R., Weingartner, E., and Baltensperger, U. (2013). Effects of relative humidity on aerosol light scattering: results from different European sites. *Atmospheric Chemistry and Physics*, 13(21):10609–10631.

- Zieger, P., Väisänen, O., Corbin, J., Partridge, D. G., Bastelberger, S., Mousavi-Fard, M., Rosati, B., Gysel, M., Krieger, U., Leck, C., et al. (2017). Revising the hygroscopicity of inorganic sea salt particles. *Nature Communications*, 8:ncomms15883.
- Zieger, P., Weingartner, E., Henzing, J., Moerman, M., de Leeuw, G., Mikkilä, J., Ehn, M., Petäjä, T., Clémer, K., van Roozendaal, M., Yilmaz, S., Frieß, U., Irie, H., Wagner, T., Shaiganfar, R., Beirle, S., Apituley, A., Wilson, K., and Baltensperger, U. (2011). Comparison of ambient aerosol extinction coefficients obtained from in-situ, MAX-DOAS and LIDAR measurements at Cabauw. *Atmospheric Chemistry and Physics*, 11(6):2603–2624.
- Ziemba, L. D., Lee Thornhill, K., Ferrare, R., Barrick, J., Beyersdorf, A. J., Chen, G., Crumeyrolle, S. N., Hair, J., Hostetler, C., Hudgins, C., et al. (2013). Airborne observations of aerosol extinction by in situ and remote-sensing techniques: Evaluation of particle hygroscopicity. *Geophysical Research Letters*, 40(2):417–422.